JPRS-JST-91-015
2 MAY 1991

Foreign Broadcast Information Service 50 ANNIVERSARY 1941 - 1991

JPRS Report

Science & Technology

Japan

INTERNATIONAL MEETING ON NEW GLASS TECHNOLOGY

JPRS-JST-91-015
2 MAY 1991

SCIENCE & TECHNOLOGY

JAPAN

INTERNATIONAL MEETING ON NEW GLASS TECHNOLOGY

43078079E Tokyo INTERNATIONAL MEETING ON NEW GLASS TECHNOLOGY in English
10-11 Dec 90 pp 1-123

[Selections from International Meeting on New Glass Technology (N.G.F.'90) held 10-11 Dec 90 in Tokyo, sponsored by the Association of New Glass Industries]

CONTENTS

International Meeting on New Glass Technology (N.G.F '90)

- Glass Material Design Technical Meeting
- Nonlinear Optical Material Technical Meeting
- Composite Glass Technical Meeting
- Machining and Processing Technical Meeting

December 10~11, 1990

The Association of New Glass Industries

International Meeting on New Glass Technology (N.G.F. '90)

Program

December 10, 1990 (The Hall at B2)

14:00~14:05 Opening Address — Tatsuji Nakajima
(President; The Association of New Glass Industries)

14:05~14:10 Congraturation — Naotoshi Osada
(Director; Cermaics and Construction Materials Division, MITI)

14:10~17:00 **Session I: Chairman; H. Kawazoe (The Hall at B2)**
(Research Laboratory of Engineering Materials Tokyo Institute of Technology)

1) Robert A. Weeks *(Vanderbilt University, U.S.A.)*
"New Glasses Produced by Ion-Implantation"

15:05~15:20 Coffee Break

2) Mr. Yamane *(Tokyo Institute of Technology)*
"A Study on New Glass by Sol-Gel Process"

3) O. V. Mazurin *(Institute of Silicate Chemistry of the Academy of Sciences of U.S.S.R.)*
"Collection and Selection of Glass Properties Data"

17:30~20:00 Party

December 11, 1990

10:00~17:00 **Session II (Room 3035 at B3)**

10:00~13:00 ***Glass Material Design Technical Meeting**
Chairman: K. Arai *(Electrotechnical Laboratory, MITI)*

1) David L. Griscom *(Naval Research Laboratory, U.S.A.)*
"SHG in SiO_2: GeO_2 Waveguides"

2) S. Takahashi *(NTT)*
"Materials Design of Functional Glasses"

3) H. Kawazoe *(Tokyo Institute of Technology)*
Y. Watanabe, M. Takada *(Nagaoka University of Technology)*
"Band Structure-Design of Inorganic Materials with Optoelectronic Use"

14:00~17:00 ***Nonlinear Optical Material Technical Meeting**
Chairman: K. Nishizawa *(Nippon Sheet Glass)*

1) A. Nakamura *(Nagoya University)*
"Physics on Nonlinera Glass Materials"

2) T. Kobayashi *(University of Tokyo)*
"Nonlinear Optical Properties of Semiconductors Prepared by a New Method and Studies by a Novel Techniques"

3) Eva M. Vogel *(Bellcore, U.S.A.)*
"Glasses for Nonlinear Optical Devices"

4) J. Yumoto *(NTT)*
"Optical Characteristics on CdS_xSe_{1-x} Doped Glasses"

10:00~17:00 **Session III (Room 3036 at B3)**

10:00~13:00) ***Composite Glass Technical Meeting**
Chairman: K. Niihara *(Osaka University)*

1) T. Kokubo *(Kyoto University)*
"Glass-Based Composites for Biomedical Applications"

2) O. Y. Chen *(United Technology, U.S.A.)*
"Fiber Reinforced Glass and Glass Cermaics"

3) A. Matsuda *(Nippon Sheet Glass)*
"Organic Polymer-Containing Gels for Fine Patterning on Glass Substrates"

14:00~17:00 **•Machining and Processing Technical Meeting**

Chairman: I. Suzuki *(HOYA Corp.)*

1) Ronald O. Scattergood *(North Carolina State University, U.S.A.)*
   "Ductile-Regime Grinding"
2) T. Moriwaki *(Kobe University)*
   "Machining Characteristics of Metals and Brittle Materials"
3) J. Takashita *(CANNON Inc.)*
   "Elastic Emission Machining Technology for Glass Material Optics"

• The Place of Meeting is Kikai Shinkoukaikan.
Address: 8-5, 3-chome Shibakoen, Minato-ku, Tokyo 105, Japan

SESSION I

OPTICAL AND MAGNETIC PROPERTIES OF TRANSITION METAL ION IMPLANTED SILICA

R. A. Weeks

Department of Materials Science and Engineering
Vanderbilt University, Nashville, TN 37235, USA

The optical and magnetic properties of the surface and near surface regions of high purity silica were modified by the implantation of transition metal ions (Ti^+, Cr^+, Mn^+, and Fe^+, Cu^+) at 160 keV and 4 $\mu A/cm^2$ to doses ranging from 0.5×10^{16} to 6×10^{16} ions/cm^2. The implanted ion distribution, measured by backscattering techniques, was gaussian in shape with a peak 0.12 μ from the surface and with a full width at half maximum of 0.14 μm with the exception of Cu. Optical absorption bands due to radiation damage at 5.0 eV and 5.8 eV superimposed on the low energy tail of an absorption band were resolved. The refractive index of the ion modified region, measured by ellipsometric techniques, increased with increasing implantation dose. For a dose of 6×10^{16} ions/cm^2, the refractive index increased with increasing stomic mass of the implanted ion. The temperature and orientation dependence of the electron paramagnetic resonance (EPR) spectra of the implanted samples show vastly different magnetic characteristics as a function of transition metal ion species. The EPR spectra, at room temperature, for the 6×10^{16} ions/cm^2 samples show the signal from the implanted Fe to be approximately 40 times greater than the Mn signal and a signal from implanted Cr was not observed. The EPR spectra indicate that the ion modified surface region contains a mixture of magnetic phases measurements of the record order refractive index in Ti and Cu implanted samples showed the implanted regions to have values several orders of magnitude greater than silica. The data reviewed demonstrates that the materials produced by implantation of transition metal ions into amorphous silica are new materials. The properties of the ion modified regions are not predictable from existing data or theories.

RESUME

ROBERT A. WEEKS

Born in 1924 in Birmingham, alabama, U. S. A., Robert A. Weeks received his early education in that city. Hé was awarded a B. S. in Physics from Birmingham-Southern College, a M. S. in Physics from the University of Tennessee and Ph. D. in Physics from Brown University. In 1951 he joined the Solid State Physics Division of the Oak Ridge National Laboratory and in 1984 was appointed Research Professor of Materials Science at Vanderbilt University.

In 1970 he as Distinguished Visiting Professor, American University in Cairo, Cairo, Egypt; in 1981 Professor Invité. Ecole Polytechnique Federale de Lausanne, Lausanne, Switzerland; in 1983 Visiting Professor, Catholic University of Leuven, Leuven, Belgium. He served as Associate Editor, Journal of Geophysical Research, 1968—1974 and was appointed Editor, Journal of Non-Crystalline Solids in 1988.

His research interests are optical, electrical and magnetic properties of wide band-gap solids and the modification of these properties by radiation with photons and particles. He pioneered the application of electron paramagnetic resonance spectroscopy to the investigation of these modifications. He has had a primary interest in non-crystalline solids in 1988.

A Study on New Glass by Sol-Gel Process

Masayuki YAMANE

Department of Inorganic Materials,

Tokyo Institute of Technology,

2-12-1 Ookayama, Meguro-ku, Tokyo 152 Japan

The sol-gel process has been receiving a great deal of attention in this decade as a new technique of glass preparation owing to its potential advantages over conventional method of glass formation by melt-quenching. These advantages are particularly important in developing the new glasses in the fields of optics and opto-electronics.

The basic studies on sol-gel process relevant to the fabrication of new glasses have been made in this decade by numerous researchers in the world. These include the study on the phenomena of hydrolysis and polycondensation of silicon alkoxide , drying of a monolithic gel, dip- or spin- coating of thin film on a glass substrate , fiber drawings, elimination of heterogeneity in multicomponent systems, and densification et. cetera.

The important results of these studies have mostly been reported in the following three international conference series, i.e., The International Workshop on Glasses and Ceramics from Gels, The International Conference on Ultrastructure Processings of Glasses, Ceramics and Composites, The International Symposium on Better Ceramics Through Chemistry.

The development of various new glasses have been tried in this decade. These include sol-gel coated glasses for various optical and electronic uses, silica fiber of low dielectric constant, silica fiber for thermal insulation, doped silica fiber for optical communication, glass laser, large sized silica glass plates and tubes, gradient-index rods, semiconductor doped glass for non-linear optics, et cetera.

New glasses prepared by coating technique were mostly

successful and now commercially produced.

The silica glass fiber of low dielectric constant was also successfully developed by drawing technique and is now manufactured to be used as a part of electronic devices as well as furnaces for semi-conductor industries where very clean insulating material is required. The doped silica fiber prepared by sol-gel process for optical communication, however, could not attain better quality than the one by chemical vapor deposition process.

In spite of the effort made by numerous researchers, none of the monolithic materials is on commercial production yet, although some of them seem to be promising.

Difficulty of commercial application of the sol-gel derived monolithic glass is attributed to large shrinkage of a gel in the drying stage, and the difficulty in completely eliminating bubble inclusion. Such disadvantages are particularly serious in developing new glasses which is obtainable by the existing highly competitive techniques.

From this point of view, sol-gel process should be applied on new glasses whose quality is expected to be far superior to the one by alternative ways.

Among new glasses, some including silica glass of high UV transmittance, gradient index glass rods, semiconductor doped glasses for non-linear optics may be advantageously produced by sol-gel process.

A silica glass prepared by Professor L.L.Hench and group of Geltech Co. under the precise control of the process tranmits UV light to the wavelength as low as 150 nm. This value of

transmittance is much better than that of silica glasses by made existing technique. This silica glass of good UV transmittance will be an important material for semiconductor industries who uses an excimer laser of very short wavelength.

Study on the gradient-index (GRIN) glass rods by sol-gel process is now in progress at Hitachi Cable CO. , Enimont America Inc., and Tokyo Institute of Technology. The fabrication of GRIN rods in the first two research groups is based on the partial leaching of index-modifying cations such as Ti, Ge, or Zr from silicate gels of binary or ternary systems. The GRIN rods obtained by this method have very accurate index profile and show a superior beam collimation property to any other GRIN rods.

While ion-exchange technique can hardly produce GRIN rods of large diameter, a GRIN rod rod having diameter larger than 10 mm with the difference of 0.05 in refractive index between center and perimeter was prepared at Tokyo Institute of Technology based on the inter-diffusion of index-modifying cations through liquid phase in the micropores of a wet gel.

Preparation of semiconductor doped glasses for non-linear optics by sol-gel process is now attracting an attention. The semiconductor-doped glass currently obtained by the melt-quenching technique is limited in its efficiency due to the limiting amount of CdS or CdSe content to be incorporated in the glass. In sol-gel process a glass containing very fine particles of these semiconducting crystal is expected to be obtained independent of the solubility of the material to the glass matrix, which will allow us the fabrication of the glass with the higher number density of fine crystalline particles.

COLLECTION AND SELECTION OF GLASS PROPERTIES DATA

O. V. MAZURIN
INSTITUTE OF SILICATE CHEMISTRY OF
THE ACADEMY OF SCIENCES OF U.S.S.R.

SESSION II

(1)

Abstract of paper to be presented at the International Meeting on New Glass Technology (N.G.F. '90), Tokyo, Japan, December 10–11, 1990

SECOND-HARMONIC GENERATION IN SiO_2 : G_2O_2 GLASS-FIBER WAVEGUIDES: A REVIEW

DAVID L. GRISCOM
NAVAL RESEARCH LABORATORY, WASHINGTON, DC 20375, USA

Since its unexpected discovery in 1986,[1] the phenomenon of second-harmonic generation (SHG) in optical fibers has become a subject of intense scientific and technological interest. Typical experiments have involved Ge- or Ge-P-doped-core single-mode fibers pumped by a high-intensity mode-locked Q-switched laser operating at 1064-nm and have resulted in the generation of 532-nm second-harmonic (SH) light with conversion efficiencies sometimes exceeding 5%. There are many theories of the origin of SHG in glass fibers. A common element in all of these is that the 1064-nm pump and 532-nm SH light mix through the third-order susceptibility $\chi^{(3)}$ to generate an axially periodic DC polarization field.[2] This polarization field, possibly coupled with variations in the intensity of the SH light of the same periodicity,[3] create and/or organize periodic arrays of oriented dipoles which give rise to a phase-matched $\chi^{(2)}$ grating. These grating build up over a period of hours under very intense pumping (-100 GW/cm^2) by 1064-nm light alone,[1] presumably seeded by a weak SH signal arising from bulk quadrupole or core-cladding surface interactions. However, the writing time can be reduced to minutes, even at much lower pump powers, by deliberate seeding with SH light.[2] It has been shown[4] that Ge doping of the fiber core is a necessary condition for grating formation, and more recently a correlation has been established between SHG efficiency and the photolytic production of Ge E′ centers (a positively charged oxygen vacancy defect) as detected by electron spin resonance (ESR).[5] These phenomena will be discussed in greater detail, with particular emphasis on the ESR data and their interpretation in terms of microscopic models.

[1] U. Österberg and W. Margulis, Opt. Lett. 11, 516 (1986).
[2] R. H. Stolen and H. W. K. Tom, Opt. Lett. 12, 585 (1987).
[3] M. C. Farries, P. St. J. Russel, M. E. Fermann, and D. N. Payne, Electron. Lett. 23, 322 (1987).
[4] M. A. Saifi and M. J. Andrejco, Opt. Lett. 13, 773 (1988).
[5] T. E. Tsai, M. A. Saifi, E. J. Friebele, D. L. Griscom, and U. Österberg, Opt. Lett. 14, 1023 (1989).

Material Design of Functional Glass

Shiro Takahashi
NTT Opto-electronics Laboratories

One of the biggest and most successful research projects on New Glass was that on optical fiber for communications use. The initial requirement for the development of this fiber was a transparency two orders of magnitude higher than that of usual optical grade glass. In fact, a four orders of magnitude improvement was achieved which is the theoretical limit of the materials' transmission characteristics. The development of low loss optical fiber has presented us with a new target which is functional glass.

"Functional" glass is used here to refer to glass which has useful and important characteristics for device application. To develop it successfully the characteristics of glass in general need to be carefully and thoroughly investigated. High optical absorption, for example, is an undesirable characteristic for the development of low loss optical fiber, in contrast, it is advantageous for fiber laser development.

There are many possible kinds of functional glass which will correspond to various characteristics. These will include infrared transparent glass, laser glass and glass for use in nonlinear optics. In this paper, however, only the optical functions relating to optical fiber are described.

A fundamental understanding of transmission loss mechanism in optical fiber, namely the interactions between light and materials, was obtained during the course of research on loss reduction. Based on this knowledge, the possibility of ultra-low loss optical fiber has been predicted. The known optical characteristics of glass with good transparency in the infrared wavelength region, a low glass transition temperature or a small refractive index, are being used to design ultra-low loss optical fiber materials.

The most important factor in the material design of functional glass is to understand the intrinsic characteristics of the glass precisely and fundamentally. Furthermore, in order to develop functional devices it is important to investigate extrinsic characteristics such as the dispersion caused by waveguide structures and gain properties which are affected by the dopant distribution profile in the fiber core.

The realization of new glass devices required comprehensive research and development including the material and structural design of functional glass. As examples of these functional devices, ultra-low loss optical fiber for telecommunications use and rare-earth doped fiber amplifiers will be reviewed.

Comprehensive material design must be effective in predicting device performance, selecting materials and indicating approaches for device realization.

SESSION II

(2)

Physics on Nonlinear Glass Materials
- Quantum Size Effects and Large Optical Nonlinearity -

Arao NAKAMURA
Department of Applied Physics, Faculty of Engineering
Nagoya University, Chikusa-ku, Nagoya, 464-01 JAPAN

Recently, there are increasing interests in nonlinear optical materials and devices that are capable of processing light signals without converting them to electronic forms. These all-optical devices are based on the nonlinear optical properties of materials, i.e., change of refractive index or absorption coefficient caused by an intense optical beam. Semiconductor heterostructures have attracted much attention, because of the large third-order susceptibility and its fast responding time.

In quantum well structures of GaAs/$Al_xGa_{1-x}As$ thin films, an electron or an exciton is one-dimensionally confined in an ultrathin layer. On the other hand, in small semiconducting microcrystallites with radii of several nanometers, which are embedded in matrices, photoexcited carriers are three-dimensionally confined and show zero-dimensional features. These quantum dots are expected to give rise to a larger enhancement of both linear and nonlinear susceptibilities than the two-dimensional system.

In this talk, I will report linear and nonlinear optical properties of CdSe- and CuCl- microcrystallites in glasses. In colored glasses semiconducting crystallites are precipitated during a secondary heat-treatment procedure. Variation in the heat treatment significantly alters the final crystallite size of the order of nanometer. In CdSe microcrystallites, electrons and holes are individually confined by the deep confining potential of glass and quantum confined levels are formed in both conduction band and valance band. On the other hand, in CuCl-microcrystallite embedded glasses in which the exciton

Bohr radius is relatively small (~ 7A), the translational motion of exciton is confined. These quantum size effects on the photoexcited carriers and excitons are clearly observed on the absorption spectra.

Using the degenerate four-wave mixing experiment, we have measured values of $\chi^{(3)}$ in CuCl microcrystallites with radii of 1.8 - 3.5 nm where the translational motion of exciton is confined. We have found the large enhancement of $\chi^{(3)}$ from 2×10^{-7} esu to 5×10^{-6} esu depending on the crystal radii. Furthermore, performing the pump and probe experiments in the femtosecond time region, we have investigated the relaxation dynamics of carriers and excitons between the sublevels and traps in CdSe-microcrystallite embedded glasses.

Excitonic Superradiance Observed by Picosecond Luminescence Dynamics and Quantum Confined Stark Effect Studied by Electroabsorption in CdS and CdS_xSe_{1-x} Microcrystallites

[1]Takayoshi Kobayashi, [1]Kazuhiko Misawa, [1]Shintaro Nomura, [2]Hiroshi Yao, and [2]Toyoharu Hayashi

[1]Department of Physics, University of Tokyo
Hongo 7-3-1, Bunkyo-ku, Tokyo 113, Japan
[2]Central Research Institute, Mitsui Toatsu Chemicals Inc.
Kasama-cho 1190, Sakae-ku, Yokohama 247, Japan

1. Abstract

We developed a new preparation method of the CdS microcrystallites which show enhanced band-edge emission and reduced trap emission. Using the sample we observed excitonic superradiance. By the electric field modulation spectroscopy, quantum confined Stark shift in semiconductor microcrystallites was observed and the shift was analyzed including Coulomb interaction.

2. Luminescence Decay of CdS Microcrystallites

The samples for the luminescence decay measurement were prepared by our new synthetic method[1]. CdS microcrystallites are embedded in an acrylonitrile-styrene copolymer film. The average diameter of the CdS microcrystallites was measured by TEM to be 39 $\pm$ 8 A. The luminescence spectrum of the CdS microcrystallites has a sharp peak near absorption band-edge at 440 nm and a red-shifted broad band with a peak near 700 nm. The band-edge emission is attributed to the direct recombination of electrons and holes, and the red-shifted band corresponds to the emission from the trapped states. The intensity ratio of the band-edge emission to the red-shifted emission is much larger than any other previously reported samples.

We measured the temporal behavior of the band-edge emission using a picosecond UV laser and a synchroscan streak camera. The UV pulse of 82 MHz was obtained in a β-BaB_2O_4 (BBO) crystal by the sum frequency generation of the fundamental of a cw mode-locked YAG laser and a rhodamine 6G laser synchronously pumped by the second-harmonic of the former. The wavelength tunable between 375 and 395 nm was tuned to 385 nm in the experiment, and the time resolution of the whole system was about 30 ps.

The time-resolved luminescence intensity can be fitted with two exponential-decay components. The radiative lifetime of the direct recombination was theoretically predicted to be the order of 100 ps[2]. The fast component is due to the direct recombination and was observed to be dependent on temperature as shown in Fig. 1. At low temperatures below 45($\pm$ 5) K, the almost constant decay constant about 60 ps and it becomes longer as temperature increases above 45 K. This temperature dependence is very similar to that of Frenkel excitons in molecular aggregates reported by de Boer et al.[3]. They explain this temperature dependence in terms of dephasing-induced quenching of excitonic superradiant emission. This explanation may be applicable to the Wannier excitons in semiconductors, which delocalizes coherently over the microcrystallite. In this case, the coherently extended volume of an exciton (coherent volume) proportional to the radiative decay rate is limited by the exciton scattering with acoustic phonons.

We propose that the decrease in the radiative decay rate above 45 K can be interpreted by an interaction between an exciton and a vibrational mode frequency of the microcrystallites. The acoustic-phonon mode in the micro-

crystallites is also discrete, because the microcrystallites are well isolated from the matrix polymer and the phonons are confined. The lowest phonon mode coupling with electron may be radial compression mode of a microcrystallite. Assuming each microcrystallite to be an elastic sphere, the frequency of radial mode is estimated as

$$\omega = (\pi/R)v_l \qquad (1)$$

where R is the particle radius and v_l is the longitudinal sound velocity (for CdS at 5 K, $v_l = 4.50 \times 10^5$ cm/s [4]). For a microcrystallite of R = 20 ± 4 A, the phonon frequency is 37 ± 7 cm^{-1}, which corresponds to 54 ± 10 K. The value of one-phonon frequency (54 ± 10 K) is in good agreement with experimentally obtained threshold temperature (45 ± 5 K). Below the temperature corresponding to the one-phonon frequency, a coherently extended exciton cannot be scattered with the acoustic phonon. The constant lifetime is observed because no dephasing-induced quenching of the superradiance occurs at such low temperatures. On the other hand above the threshold temperature, the phonons are populated in the crystallites. Thus the radiative decay rate decreases with temperature because of the more efficient quenching of the superradiance by exciton-phonon scattering at higher temperature. The confined-phonon model was applied by Alivisatos et al. to explain temperature dependence of the homogeneous linewidth of exciton transition in CdSe microcrystallites[5]. We previously analyzed the ultrafast dephasing time in CdS microcrystallites at 2 K also by the confined-phonon model[6]. We believe that the threshold temperature of the superradiance in CdS microcrystallites is a proof of the phonon confinement.

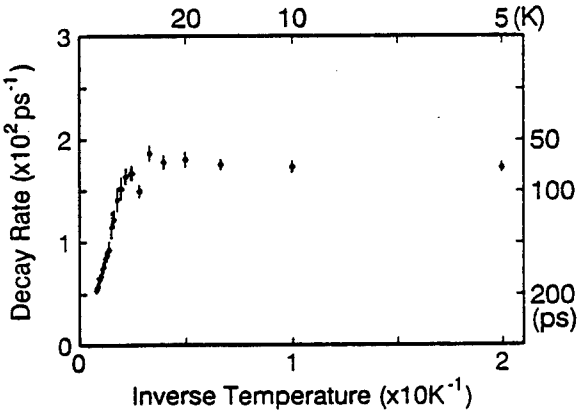

Fig. 1. Temperature dependence of radiative decay rate.

3. Electroabsorption

The samples used for the study of electroabsorption are CdS_xSe_{1-x} (x=0.12 ± 0.05) microcrystallites in the glass plates of 300 μm thick. The size of them was controlled by heat treatment. A sinusoidal wave with a 1.2-kV peak voltage and a frequency (f) 500-Hz was applied parallel to the surface of the samples between a pair of aluminum electrodes with a 0.48-mm gap. The light was introduced between the electrodes and the change in transmission was measured with a lock-in amplifier in the 2f mode.

The absorption spectra of samples shows two vague shoulders are seen around 1.9 - 2.0 eV and 2.3 - 2.4 eV, which correspond to exciton peaks. In

the transmittance change spectra, the exciton peaks, which are ambiguous in ordinary absorption spectra, are clearly resolved. Both broadening and energy shift are observed.

As the particle size, R, increases, the Coulomb potential becomes important, and as the size decreases, the confining potential becomes dominant. When no external field is applied (F=0), the energy, E, has been calculated by Brus[7] and Kayanuma,[8] assuming a spherical shape, to be

$$E = -E^{*}_{Ry} + \frac{h^2\pi^2}{2MR^2} \qquad (2)$$

in the limit of weak confinement ($R>>a_B$), and,

$$E = \frac{h^2\pi^2}{2\mu R^2} - 1.786\,\frac{e^2}{4\pi\varepsilon R} - 0.248E^{*}_{Ry} \qquad (3)$$

in the limit of strong confinement ($R<<a_B$).[3] Here, μ is the reduced mass, M is the total mass and R is the particle radius. These values and experimentally observed blue shift are shown in Fig. 2.

The broadening is due to exciton dissociation by the electric field. In the bulk case, excitons are rapidly ionized by the electric field, but in the confined case, exciton peaks are persistent up to a very high field. The tunneling rate through barriers is estimated using the barrier height of 1 eV and the mean distance between microcrystallites of 500 A. The change in the width of exciton transition was found to be far smaller than the experimental result. There is a possibility of tunneling to the states by the surrounding CdS_xSe_{1-x} clusters around the microcrystallites contributing to broadening, or increase of surface recombination rate due to change in the charge distribution.

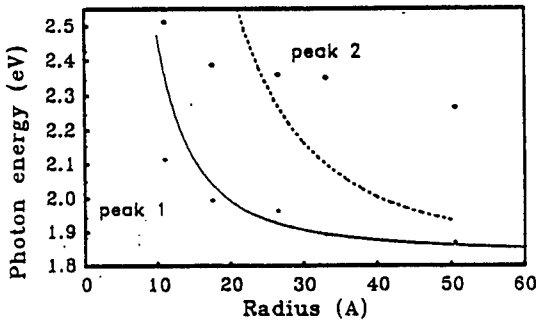

Fig. 2. The size dependence of the peak position of excitons. The solid line is calculated using eq.2, and the dotted line using eq.3. Closed and open circles are experimentally observed peak photon energies of excitons.

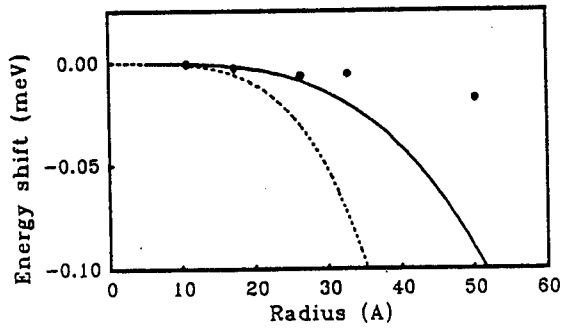

Fig. 3. Dependence of the energy shifts induced by an external electric field. The solid curve is the theoretical calculation including the polarization energy and the Coulomb interaction, the dotted curve is the theoretical calculation without these interactions, and dots are the experimental results in Ref. 9.

The Stark shift is estimated in the literature.[9] In the calculation, we assumed the effective mass approximation with simple parabolic bands both for a conduction band and for valence bands, an infinitely high confining potential. Both the dielectric confinement effect due to the difference in dielectric constants between microcrystallites and the surrounding matrix and the Coulomb interaction between an electron and a hole were considered. The result is shown in Fig. 3. It is shown that the Coulomb interaction plays a significant role for a microcrystallites with radius as small as one third of the effective Bohr radius of the exciton.

The broadening of the exciton transition in the microcrystallites was investigated from the view point of the exciton-LO phonon coupling experimentally and theoretically. The estimated strength of the exciton-LO phonon coupling is of key important for the realization of large nonlinear susceptibility, because the oscillator strength is redistributed through the exciton-LO phonon interaction, which results in the reduction in the nonlinear susceptibilities. The temperature dependencies of the exciton energy and the width were obtained. They exhibited bulk-like temperature dependence as shown in Figs. 4 and 5. Qualitatively, the energy shift and the change in the width by temperature change are reduced from the bulk values because of the quantum confinement effects. The exciton phonon coupling constant was calculated with variational functions in finite height confining potential. It was shown that the coupling to LO phonon increases with decreasing a microcrystallite size as shown in Fig. 6.

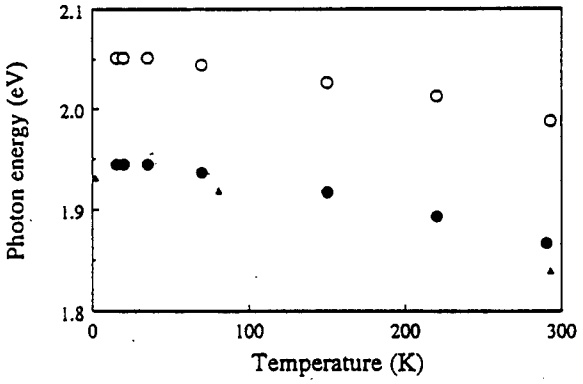

Fig. 4. Temperature dependence of the exciton energy of microcrystallites of radius of 17.5 A (open circles) and 50.5 A (closed circles), respectively. The bulk band gap from Ref. 4. is also depicted (triangles).

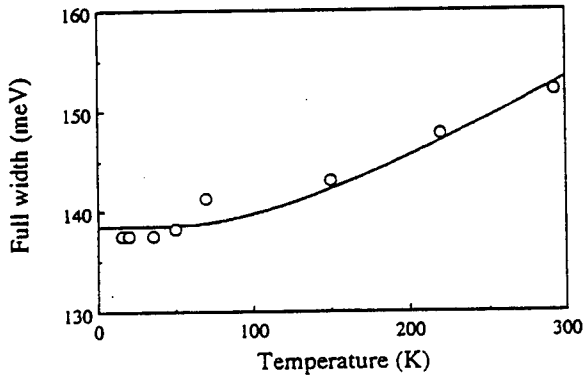

Fig. 5. Temperature dependence of the exciton width of microcrystallites of radius of 17.5 A (open circles). The solid curve is the best fitted curve using the LO phonon energy of 28 meV.

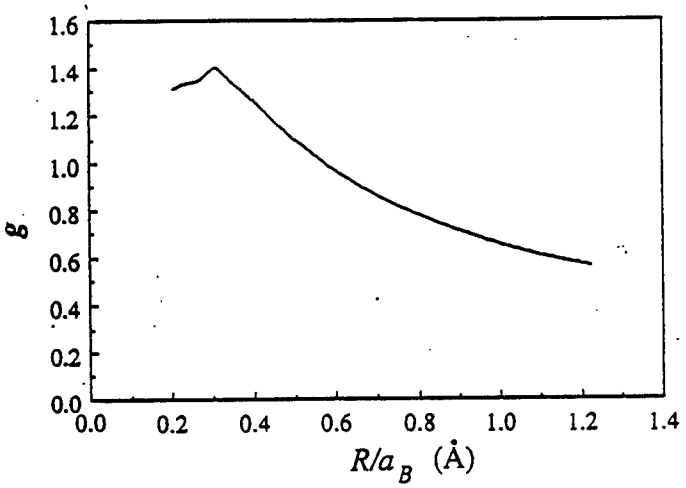

Fig. 6. The calculated size dependence of the coupling constant.

References

1. K. Misawa, H. Yao, T. Hayashi, and T. Kobayashi, J. Chem. Phys. submitted.
2. T. Takagahara, Phys. Rev. B **36** 9293 (1987)
3. S. de Boer and D.A. Wiersma, Chem. Phys. Lett. **165**, 45 (1990)
4. Landort-Bornstein Numerical Data and Functional Relationships in Science and Technology, ed. by K.H. Hellwege (Springer, Berlin, 1982), New Series, Vol. 17b
5. A.P. Alivisatos, A.L. Harris, N.J. Levinos, M.L. Steigerwald, and L.E. Brus, J. Chem. Phys. **89**, 4001 (1988)
6. T. Kobayashi, S. Nomura, and K. Misawa, SPIE Proceedings vol.1216, p.105 (1990)
7. L. Brus, *J. Phys. Chem.* **90**, 2555 (1986).
8. Y. Kayanuma, *Solid State Commun.* **59**, 405 (1986).
9. S. Nomura and T. Kobayashi, *Solid State Commun.* 73, 425 (1990), *ibid* 74, 1153(1990).

GLASSES FOR NONLINEAR OPTICAL DEVICES

EVA M. VOGEL
BELLCORE
RED BANK, NJ 07701, USA

The success of all-optical switching depends on the development of the materials and devices that are capable to process light signal without converting it to electronic form.

The recent demonstration of several logic elements, such as an ultrafast dual-core fiber nonlinear coupler and spatial optical solitons, has focused attention on glasses as nonlinear photonic materials.

Glasses are desirable material for these all – optical devices because of their fast responding nonlinearities and low absorption. The relative merits and the tradeoff of glasses for these applications will be discussed in general. The effect of structure and composition on the nonlinear optical properties of glasses will be discussed in detail.

Optical Characteristics on CdS_xSe_{1-x}-Doped Glasses

NTT Basic Research Labs.
Junji Yumoto

Reprinted from Optics Letters, Vol. 12, page 832, October 1987.

Observation of optical bistability in CdS_xSe_{1-x}-doped glasses with 25-psec switching time

Junji Yumoto

NTT Electrical Communications Laboratories, Musashino-shi, Tokyo 180, Japan

Seiji Fukushima

NTT Electrical Communications Laboratories, Tokai-mura, Ibaraki 319-11, Japan

Ken-ichi Kubodera

NTT Electrical Communications Laboratories, Musashino-shi, Tokyo 180, Japan

Received March 11, 1987; accepted July 9, 1987

We report the first observation to our knowledge of optical bistability in CdS_xSe_{1-x}-doped glasses with rise and fall times of 25 psec for bistable switching. The third-order nonlinear susceptibility $\chi^{(3)}$ was estimated experimentally to be 1.3×10^{-9} esu, which is in good agreement with the value reported previously. The high-speed switching and value of $\chi^{(3)}$ show that the bistability is caused by an optical nonlinearity that is attributed to the band-filling effect.

There is a great deal of interest in developing high-speed and low-power optical bistable devices for future optical signal-processing and optical communications systems. Glasses doped with semiconductor microcrystalline CdS_xSe_{1-x}, which are commercially available as sharp-cut filters, have recently attracted much interest because of their large third-order nonlinearities and fast response times. Jain and Lind have reported that the third-order susceptibilities $\chi^{(3)}$ were measured to be 10^{-9}–10^{-8} esu in a degenerate four-wave mixing (DFWM) experiment and that the origin of the nonlinearity can be attributed to the generation of a short-lived electron–hole plasma (band-filling effect).[1] Yao *et al.* have estimated the free-carrier lifetimes to be less than 16 psec based on the results of the luminescence and the DFWM grating experiments.[2]

Optical bistabilities in CdS_xSe_{1-x}-doped glasses have been reported by McCall and Gibbs[3] and by Gibbs *et al.*[4] The mechanism of the optical nonlinearity in their experiments, however, was a thermal effect, and therefore the switching time of the observed optical bistability was in the range of a few milliseconds or a few seconds.

In this Letter we report the first observation to our knowledge of optical bistability made using a Fabry–Perot cavity containing CdS_xSe_{1-x}-doped glasses. The switching time of the optical bistability is 25 psec, and the value of $\chi^{(3)}$ in CdS_xSe_{1-x}-doped glasses is estimated from the experiment to be 1.3×10^{-9} esu. The observed switching speed and the value of $\chi^{(3)}$ are consistent with those due to the band-filling effect.

Figure 1 shows a schematic diagram of the experimental setup. To observe the ultrafast optical bistability, we developed an experimental setup using a mode-locked and Q-switched YAG laser and a streak camera. As a light source, we used the second-harmonic-generated (SHG) light (532 nm) with a pulse width of 150 psec (FWHM), pumped by a mode-locked (82-MHz) and Q-switched (900-Hz) YAG laser (1064 nm). CdS_xSe_{1-x}-doped glasses (commercial sharp-cut filters, Hoya Y-50, Y-52, and O-54) with antireflection coatings on both endfaces were inserted into a 600-μm-long Fabry–Perot cavity consisting of 90%-reflectivity plane-parallel mirrors. The cavity length was changed by using a piezo pusher to vary the initial detuning. Each 300-μm-thick sample had an absorption of 2% (absorption efficiency $\alpha = 0.7$ cm^{-1}), 4% ($\alpha = 1.4$ cm^{-1}), and 20% ($\alpha = 7.4$ cm^{-1}) for Y-50, Y-52, and O-54, respectively, at a wavelength of 532 nm. The diameter of the input beam incident upon

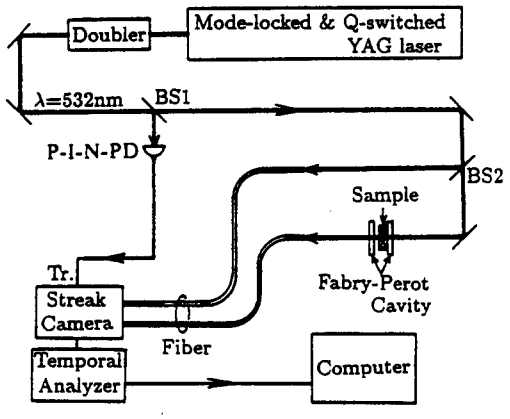

Fig. 1. Experimental setup for the observation of optical bistability in CdS_xSe_{1-x}-doped glass.

0146-9592/87/100832-03$2.00/0

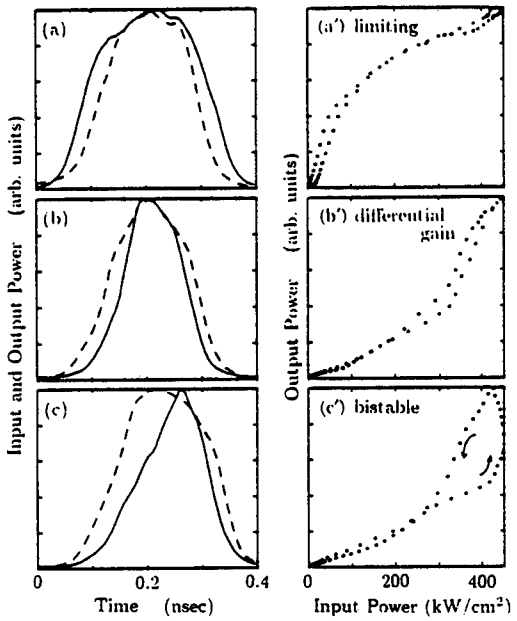

Fig. 2. Left: Input pulses (dashed lines) and output pulses (solid lines) for sample Y-52. The maximum value of each line was normalized to 1. Right: Input–output characteristics. (a'), (b'), and (c') correspond to (a), (b), and (c), respectively. The dot-to-dot time interval in (a')–(c') is 6.2 psec.

the sample was 1 mm. The input pulse to a P-I-N photodiode (PD) split by beam splitter BS1 was used as a trigger for the streak camera. The waveforms of the input and transmitted pulses guided by optical fibers were detected simultaneously by the streak camera. Time-dependent intensity profiles of both signals stored in the temporal analyzer were transferred to a computer to analyze the input–output characteristics.

Figures 2(a)–2(c) show the observed input and transmitted pulse waveforms obtained by varying the initial detuning of the cavity length from off resonant to on resonant. The corresponding input–output characteristics obtained from these waveforms are shown in Figs. 2(a')–2(c'), and the transition of the input–output characteristics from limiting, differential gain to bistability was observed. The sample tested was Y-52, and the peak input power was 450 kW/cm^2. The threshold power for the bistable jump was strongly dependent on the initial detuning. Figure 3 shows the bistable input–output characteristics having the lowest threshold power of the results obtained. At the bistable jumps, both the rise and the fall times are estimated to be 25 psec, as shown in Fig. 3.

The value of this fall time is in good agreement with the calculated value of $\tau_s = (\tau_c^2 + \tau_r^2)^{1/2} = 18$ psec, where τ_c is a cavity-decay time of ~ 10 psec (assuming an effective mirror reflectivity of 0.73 from the measured finesse, $F \sim 10$) and $\tau_r = 16$ psec is the fastest reported value of the carrier lifetime in CdS_xSe_{1-x}-doped glasses.[2] Recently the darkening effect of CdS_xSe_{1-x}-doped glasses was reported, indicating that the nonlinear response was slow for a fresh sample and was very fast (~50 psec) after a long laser exposure.[5] Therefore we consider that the slow component of the carrier lifetime in our sample was completely suppressed during our experiment. Relatively slow switching characteristics such as those shown in Fig. 2(c') are attributed to the critical slowing down.

In Y-50 the limiting, differential gain and bistability were also observed, and we could not see much difference in the threshold power for optical bistability between Y-50 and Y-52. We observed only the limiting, differential gain in O-54, which had the largest absorption among the measured samples. It is thought that the absorption in the 300-μm-thick O-54 reduced the finesse of the Fabry–Perot cavity, and thus much more input power was required to produce optical bistability, even though the larger absorption in O-54 increased the optical nonlinearity. Actually, by using the experimental values of an absorption of 20% and a finesse of 7, it is possible to estimate that O-54 requires about 20 times as much power as Y-52 to produce optical bistability. Note that the optimum conditions for an optical bistable device depend not only on matching of the photon energy and the absorption edge energy but also on the finesse of the Fabry–Perot cavity.

The value of $\chi^{(3)}$ in CdS_xSe_{1-x}-doped glasses is estimated. Assuming that the mean internal intensity in the Fabry–Perot cavity $I_{int} = 3$ MW/cm^2 (estimated from the effective mirror reflectivity) and that the nonlinear round-trip phase shift $\phi_{NL} \simeq 2\pi/F = \pi/5$ (the full width at half-maximum of the Fabry–Perot cavity transmission peak), the nonlinear index of refraction n_2 of 3×10^{-8} (cm^2/kW) is obtained from

$$2ln_2k_0I_{int} = \phi_{NL} \simeq \pi/5,$$

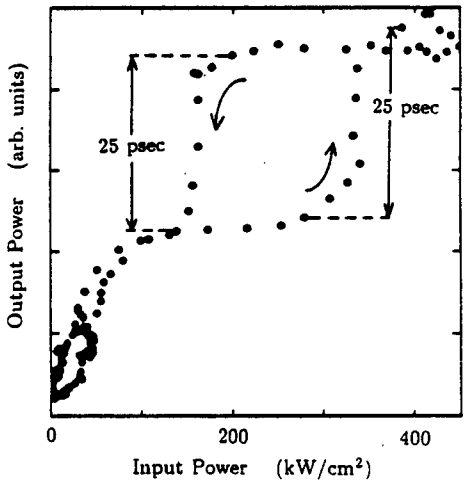

Fig. 3. Optical bistability with 25-psec switching time. The dot-to-dot time interval is 3.1 psec. There are eight such intervals in on and off jumps.

where l is the thickness of the CdS_xSe_{1-x}-doped glass and k_0 is the propagation constant. The value for n_2 yields a $\chi^{(3)}$ value of 1.3×10^{-9} esu, which is in good agreement with the reported value of 10^{-9}–10^{-8} esu.[1] This $\chi^{(3)}$ and the high-speed switching show that the optical nonlinearity in CdS_xSe_{1-x}-doped glasses can be attributed to the band-filling effect.

From the present experiment we can estimate the switching energy in CdS_xSe_{1-x}-doped glasses to be 10 pJ, if we assume a 10 μm × 10 μm area for 1-bit operation. This value is equivalent to that for optical bistability in GaAs bulk material[6] that is due to the band-filling effect. This value can be reduced by optimizing the radius and the concentration of the microcrystalline CdS_xSe_{1-x}.

In conclusion, optical bistability in CdS_xSe_{1-x}-doped glasses was demonstrated using a 600-μm-long Fabry–Perot cavity. The rise and fall times of the bistable switching were both 25 psec, and the value of $\chi^{(3)}$ was 1.3×10^{-9} esu. The switching energy was estimated to be 10 pJ, assuming a 1-bit area of 10 μm × 10 μm.

The authors are indebted to Hiroshi Kanbe and Masaharu Mitsunaga for their comments.

References

1. R. K. Jain and R. C. Lind, J. Opt. Soc. Am. 73, 647 (1983).
2. S. S. Yao, C. Karaguleff, A. Gabel, R. Fortenbery, C. T. Seaton, and G. I. Stegeman, Appl. Phys. Lett. 46, 801 (1985).
3. S. L. McCall and H. M. Gibbs, J. Opt. Soc. Am. 68, 1378 (A) (1978).
4. H. M. Gibbs, G. R. Olbright, N. Peyghambarian, H. E. Schmidt, S. W. Koch, and H. Haug, Phys. Rev. A, 32, 692 (1985).
5. P. Roussignol, D. Ricard, J. Lukasik, and C. Flytzanis, J. Opt. Soc. Am. B 4, 5 (1987).
6. Y. H. Lee, H. M. Gibbs, J. L. Jewell, J. F. Duffy, T. Venkatesan, A. C. Gossard, W. Wiegmann, and J. H. English, Appl. Phys. Lett. 49, 486 (1986).

Reprinted from Journal of the Optical Society of America B, Vol. 5, page 1448, July 1988

Laser annealing effect on carrier recombination time in CdS_xSe_{1-x}-doped glasses

Masaharu Mitsunaga, Hiroyuki Shinojima, and Ken-ichi Kubodera

NTT Basic Research Laboratories, Musashino-shi, Tokyo 180, Japan

Received July 31, 1987, accepted March 3, 1988

The carrier recombination time of CdS_xSe_{1-x}-doped glasses has been studied in detail by using laser-induced-grating and pump–probe measurements. Decay curves have been found to show strong sharpening as a function of the laser-pulse exposure time. A slow decay of a few nanoseconds in the first stage is quenched during the irradiation, and finally a fast decay as short as 7 psec remains. Simple three-level rate equations, including the valence band, the conduction band, and the intermediate trap level, are proposed to explain the observation that this annealing effect may be parameterized by the conduction-to-trap-level decay time.

1. INTRODUCTION

Since the pioneering work by Jain and Lind,[1] semiconductor-doped glasses (SDG's) have been studied quite extensively as nonlinear-optical materials. In addition to relatively large nonlinear susceptibility $\chi^{(3)}$, the carrier lifetime T_1 of this material has been controversial. Yao *et al.*[2] claimed first that T_1 is as short as a few tens of picoseconds. Cotter[3] showed that the decay time depends on the excitation intensity and varies from 10 nsec to 10 psec as the intensity is elevated. Fast recombination lifetime was also supported by the absorption recovery in the femtosecond pump–probe (PP) technique[4,5] and by the observation of 25-psec optical bistable switching by Yumoto *et al.*[6] On the other hand, the existence of a slow decay longer than 1 nsec was also reported.[7]

Recently, Roussignol *et al.*[8] bridged the gap between these two viewpoints and provided a reasonable explanation. They found an optical darkening effect by which a SDG experiences a quasi-irreversible exposure process of the laser-pulse irradiation and indicated that the trap levels play a key role in the carrier recombination processes in SDG. Shortening of the recombination times from the nanosecond to the picosecond region could well be interpreted as the unavailability of these trap centers. In fact, in commercial color-glass filters, the existence of vast trap levels, likely due to surface-related defects,[9] a few hundred millielectron volts below the band gap seems to mask the band-to-band recombination process in the first stage of laser irradiation. Our independent photoluminescence studies on two commercial color-glass filters (Hoya and Corning) revealed that the contribution of luminescence from trap levels is overwhelmingly great; thus the luminescence from the band edge is sometimes almost negligible.

We systematically analyzed this laser-pulse annealing effect of the SDG trap levels by a laser-induced-grating (LIG) method and a PP method by using a picosecond laser system. Signal decay curves were monitored for different laser-pulse exposure times. Certainly, irradiation by a moderately intense light has been found to alter the microscopic structure of this material gradually and, consequently, the recombination processes, in a nonreversible manner. After a few hours of irradiation, a recombination time as short as 7 psec was observed. We believe this to be the shortest recombination time ever observed in SDG. A theoretical model is also proposed, assuming simple rate equations, including the valence band, the conduction band, and the intermediate level. In this model the annealing effect can be explained by the reduction of the conduction-to-trap-level decay times.

2. EXPERIMENTAL SETUPS

Two types of experimental setup for the decay-time measurements are shown in Fig. 1, i.e., a LIG method and a PP method.

As a light source, an Ar synchronously pumped mode-locked dye laser with a cavity dumper was employed. According to autocorrelator detection, the pulse duration was approximately 5 psec. The repetition rate of cavity dumping was set at 800 kHz for a clean, quiet signal. The average power at the sample point was approximately 1 mW for each beam in a LIG. In the PP measurement the pump–probe power was 3 mW/80 μW and was variable by a half-wave (λ/2) plate. The beam was focused to a spot size of 30–100 μm.

The samples were commercial Hoya (058, R60, R62, and R64) and Corning (nine different filters with sharp cuts around 600 nm) color-glass filters. LIG signals could be identified for any of the above. Generally, Corning filters yielded an order of magnitude larger signal and could be seen even with the naked eyes. (The signal power was typically 70 nW for the 2-61 sample.) The annealing effect was much more pronounced in Hoya filters, however. These facts may suggest that Hoya filters have fewer long-lived trap centers that can be easily annealed. The following fluorescence study also supported this proposition. Corning filters had large photoluminescence spectra due to trap levels in the near infrared along with almost negligible band-edge luminescence, whereas the trap-level luminescence of Hoya filters was small compared with that from the band edge but covered almost all the visible-to-near-infrared spectrum, starting just below the band edge.

0740-3224/88/071448-05$2.00

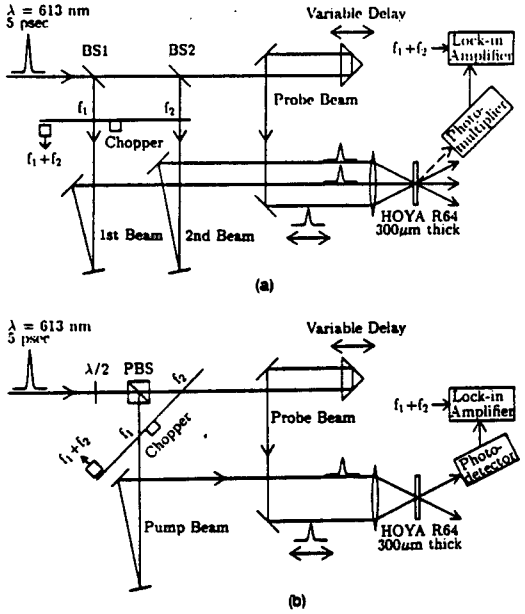

Fig. 1. (a) Experimental apparatus for LIG measurement: BS1, BS2, beam splitters. (b) Experimental apparatus for PP measurement: λ/2, half-wave plate; PBS, polarizing beam splitter.

Samples with a thickness of 0.3 mm were employed to investigate the above-band-gap behavior of carriers with ~50% transmission (α = 30 cm^{-1}). This is important because usual 2.5-mm-thick samples give 50% transmission for the photon energy far below the band edge. Although the following analysis was made using a 0.3-mm-thick Hoya R64 filter, similar behavior was observed in Corning filters and in 2.5-mm-thick samples.

In the LIG method the phase-matched diffracted beam of the delayed pulse was monitored by a photomultiplier in the folded-boxcars configuration.[10] In the PP method the transmission intensity of the probe pulse was detected by a photodetector. The cross-modulation technique[11] for lock-in detection helped to improve the signal-to-noise (S/N) ratio. For data taking, a personal computer was used to drive the pulse stage of the optical delay line, and for each step the output of the lock-in amplifier was sent to a digital voltmeter, which in turn was stored in the computer. These experimental setups were also useful for the measurement of T_2 by using two-beam incident degenerate four-wave mixing. By slightly modifying the setup, we could measure the T_2 of a SDG sample; however, this measurement was masked by our resolution time of 2 psec.

3. EXPERIMENTAL RESULTS

Typical experimental results are shown in Figs. 2(a) and 2(b) for the LIG case and the PP case, respectively. Theoretically, the main differences between the LIG and PP measurements are (1) LIG measures the quantity proportional to $|\chi^{(3)}|^2$,[12] whereas PP measures the imaginary part of $\chi^{(3)}$, i.e., transient change in the absorption coefficient; (2) for a two-level system, LIG measures $T_1/2$, whereas PP measures T_1. The decay times, therefore, differ by a factor of 2 for the two cases. For a three-or-more-level system, the situation becomes more complicated.

The LIG result is shown in Fig. 2(a). Because the polarizations of the three beams are parallel, spikes can be seen at the delay time $\tau_d = 0$ because of the diffraction of the second pulse by the grating generated by the first and the probe pulses. As can be clearly seen, the decay time right after laser exposure is on the order of 1 nsec. With time, however, this component is reduced dramatically, and, after a 3-h exposure, it becomes almost completely suppressed, and only the fast component survives. It is also clear that the signal peak intensity decreases by approximately one third as a function of the exposure time. A few more hours, exposure had no effect on the decay behavior.

The PP result is shown in Fig. 2(b). Here again the annealing effect is obvious. The slow decay in the first stage ended up with an ~20-psec decay, which agrees with the final curve of Fig. 2(a), considering that PP measures twice the decay time of LIG. Because of the resolution of our system and the laser wavelength almost equal to the band gap, the subpicosecond intraband relaxation[4,5] or the thermalization of hot electrons should not be seen. Because this method is not a background-free method, the S/N ratio is poor compared with that of LIG. The way to circumvent this poor S/N ratio is to reduce the spot size of the beam. This is possible only in the PP method since the LIG method requires a larger spot size (~100 μm) in order to provide a well-defined interference pattern inside the spot. For example, the distance of the interference fringe is 30 μm for a 20-mrad intersection angle of two beams of 600 nm. This small spot size (~30 μm) in PP is reflected on the annealing time of the sample. An order-of-magnitude reduction of the annealing time was observed in this case as shown in the figure. To measure the decay time for short exposure time, say 10 sec, the sample was moved from spot to spot after 10 sec of irradiation for each delay time of the probe pulse.

The shortest decay time using LIG was realized in the very final stage of our experiment with the help of a hybridly mode-locked dye laser[13] with a pulse width of 1.5 psec using DQOCI dye as a saturable absorber. The decay curve is displayed in Fig. 2(c) along with the laser pulse and the best-fit theoretical plot based on the theory mentioned in Section 4. The recombination time thus obtained yielded a value of 7 psec. We did not observe any input intensity dependence of the final decay time; reduction of the incident power by one fourth did not change the decay behavior. The annealing effect is sometimes evident by a glance at the lock-in amplifier, where the reading decreases in several seconds by a laser irradiation and immediately recovers by a quick movement of the sample position from an annealed spot to a fresh spot. Annealing time depends on beam spot size and laser-pulse repetition rate, thus indicating that it simply depends on peak power density times total exposure time. A similar type of annealing was also made possible by a mode-locked Ar laser. We did not observe, however, the darkening effect[8] as Roussignol *et al.* did. Neither did we observe any change in the transmission spectrum even after the annealing, suggesting that this effect should be distinguished from optical damage.

To show that this annealing effect is irreversible, the fol-

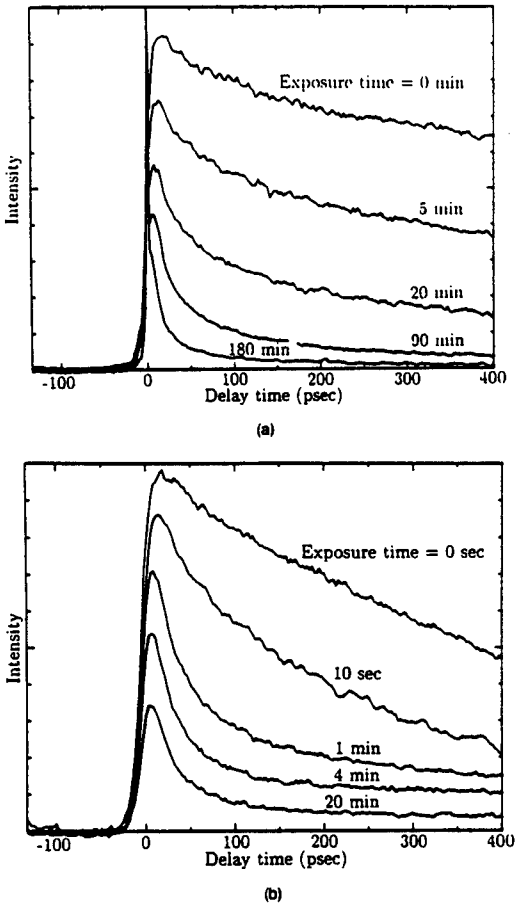

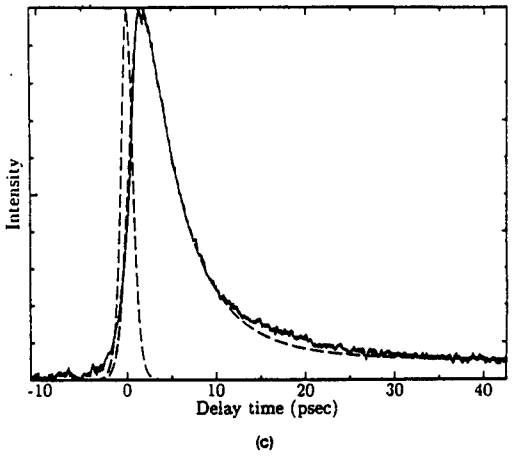

Fig. 2. Signal intensity versus probe-pulse delay time τ_d for a 300-μm-thick Hoya R64 sample (λ = 613 nm): (a) decay curves for various exposure times in the LIG measurement, (b) decay curves for various exposure times in the PP measurement, (c) shortest decay signal (solid line) observed in LIG, excitation laser pulse (narrow dashed line) and theoretical best-fit curve (broad dashed line). The coherent spike at a delay time of 0 is unseen because of the perpendicular polarization of the probe beam with respect to the first and second beams. Average powers of the first, second, and probe beams were 3.6, 1.4, and 0.3 mW, respectively. The repetition rate was 4 MHz. The signal was averaged over five times. The laser pulse width was 1.5 psec. For plotting, a sech^2 pulse shape was assumed.

lowing experiment was performed. After a few hours of exposure of one sample spot, the laser beam was blocked for another few hours. Then the LIG signal was monitored as a function of the sample position by transversely moving the sample around the annealed spot by using a translation stage. This time, the probe delay time was kept to 100 psec. The result is shown in Fig. 3. It can be clearly seen that only the annealed spot shows an almost zero signal (the decay time is much shorter than 100 psec), whereas fresh spots show quite a large signal. Considering that the spot size in this experiment was approximately 70 μm, we can conclude that this effect is neither related to the diffusion nor thermal in origin, but instead the exposed spot experiences some kind of irreversible photochemical annealing process.

4. DISCUSSION

Although the laser annealing effect is experimentally obvious, its physical origin is still uncertain. This uncertainty stems directly from the fact that the microscopic structure of semiconductor crystallite in the glass material is not yet known. Apparent deviation from a simple single exponential decay implies that the system cannot be described by a valence-to-conduction two-level system. The importance of intermediate levels is clear from the fluorescence studies. Finally, the decaying mechanism gradually changes by the laser irradiation.

After consideration of all these facts, the most probable

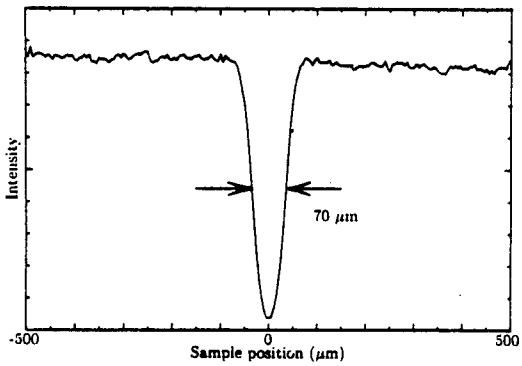

Fig. 3. Diffracted signal intensity versus sample position x in the LIG measurement. The probe delay time was fixed at τ_d = 100 psec. At 2 h before the measurement, the spot at x = 0 had been annealed for a few hours.

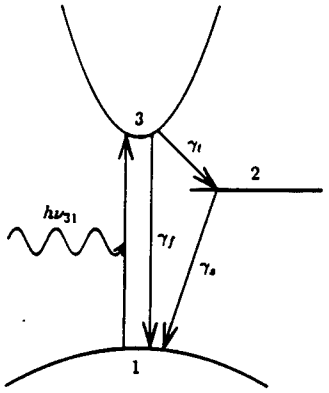

Fig. 4. Energy levels participating in the carrier recombination processes in SDG. Laser excitation promotes the electrons to level 3. The electrons, thereafter, either directly recombine to level 1 or get trapped by level 2 and decay back to level 1.

proposal at this stage, admitting that the experimental support is not enough, is the three-level system, including the valence band (level 1), the trap level (level 2), and the conduction band (level 3). This is shown schematically in Fig. 4. First, the laser pulse generates free carriers in the conduction band. Thermalization of hot carriers (<1 psec) is ignored. Thereafter the carriers will either go directly down to the valence band at a fast decay rate γ_f or will take a bypass to the trap levels at a rate γ_t and then return to the valence band with a relatively slow rate γ_s. Denoting the populations of carriers in the valence band, trap level, and conduction band as n_1, n_2, and n_3, respectively, we can write the rate equations as[14]

$$\frac{dn_3}{dt} = \beta I(t) - \gamma_f n_3 - \gamma_t n_3,$$

$$\frac{dn_2}{dt} = \gamma_t n_3 - \gamma_s n_2,$$

$$n_1 + n_2 + n_3 = N, \tag{1}$$

where $\beta = \sigma_{31}N/h\nu_{31}$, with σ_{31} being the absorption cross section for the optical transition of frequency ν_{31}. The total number of carriers is represented by N. $I(t)$ is the time-dependent pulse intensity and is assumed to be weak enough not to alter the value n_1 much. When the pulse is on, the solution to the above set of equations is given in an integral form. After the pulse, $I(t) = 0$ in the above equation, and the analytical solution is available. The solutions for $n_3(t)$ and $n_2(t)$ during the laser pulse are

$$n_3(t) = \beta \int_{-\infty}^{t} dt_1 I(t_1)\exp[-(\gamma_f + \gamma_t)(t - t_1)],$$

$$n_2(t) = \beta\gamma_t \int_{-\infty}^{t} dt_1 \int_{-\infty}^{t_1} dt_2 I(t_2) \times \exp[-(\gamma_f + \gamma_t)(t_1 - t_2) - \gamma_s(t - t_1)]. \tag{2}$$

On the other hand, the solutions after the pulse has ceased at $t = \tau_p$ are

$$n_3(t) = n_3(\tau_p)\exp[-(\gamma_f + \gamma_t)(t - \tau_p)],$$

$$n_2(t) = \frac{\gamma_t}{\gamma_f + \gamma_t - \gamma_s} n_3(\tau_p)[\exp[-\gamma_s(t - \tau_p)] - \exp[-(\gamma_f + \gamma_t)(t - \tau_p)]] + n_2(\tau_p)\exp[-\gamma_s(t - \tau_p)]. \tag{3}$$

As shown in the luminescence measurements[8] before and after the laser irradiation by Roussignol *et al.*, the number of trap levels is supposedly reduced in the process of exposure. Because the free-carrier collisional cross section with trap levels is reduced, it indicates that the decay rate γ_t to trap levels is also reduced. In this way the annealing effect can be physically understood by parameterizing the quantity γ_t. However, to obtain, theoretically, LIG signals for a three-level system such as this, the exact information of the energy-level structure of trap levels is necessary. Because the experimental data of the trap-level structure are not available, the actual fitting is not given here. We could, however, at least qualitatively see the decaying behavior from Eq. (3). When γ_t is large comparable with γ_f, the first term in the expression of n_2 is not negligible, and the dominant contribution arises from n_2, which exhibits a slow decay. As γ_t is reduced, then n_3 becomes important, and the carriers decay back to the valence band quickly.

5. CONCLUSION

In conclusion, the strong dependence of carrier lifetime on laser-beam exposure time was systematically studied and analyzed in SDG samples. Steepening of the decay curves in the few-nanosecond region to less than 10 psec is attributed to the irreversible laser annealing effect of the sample, i.e., extinction of the intermediate levels. This behavior was common in the LIG and PP measurements. The ultimate recombination time observed was estimated as 7 psec, one of the shortest ever observed in any material. Finally, it should be stressed that this annealing process is favorable from the viewpoint of optical devices, since reduction of response time is dominant over reduction of nonlinearity, i.e., the signal peak intensity becomes one third [see Fig. 2(a)] after annealing, whereas the speed (decay time) is enhanced ~1000 times! We believe that this effect as well as the diffusion-free property of SDG's makes them promising for use as nonlinear-optical materials.

ACKNOWLEDGMENTS

We would like to thank H. Kobayashi for making the photoluminescence measurement used in this study. We also are thankful for the contributions of H. Kanbe and T. Takagahara in stimulating discussions.

REFERENCES

1. R. K. Jain and R. C. Lind, J. Opt. Soc. Am. 73, 647 (1983).
2. S. S. Yao, C. Karaguleff, A. Gabel, R. Fortenberry, C. T. Seaton, and G. I. Stegeman, Appl. Phys. Lett. 46, 801 (1985).
3. D. Cotter, J. Opt. Soc. Am. B 3(13), P246 (1986).
4. M. C. Nuss, W. Zinth, and W. Kaiser, Appl. Phys. Lett. 49, 1717 (1986).
5. N. Peyghambarian, G. R. Olbright, and B. D. Fluegel, J. Opt. Soc. Am. B 3(13), P248 (1986).
6. J. Yumoto, M. Mitsunaga, and K. Kubodera, in *Digest of Con-*

ference on Lasers and Electro-Optics (Optical Society of America, Washington, D.C., 1987), paper ThU15.
7. P. Roussignol, D. Ricard, K. C. Rustagi, and C. Flytzanis, Opt. Commun. **55**, 143 (1985).
8. P. Roussignol, D. Ricard, J. Lukasik, and C. Flytzanis, J. Opt. Soc. Am. B **4**, 5 (1987).
9. J. Warnock and D. D. Awschalom, Phys. Rev. B **32**, 5529 (1985).
10. See, for example, J. E. Goloub and T. W. Mossberg, J. Opt. Soc. Am. B **3**, 554 (1986).
11. S. Asaka, H. Nakatsuka, M. Fujiwara, and M. Matsuoka, Phys. Rev. A **29**, 2286 (1984).
12. D. S. Chemla, D. A. B. Miller, P. W. Smith, A. C. Gossard, and W. Wiegmann, IEEE J. Quantum Electron. **QE-20**, 265 (1984).
13. Y. Ishida and T. Yajima, Opt. Commun. **58**, 355 (1986).
14. A. J. Taylor, D. J. Erskine, and C. L. Tang, Appl. Phys. Lett. **43**, 989 (1983).

Microcrystallite size dependence of absorption and photoluminescence spectra in CdS_xSe_{1-x}-doped glass

H. Shinojima, J. Yumoto, and N. Uesugi
NTT Basic Research Laboratories, Midori-cho 3-9-11, Musasino-shi, Tokyo 180, Japan

S. Omi and Y. Asahara
HOYA Materials Research Laboratory, Musashiono 3-3-1, Akishima-shi, Tokyo 196, Japan

(Received 3 April 1989; accepted for publication 31 July 1989)

Absorption and photoluminescence peak shifts due to the quantum size effect are observed in CdS_xSe_{1-x} microcrystallites with average radii ranging from several angstroms to 100 Å. For microcrystallite radii between 15 and 100 Å, the observed peak shifts can be described using an effective mass of $0.46m_0$ (m_0 is the free-electron mass), which is 4.6 times as large as the reduced mass in $CdS_{0.12}Se_{0.88}$. When the radius is reduced to less than 15 Å, the effective mass, which is estimated from the experimental results, increases. The discrepancy between the theoretical prediction and the obtained results is discussed.

CdS_xSe_{1-x}-doped glasses have recently attracted much interest for optical communications and optical signal processing because of their large optical nonlinearity and fast response time.[1-3] In addition, the quantum size effect has been studied from the viewpoints of enhancement of optical nonlinearity and the physics of low-dimensional systems.[4,5] In a semiconductor microcrystallite with a radius of over 10 Å, discrete subbands are formed in valence and conduction bands since electron and hole wave functions are confined. The effective band gap between the top of the valence subband and the bottom of the conduction subband is a function of microcrystallite size. For microcrystallites with radii less than the Bohr radius (a_B), Efros and Efros showed that the interband absorption of electrons and holes is theoretically expressed by the reduced mass (μ).[4] It has also been pointed out that the energy of the lowest excited exciton state is dominated by the reduced mass term for a CdS microcrystallite radius between 20 Å and the Bohr radius.[5] These phenomena are observed through peak shifts in absorption and photoluminescence spectra.

Experimental work on the quantum size effect has been reported for a few semiconductor materials, for example, CdS and PbS microcrystallite with a radius of less than a_B. In a CdS microcrystallite radius range between 320 and 12 Å, Ekimov *et al.* reported that the exciton absorption peak is reduced and the interband absorption peak becomes significant as the microcrystallite radius decreases.[6] Wang *et al.* showed that the effective mass approximation breaks down for a PbS microcrystallite radius less than 50 Å. They also provide a cluster model of the band gap, which agrees well with the experimental values.[7] For microcrystallites with a radius less than a_B, however, the confined electron and hole states have not yet been clarified by systematic experiments. This letter reports measurements of peak shifts due to the quantum size effect using the absorption and photoluminescence (PL) spectra for microcrystallites with radii ranging from several angstroms to 100 Å.

Experimental samples have the same composition and the size of CdS_xSe_{1-x} microcrystallites in the glass is controlled by heat treatment.[8] The heat treatment temperature T is varied from 600 to 800 °C, and time t is set to 2, 16, 54, or 128 h.

Semiconductor microcrystallites with radii greater than 10 Å were observed with a transmission electron microscope (TEM), and we obtained the average radii and microcrystallite size distributions within the measurement error of 20%. However, microcrystallites with radii less than 10 Å are outside the TEM resolution. Most microcrystallites were spherical but some had a hexagonal cross section.

Figure 1(a) shows the heat treatment time dependence of the microcrystallite average radius. The horizontal axis is normalized to $(t/2)^{1/3}$. During recondensation, microcrystallite average radius r_{av} in the supersaturated solid

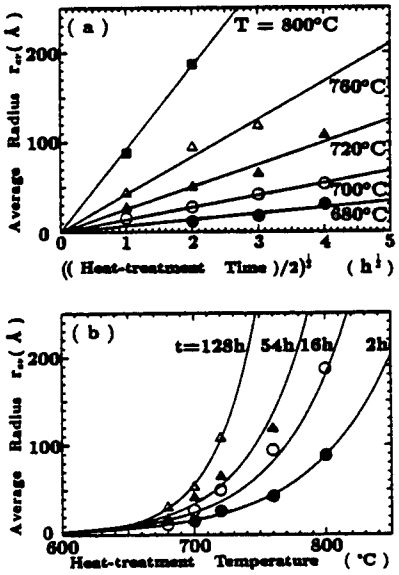

FIG. 1. (a) heat treatment time dependence. Heat treatment time t is set at 2, 16, 54, or 128 h. Temperature T is set at 680, 700, 720, 760, or 800 °C. The solid lines are fitted to the experimental data using the minimum squares method. The measurement error of the average radius is 20%. (b) heat treatment temperature dependence. The solid lines are the calculated curves for each heat treatment time using the equation $r_{av} = r_0(t)\exp[\beta(t)T]$.

 0003-6951/89/411519-03$01.00

solution grows according to the cube-root law, $r_{av} \propto [\alpha(T)D(T)t]^{1/3}$, where $\alpha(T)$ is a coefficient relating to the interfacial surface tension and $D(T) = D_0 \exp(-\Delta E/kT)$ is a diffusion coefficient.[8] Clearly, the experimental results agree very well with the cube-root law. It has been reported that microcrystallites grow in proportion to $t^{1/2}$ just after nucleation.[9] However, Fig. 1(a) suggests that the $t^{1/2}$ growth region is very small and can be ignored. The heat treatment temperature dependence of r_{av} is shown in Fig. 1(b). The experimental results fit the solid lines, assuming r_{av} is expressed by

$$r_{av} = r_0(t)\exp[\beta(t)T] .$$

The average radii of the microcrystallites which could not be observed by TEM are extrapolated using the cube-root law, $r_0(54h) = 4.1\times10^{-6}$ and $\beta(54h) = 0.023$ which reproduce well those of the observed 680 °C microcrystallites.

The absorption spectra measured at room temperature are shown in Fig. 2. The series of subbands due to the quantum confinement effect leads to absorption spectra with some peaks. Peaks A 1 and A 2 are attributed to the transition from the highest valence subband to the lowest conduction subband[4] and from the spin-orbit split-off state in the highest valence subband to the lowest conduction subband, respectively. The energy splittings between A 2 and A 1 for samples with r_{av} of more than 10 Å are about 400 meV, independent of r_{av} in Fig. 4.[10]

The photoluminescence spectra are measured at room temperature using a 488 nm cw Ar pump laser. The power density of the excitation on the sample is 0.1 W/cm^2 and the sample is 0.3 mm thick. Two peaks, P 1 around a wavelength of 600 nm and P2 around 800 nm, are observed in the PL spectra, as shown in Fig. 3. The measurement resolution of the wavelength is 20 Å. P 1 intensity increases as the microcrystallite radius approaches 5 Å, and decreases when the microcrystallite radius is larger than 5 Å. P2, ranging from 700 to 1000 nm in wavelength, is attributed to carrier recombination via the deep levels due to dangling bonds or surface state on the glass microcrystallite boundary.[10] P2 intensity also decreases monotonically as the microcrystallite grows.

The energy shifts of A 1 and P 1 derived from the experimental results of absorption and PL spectra are shown in

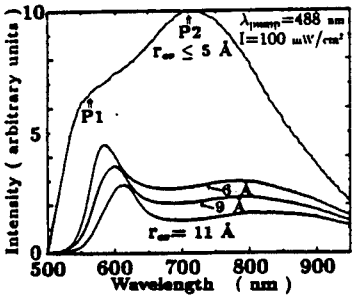

FIG. 3. Photoluminescence spectra. Peak P 1 translates to the lower energy side as particle size increases. P2 is the luminescence from the trap levels due to the surface state. Average radii of less than 10 Å are extrapolated by the cube-root law, $r_0(54h) = 4.1\times10^{-6}$, and $\beta(54h) = 0.023$.

Fig. 4 as a function of microcrystallite radius. Here, the solid line is fitted to the experimental results of the effective radii greater than 15 Å. We also define the effective radius (r_{eff}) as $r_{eff} = (\langle 1/r^2\rangle)^{-1/2}$. Thus, r_{eff} is about 0.9 times r_{av} for our samples.

The transition energy between the highest valence band and the lowest conduction band is described by Eq. (9) in Ref. 4. Taking into account the microcrystallite size distributions, the average of effective band gap, $\langle E_{eff}\rangle$, is given by

$$\langle E_{eff}\rangle = \langle E_g\rangle + \left(\frac{\hbar^2\pi^2}{2\mu}\right)\left\langle\frac{1}{r^2}\right\rangle = \langle E_g\rangle + \left(\frac{\hbar^2\pi^2}{2\mu}\right)\left(\frac{1}{r_{eff}^2}\right),$$

where $\langle E_g\rangle$ is the bulk band gap which is averaged through the stoichiometry distribution of the microcrystals, and $\langle 1/r^2\rangle$ is the average of $1/r^2$ for each microcrystallite. To obtain $\langle E_g\rangle$ for each sample, the stoichiometry x was measured by the ratio of CdS to CdSe longitudinal optical phonon peak in the Raman scattering experiment.[11] Observed x was 0.12 ± 0.05. Ignoring the deviation of x for each sample, the results give $\langle E_g\rangle$, μ, and the total mass as 1.84 eV, $0.1m_0$, and $0.59m_0$, respectively, where m_0 is the free-electron mass. The dotted line in Fig. 4 is the calculated curve using $0.1m_0$.

The absorption peak shift is proportional to r_{eff}^{-2} and is almost zero for the microcrystallite with $r_{eff}>60$ Å as is

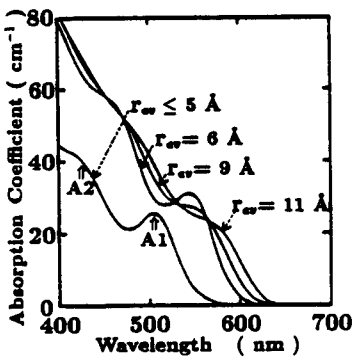

FIG. 2. Absorption spectra. Average radii of less than 10 Å are extrapolated by the cube-root law, $r_0(54h) = 4.1\times10^{-6}$, and $\beta(54h) = 0.023$.

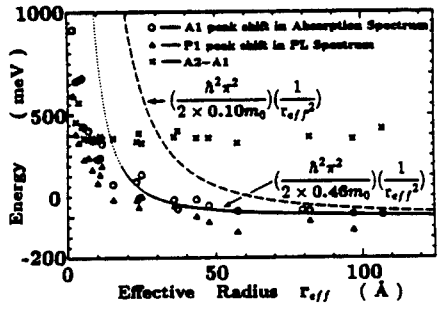

FIG. 4. Size dependence of the absorption and PL peak shift from the bulk band gap. The solid line is fitted to the experimental data of the effective radii greater than 15 Å. The dashed line is the calculated curve using the $CdS_{0.12}Se_{0.88}$ reduced mass. × is the energy splitting between peaks A 2 and peak A 1. The measurement error of the effective radius is 20%.

shown in Fig. 4. Applying the effective mass approximation to the obtained absorption peak shift ($r_{eff}^{-2} \gtrsim 15$ Å), the effective mass is estimated to be $0.46m_0$ which is 4.6 times as large as the $CdS_{0.12}Se_{0.88}$ reduced mass. For r_{eff} less than 15 Å, the peak shift values are confirmed to be far less than those calculated under the effective mass approximation using $0.46m_0$.

Comparing the absorption peak and the PL peak, the energy of peak $P1$ is smaller than that of $A1$ by 80 meV for an effective radius larger than 60 Å. However, the difference between them increases to 300 meV for a radius of several angstroms. It is considered that $P1$ corresponds not to the interband recombination[12] but to carrier recombination via other levels such as donor or acceptor levels.

In current theory, absorption peak shift due to the quantum size effect is calculated using the reduced mass of $0.1m_0$ under the effective mass approximation when the microcrystallite radius is less than a_B. The experimental result for $\langle E_{eff} \rangle$ of more than 15 Å, however, gives the reduced mass as $0.46m_0$. The absorption peak at 2.3 eV observed in 45-Å-diam CdSe microcrystallite[13] leads to the effective mass of $0.16m_0$, which is 1.6 times as large as bulk CdSe reduced mass. This increase in the reduced mass agrees with our result and the difference in the effective mass value between them is considered to be derived from the host material.

The reasons for the discrepancy between the theory and the experimental results have not yet been completely clarified; however, we believe them to be as follows. First, a CdS_xSe_{1-x} microcrystallite is surrounded by many CdS_xSe_{1-x} "clusters" and the wave function penetrates into surrounding clusters. This means that the effective radius of microcrystallite is larger than the actual radius. Second, the effective mass approximation using the invariable effective mass breaks down. This suggests that m_e and m_h for bulk crystal are invalid for microcrystallites with radii between several angstroms and a few hundred angstroms.

In conclusion, the peak shifts in the absorption and PL spectra change in proportion to r_{eff}^{-2} for an effective radius greater than 15 Å, and the size dependence of the peak shift is accurately described by an effective mass of $0.46m_0$. The estimated effective mass gets larger as the microcrystallite radius becomes smaller. The effective mass must be increased when the microcrystallite size decreases.

We would like to thank Toshihide Takagahara and Masaharu Mitsunaga for their useful suggestions, and Masaharu Seki for operating the TEM.

[1]R. K. Jain and R. C. Lind, J. Opt. Soc. Amer. 73, 647 (1983).
[2]S. S. Yao, C. Karaguleff, A. Gabel, R. Fortenberry, C. T. Seaton, and G. I. Stegeman, Appl. Phys. Lett. 46, 801 (1985).
[3]M. Mitsunaga, H. Shinojima, and K. Kubodera, J. Opt. Soc. Amer. B 5, 1448 (1987).
[4]Al. L. Efros and A. L. Efros, Fiz. Tekh. Poluprovodn. 16, 1209 (1982) [Sov. Phys. Semicond. 16, 772 (1982)].
[5]L. E. Brus, J. Chem. Phys. 80, 4403 (1984).
[6]A. I. Ekimov, Al. L. Efros, and A. A. Orushchenko, Solid State Commun. 56, 921 (1985).
[7]Y. Wang, A. Suna, W. Mahler, and R. Kasowski, J. Chem. Phys. 87, 7315 (1987).
[8]I. M. Lifshitz and V. V. Slezov, Sov. JETP 35, 331 (1959).
[9]F. C. Frank, Proc. Roy. Soc. London A 201, 586 (1950).
[10]N. Chestnoy, R. Hull, and L. E. Brus, J. Chem. Phys. 85, 2237 (1986).
[11]Z. Fangce, S. Yunfeng, and P. Jinsheng, J. Lumin. 40&41, 739 (1988).
[12]P. Roussignol, D. Ricard, J. Lukasik, and C. Flyzanis, J. Opt. Soc. B 5, 1448 (1988).
[13]A. Alivisatos, A. L. Harris, N. J. Levinos, M. L. Steigerwald, and L. E. Brus, J. Chem. Phys. 89, 4001 (1988).

to be published in Appl. Phys. Lett. vol. 57, Dec. 3 (1990).

Optical nonlinearity of CdSe-microcrystallites in a sputtered SiO_2 film

J. Yumoto, H. Shinojima, N. Uesugi
NTT Basic Research Labs., Musashino, Tokyo 180, Japan

K. Tsunetomo
Department of Electrical Engineering, Faculty of Engineering, Hiroshima Univ., Saijyo, Higashi-Hiroshima, Hiroshima 724, Japan

H. Nasu
Department of Industrial Chemistry, Faculty of Engineering, Mie Univ., Tsu, Kamihama, Mie 514, Japan

and Y. Osaka
Department of Electrical Engineering, Faculty of Engineering, Hiroshima Univ., Saijyo, Higashi-Hiroshima, Hiroshima 724, Japan

ABSTRACT

Optical nonlinearity of a sputtered SiO_2 film containing CdSe-microcrystallites with an average diameter of 15 Å is measured by degenerate four-wave mixing (DFWM) experiments. A effective nonlinear cross section σ_{eff} of 1.4×10^{-16} cm^2 is obtained. The DFWM signal as a function of the probe delay time shows bi-exponential behavior with a fast decay time of 10 psec and a slow decay time of 60 psec, which give fast and slow carrier recombination times as 20 psec and 120 psec. The third-order susceptibility $|\chi^{(3)}|$ is estimated to be 1.3×10^{-8} esu. The photodarkening and the laser annealing effects which are serious problems for device applications are not observed.

[passage omitted in original]

by degenerate four-wave mixing (DFWM) or pump-probe measurements. In addition, the optical nonlinear interactions have also been demonstrated in waveguides,[5,6] making SDG's one of the candidates for nonlinear integrated devices.

The optical nonlinearities of SDG's have some disagreements about the reported values of $\chi^{(3)}$ and relaxation time. Much of this controversy is explained by the photodarkening effect and the laser annealing effect. Roussignol et al. reported on the photodarkening effect,[4] that is, the DFWM signal intensity decreases during laser beam irradiation. Mitsunaga et al.[7] also reported that a DFWM signal consists of a slow decay component and a fast decay component, and that the slow decay component decreases drastically by laser beam exposure. Such phenomena are thought to be attributed to the trap states due to vacancies, dangling bonds and impurities. Microscopic phenomena, however, have not yet been clarified.

In SDG's, CdS_xSe_{1-x} -microcrystallites are embedded in multi-component glasses. Multi-component glasses contain more than 10 wt% of alkaline metals, Na and K which form donor or acceptor levels in II-VI compound microcrystallites. Impurities and vacancies in microcrystallites make the optical properties very complicated. In order to understand the intrinsic properties of semiconductor-microcrystallites, it is preferable to employ a simple system without impurities and vacancies.

In this letter, optical nonlinearities of a sputtered SiO_2 film with CdSe-semiconductor-microcrystallites (SSM) are reported for the first time. Compared with SDG's, SSM contains a small number of impurities in the host SiO_2 and the optical properties of the microcrystallites with a small number of impurities can be observed. Note that in DFWM experiments, the SSM does not show the photodarkening and the laser annealing effects for the input energy of less than 80 $\mu J/cm^2$.

Sample were prepared by a conventional magnetron rf-sputtering equipment. A SiO_2 glass plate with a diameter of 4 inches was used as the target, on which a number of CdSe polycrystalline chips were placed.[8] Sputtering was carried out for 180 min in an ultrahigh pure Ar gas atmosphere of 5×10^{-3} Torr. A SiO_2 film with a thickness of 10 μm was sputtered on a SiO_2 substrate. X-ray photoelectron spectroscopy (XPS) revealed a CdSe concentration of 1 atomic % and the average microcrystallite size was observed to be about 15 Å in diameter by an x-ray diffraction measurement.

Figure 1 shows the absorption spectrum of an SSM at room temperature. An absorption peak corresponding to the transition from the highest valence subband to the lowest conduction subband appears at around 2.1 eV ($\sim$ 600 nm). The width of this peak is broader than that of an SDG with the same average microcrystallite size.[9] The broad absorption peak is thought to be attributed to the wide distribution of microcrystallite sizes in the SSM.

Optical nonlinearity of the SSM is measured by a DFWM experiment in a folded boxcar configuration.[7] The light source is a synchronously-pumped mode-locked dye laser with a cavity dumper. The pump source is a second-harmonic-generated beam of a mode-locked Nd:YAG laser with a wavelength of 532 nm. Pulse width and repetition rate of the dye laser are 0.7 psec and 4MHz, respectively. The laser oscillating wavelength is 600 nm (2.1 eV). Absorption of the sample at the wavelength of 600 nm is 1270 cm^{-1} ($\alpha l = 1.27$). The phase matched diffracted beam of the probe pulse was detected by a photomultiplier using a cross modulation technique for lock-in detection in order to improve the signal-to-noise (S/N) ratio.

In DFWM experiments using a mode-locked laser with a pulse width much less than a longitudinal decay time of a sample, the diffraction efficiency ρ_s in small signal limit is given

by[10]

$$\rho_s \simeq (\sigma_{eff} N l)^2 \exp(-\alpha l), \tag{1}$$

where N is the carriers density generated by one pump pulse, l is the sample length, and α is the absorption coefficient. The effective nonlinear cross section σ_{eff} is defined by

$$\sigma_{eff} = \frac{1}{2}\sqrt{(\frac{2\pi}{\lambda} n_{eh})^2 + (\frac{\sigma_{eh}}{2})^2},$$

where n_{eh} and σ_{eh} are the change of the refractive index and absorption coefficient per electron-hole pair per unit volume. The dependence of ρ_s on the input pump pulse energy at probe delay $\tau_d = 0$ is shown in Fig. 2. The signal is described by the third-power of the input pulse energy as expected for the third-order optical nonlinearity, and saturation of the diffraction efficiency is not observed. A diffraction efficiency of 0.8×10^{-4} was obtained at an input pump energy of 60 μJ/cm^2. For these experimental results, σ_{eff} is estimated to be 1.4×10^{-16} cm^2.

The DFWM signal as a function of the probe delay time τ_d is shown in Fig. 3. Because the polarization of the three beams are parallel, a coherent spike can been seen at delay time $\tau_d = 0$. The DFWM signal as a function of τ_d shows a bi-exponential behavior with a fast decay component and a slow decay component. The fast and slow decay times, τ_f and τ_s are 10 psec and 60 psec, and the strength of the fast decay component is 1.4 times larger than that of the slow decay component. A DFWM signal intensity is proportional to N^2 as described by Eq. (1). Therefore, fast and slow carrier recombination times τ_{cf} and τ_{cs} are obtained as 20 psec and 120 psec, respectively. The σ_{eff}, τ_{cf} and τ_{cs} give the $|\chi^{(3)}|$ of SSM for quasi-monochromatic, cw excitation.[10] It is calculated to be 1.3×10^{-8} esu.

We compared the optical nonlinearity of the SSM with that of a commercial glass filter HOYA R64. The σ_{eff} of R64 after the laser annealing effect was 1.5 $\times10^{-16}$ cm^2, which is almost the same as that of SSM. A $|\chi^{(3)}|$ of 0.9×10^{-10} esu is also estimated for a carrier recombination time of 7 psec.[7] The large $|\chi^{(3)}|$ of SSM can be attributed to the high concentration of microcrystallites in the host glass. Such a high concentration of microcrystallites in SDG's can not be obtained by a precipitation technique because of phase separation in the host glass.

In SDG's, the decay curves as a function of τ_d also show bi-exponential behavior. The photodarkening and laser annealing effects are always observed in SDG's for the same input energy. Here, we should point out that the photodarkening and laser annealing effects were not observed, and the intensity and the decay time of the DFWM signal did not change after a few-hour laser irradiation.

Time-resolved PL spectra were analyzed using a synchronously-scanning streak camera in order to obtain information about the origin of the photodarkening and the laser annealing effects. The light source was a second-harmonic-generated (SHG) light (532nm) with a pulse width of 70 psec (FWHM) pumped by a mode-locked YAG laser. The streak camera was locked to 82-MHz laser pulse train and the time resolution of our system is about 20 psec. Figure 4 shows a time-resolved PL spectrum of SSM at 77 K. The time-resolved PL spectrum of the SSM consists of only the emission around the bandgap with a fast decay of less than 100 psec. The time-resolved PL of SDG shows an emission around the bandgap and an emission at the low-energy side of the bandgap.[11] The decay time of both emissions are a few-hundred psec and on the order of μsec, respectively. The low-energy-side emission with a long decay time is thought to be attributed to trapped states due to vacancies, dangling bonds, or impurities. A comparative study of the time-resolved PL spectra of SSM and

100 psec. The time-resolved PL of SDG shows an emission around the bandgap and an emission at the low-energy side of the bandgap.[11] The decay time of both emissions are a few-hundred psec and on the order of μsec, respectively. The low-energy-side emission with a long decay time is thought to be attributed to trapped states due to vacancies, dangling bonds, or impurities. A comparative study of the time-resolved PL spectra of SSM and SDG suggests that the low-energy-side emission with a long decay time in SDG's is due to alkaline metal impurities, and that the photodarkening and laser annealing effects are related to these impurity levels.

In conclusion, optical nonlinearities of the SiO_2 film containing CdSe microcrystallites with an average diameter of 15 Å were measured by DFWM experiments using a mode-locked laser system. The effective nonlinear cross section σ_{eff} was estimated to be 1.4×10^{-16} cm^2 which is almost the same as that of SDG. The DFWM signal as a function of the probe beam delay time shows bi-exponential behavior with a fast decay time of 10 psec and a slow decay time of 60 psec, which give fast and slow carrier recombination times as 20 psec and 120 psec, respectively. The $|\chi^{(3)}|$ was calculated to be 1.3×10^{-8} esu which is more than one order of magnitude larger than that of a SDG. The large $\chi^{(3)}$ is attributed to the high concentration of CdSe-microcrystallites in the SiO_2 film. We should also point out that the photodarkening effect and the laser annealing effect can not been observed. These properties are considered superior for not only device applications but also the characterization of microcrystallites.

References

[1]R. K. Jain and R. C. Lind, J. Opt. Soc. Am.,73, 647 (1983).

[2]S. Schmitt-Rink, D. A. B. Miller and D. S. Chemla, Phy. Rev. B, 35, 8113 (1987): T. Takagawara, Phys. Rev. B, 36, 9293 (1987).

[3]G. R. Olbright, N. Peyghambarian, S. W. Koch and L. Banyai, Opt. Lett., 12, 413 (1987).

[4]P. Roussignol, D. Ricard, J. Lukasik and C. Flytzanis, J. Opt. Soc. Am. B, 4, 5 (1987).

[5]A. Gabel, K. W. DeLong, C. T. Seaton and G. I. Stegeman, Appl. Phy. Lett. 51, 1682 (1987).

[6]H. Jerominek, S. Patela, M. Pigeon, Z. Jakubczyk, C. Delisle and R. Tremblay, J. Opt. Soc. Am. B, 5, 496 (1988).

[7]M. Mitsunaga, H. Shinojima and K. Kubodera, J. Opt. Soc. Am. B 5, 1448 (1988).

[8]H. Nasu, K.Tsunetomo, Y. Tokumitsu and Y. Osaka, Jpn J. Appl. Phys. 28, L862 (1989).

[9]H. Shinojima, J. Yumoto, N. Uesugi, S. Omi and Y. Asahara, Appl. Phy. Lett., 55, 1519 (1989).

[10]M. N. Islam, E. P. Ippen, E. G. Burkhardt, and T. J. Bridges, J. Appl. Phys. 59, 2619 (1986).

[11]M. Tomita and M. Matsuoka, J. Opt. Soc. Am. B, 6, 165 (1989).

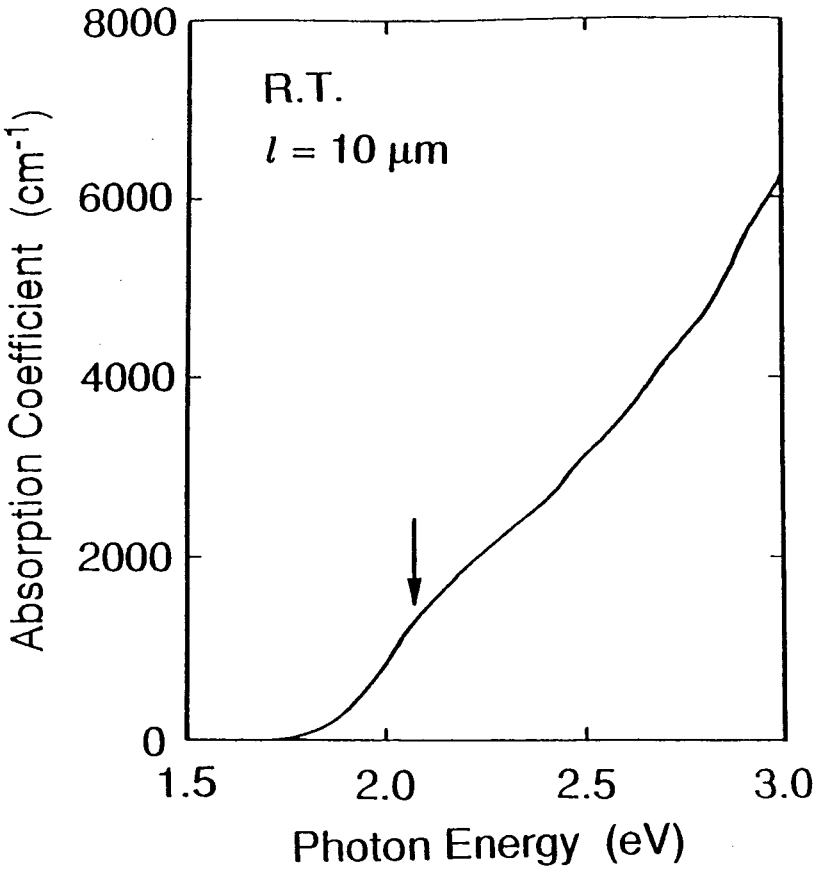

Fig. 1 Absorption spectrum of an SiO_2 file containing CdSe-microcrystallites. The arrow indicates the laser beam energy in the DFWM experiments.

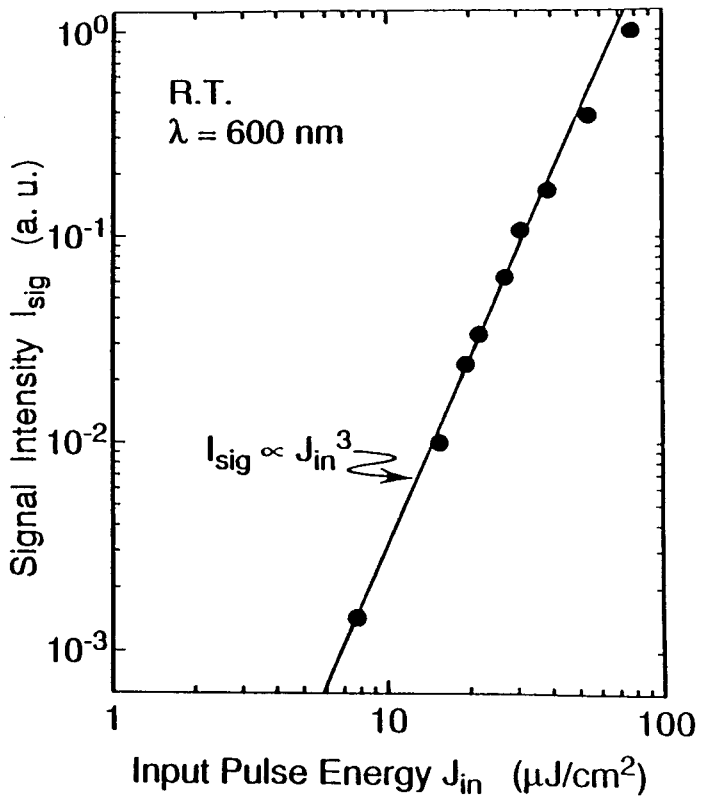

Fig. 2 Dependence of the DFWM signal on the input pulse energy.

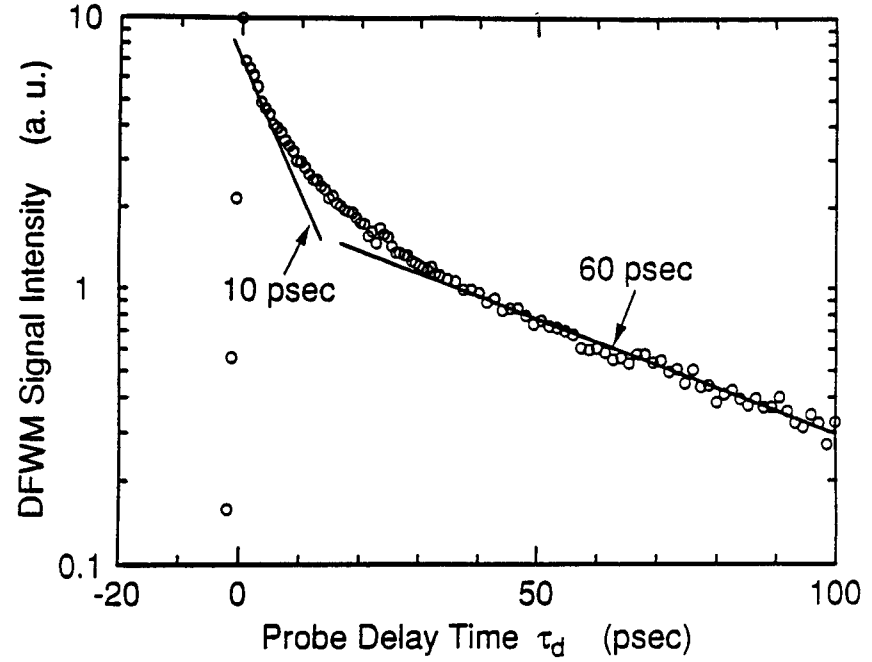

Fig. 3 The DFWM signal as a function of the probe delay time. The decay curve consists of a 10 psec-decay component and a 60 psec-decay component. These decay times give fast and slow carrier recombination times as 20 psec and 120 psec, respectively.

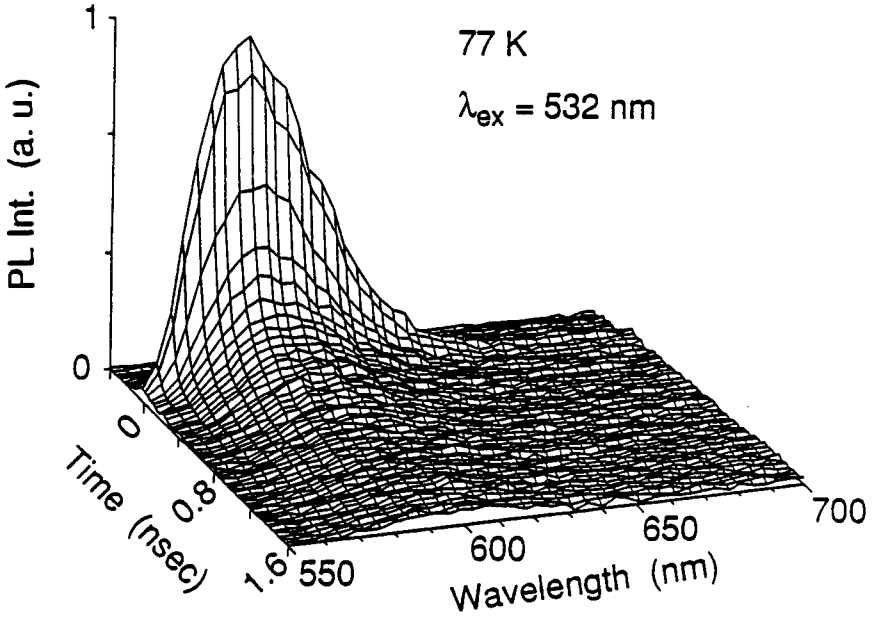

Fig. 4 Time-resolved photoluminescence spectrum of the SSM.

SESSION III

(1)

Glass-Based Composites for Biomedical Applications

Tadashi Kokubo
Institute for Chemical Research
Kyoto University

A heat treatment of a $MgO-CaO-SiO_2-P_2O_5$ glass gave a glass-ceramic containing crystalline apatite ($Ca_{10}(PO_4)_6(O,F_2)$) and β-wollastonite ($CaO \cdot SiO_2$) in a $MgO-CaO-SiO_2$ glassy matrix. It showed not only a bioactivity but also a fairly high mechanical strength which is only slowly decreased even under load-bearing conditions in the body. It is being clinically used as artificial vertebrae, iliac bones etc. The bioactivity of this glass-ceramic was attributed to apatite formation on its surface in the body. Dissolution of calcium and silicate ions from the glass-ceramic was considered to play an important role in forming the surface apatite layer. On the basis of this finding, it was shown that some new kinds of bioactive materials can be developed from CaO,SiO_2-based glasses. Ceramics, metals and organic polymers coated with bone-like apatite were obtained, when they were placed in the vicinity of a CaO,SiO_2-based glass in a simulated body fluid. A bioactive bone-cement which was hardened by 4 minutes and bonded to living bone forming an apatite was obtained by mixing a CaO,SiO_2-based glass powder with a neutral ammonium phosphate solution. Its compressive strength reached 80 MPa comparable to that of PMMA by 3 days. A bioactive and ferromagnetic glass-ceramic containing crystalline magnetite (Fe_3O_4) in a matrix of CaO,SiO_2-based glassy and crystalline phases was obtained by a heat treatment of a $Fe_2O_3-CaO \cdot SiO_2-B_2O_3-P_2O_5$ glass. This glass-ceramic was shown to be useful as thermoseeds for hyperthermia of cancer.

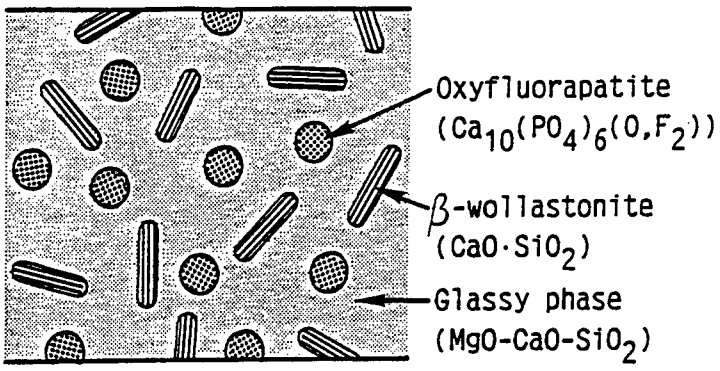

Microstructure of glass-ceramic A-W.

Specimen	Phase	Bending strength(σ)	Fracture toughnes(K_{1C})
G	g(100)	70 MPa	0.8 $MPa \cdot m^{1/2}$
A	a(38) g(62)	90	1.2
A-W	a(38) w(34) g(28)	200	2.0
HAp		115	1.0
Human bone		160	2 ~ 6

a: Oxyfluoroapatite, w: β-wollastonite, g: glassy phase
HAp: Sintered dense hydroxyapatite

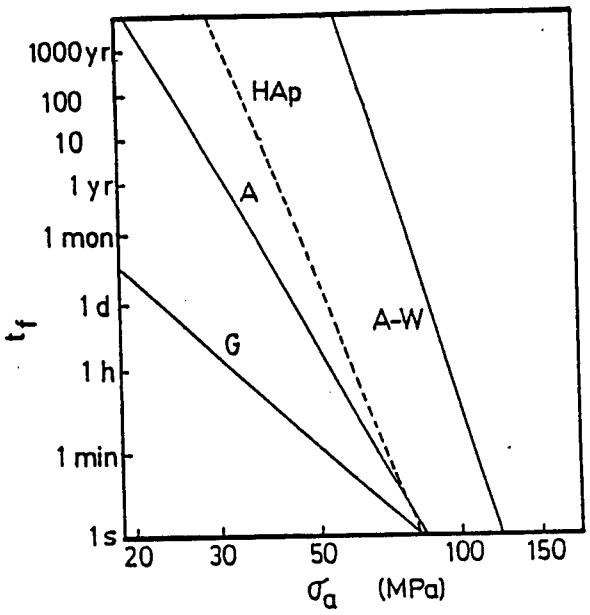

Estimated life time t_f as a function of applied stress σ_a

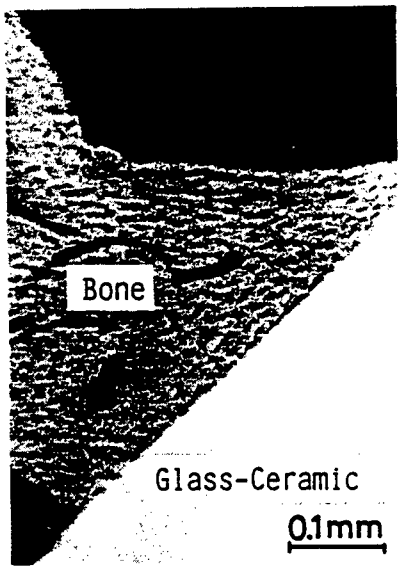

CMR of glass-ceramic A-W implanted into tibia of rabbit, 8 weeks after implantation.

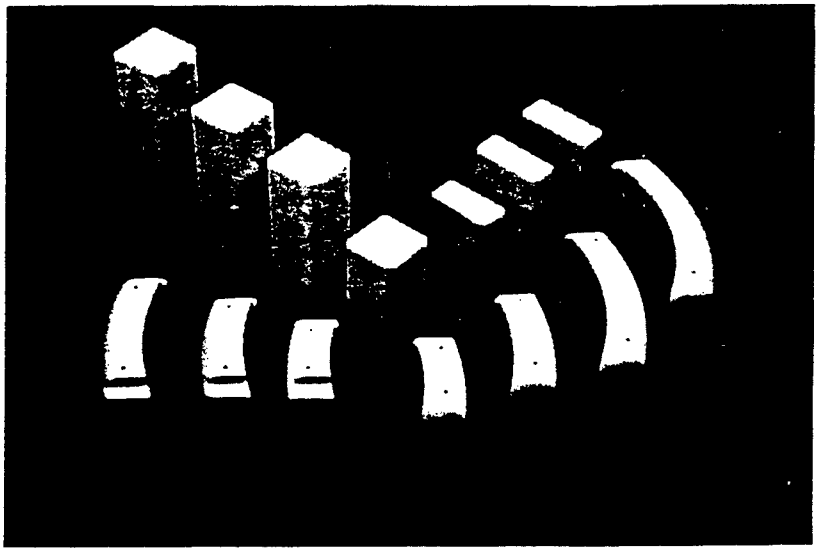

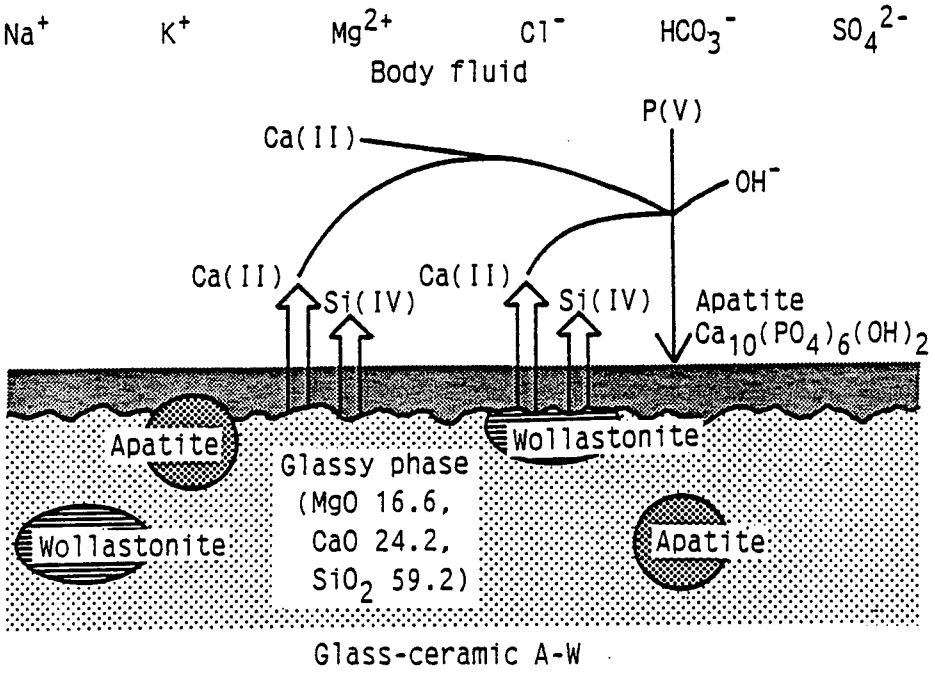

Schematic representation of apatite formation on glass-ceramic A-W.

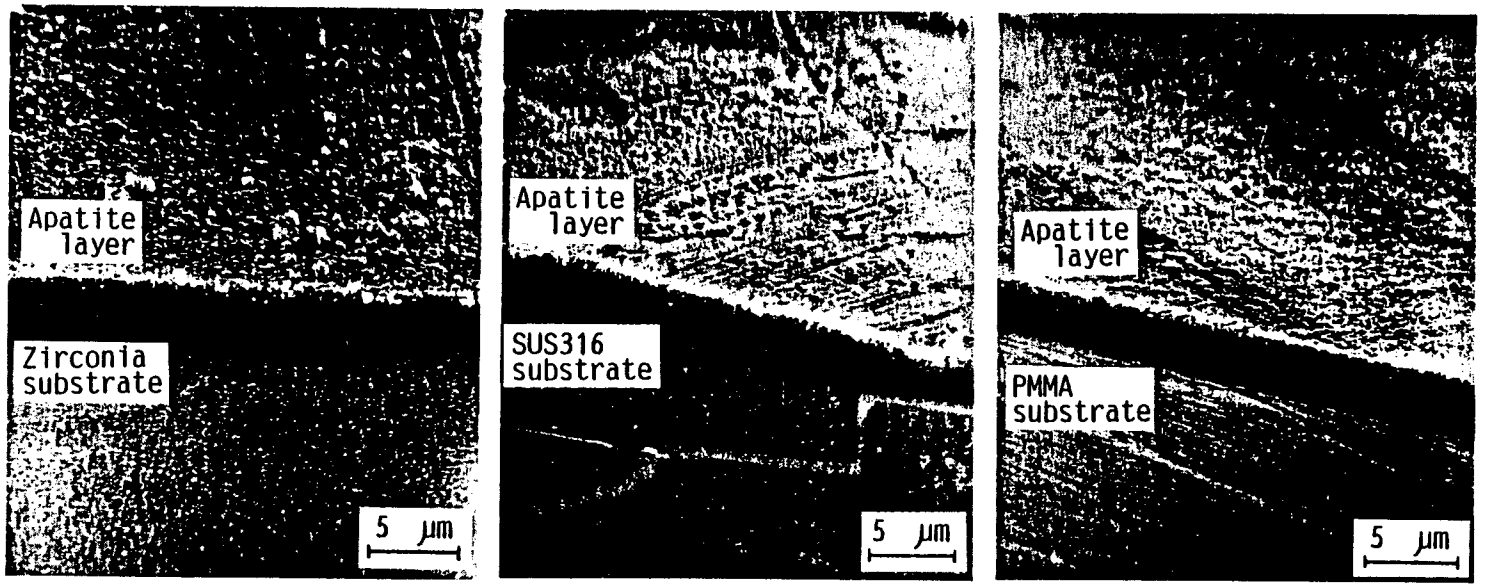

SEM pictures of apatite layers formed on zirconia ceramic, SUS316 stainless steel, and polymethylmethacrylate substrates.

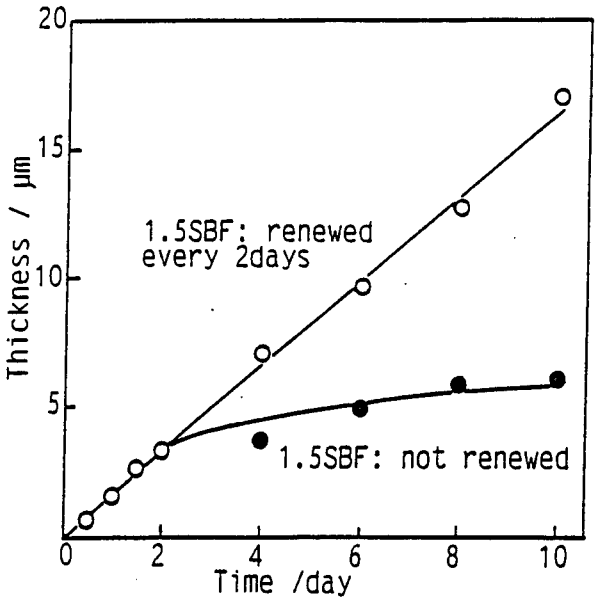

Thickness of the apatite layer formed on alumina substrates as a function of soaking time in 1.5SBF after soaking in SBF with glass G for 2d.

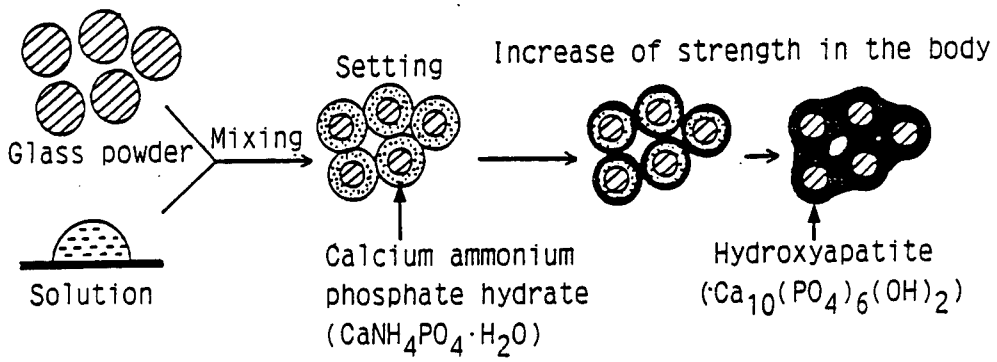

Hardening mechanism of bioactive bone cement.

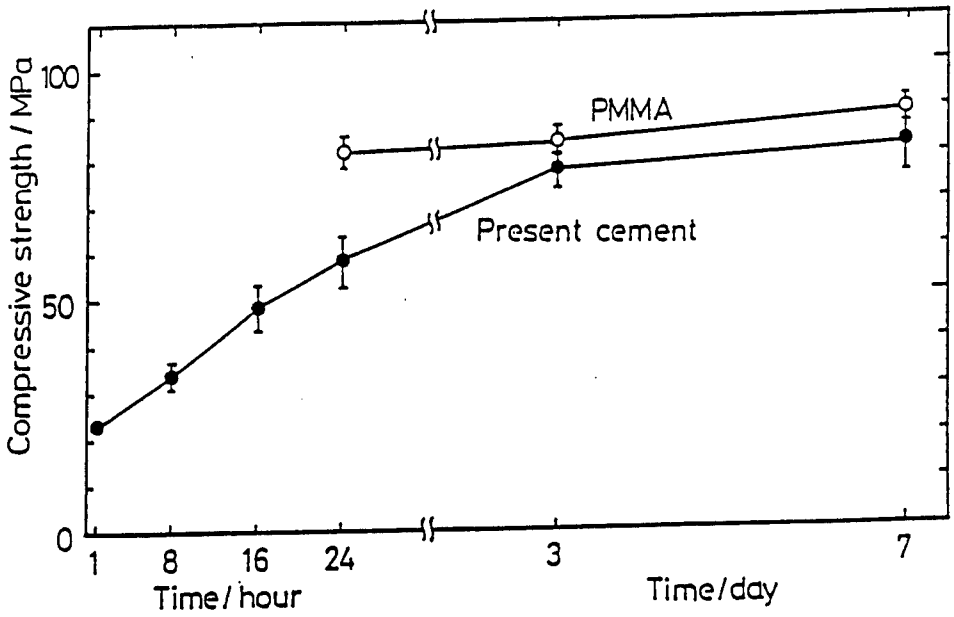

Compressive strength (in wet) of solidified cement as a function of time in comparison with that of PMMA.

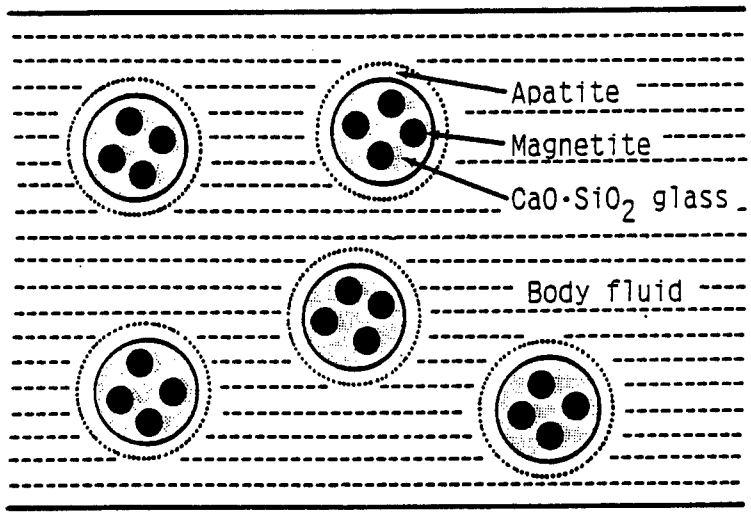

Bioactive and ferromagnetic glass-ceramics.

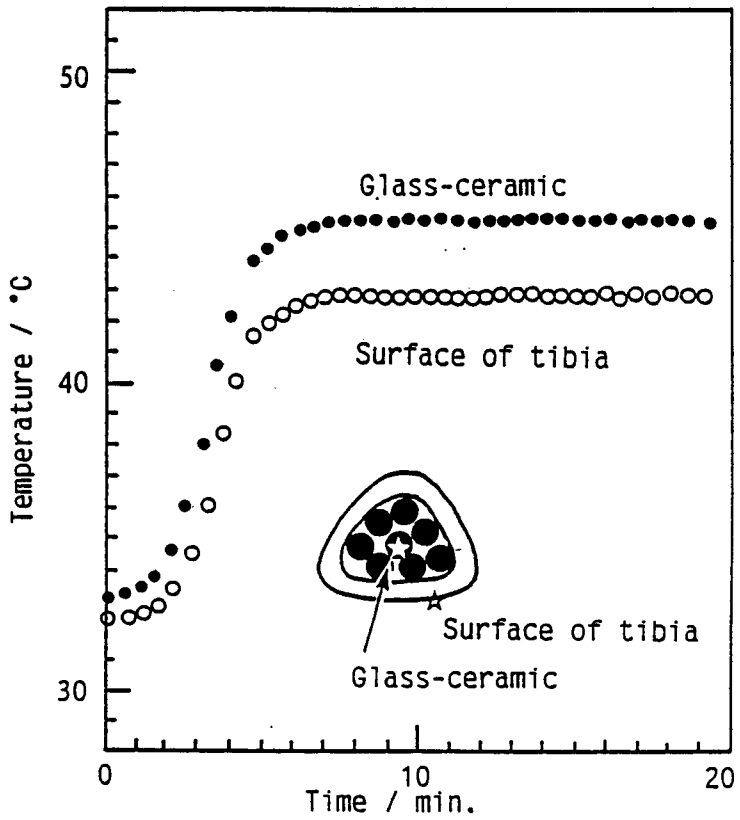

Change of temperature of glass-ceramic and rabbit tibia with application of alternating magnetic field of 100 kHz, up to 300 Oe.

Overview of Fiber Reinforced Glass and Glass-Ceramic Matrix Composites

(International Meeting on New Glass Technology - N.G.F. '90)
(December 10-11, 1990, Tokyo, JAPAN)

Otis Y. Chen
RCAST, the University of Tokyo
(On leave from Pratt & Whitney)

Karl M. Prewo
United Technologies Research Center

During the last few decades, materials scientists have been able to make revolutionary changes in the way that the materials are being used. The concept of producing composites materials from homogeneous and isotropic constituents has opened major new avenues to achieving advanced engineering systems never previously possible. From sporting goods to industrial and aerospace applications, the availability of these materials has freed the designer from the constraints of conventional material technology and permitted the development of higher performance systems. One of the examples of a drastic change of the materials properties with the incorporation of second phase constituents is a carbon reinforced cement. With a mere 2% addition of chopped carbon fiber to a brittle cement, a drastic improvement of the toughness as well as the load carrying capability can be obtained, as shown in Figure 1.

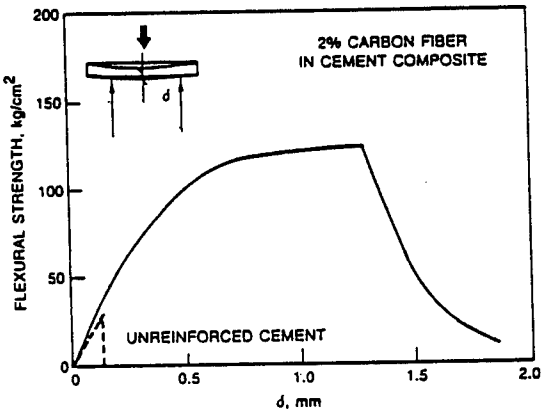

Figure 1 Comparison of Bend Tests for Unreinforced Cement and Cement Matrix Composites Containing 2% of Chopped Carbon Fiber.

As the need for advanced materials with a diverse range of applications from biomedical and automobile to aerospace increases, many scientists conclude that crystalline ceramics and oxide glasses and glass ceramics offer many advantages over metal alloys for their high strength and stability at elevated temperatures. Again, when the use of the these materials in a structural application is severely limited by their extreme sensitivity to flaws and brittle characteristics, it is natural for the scientists to consider the possibility of incorporating second phase reinforcement for greater reliability.

In this paper, the development of fiber reinforced glasses and glass ceramics will be reviewed. The current status of these materials will be described and important aspects of their development traced.

Glass and Glass-ceramic matrix Composite Processing

From a composite fabrication point of view, glass matrix composites, as compared to the other brittle ceramic candidates, probably offer the greatest commercial potential from an ease of densification, low cost and also achievement of high performance aspects. The following attributes are important in this sense.

- o Glasses can be created with a broad range of chemistries to control fiber-matrix chemical interaction.
- o Glasses can be created with a wide range of thermal expansion coefficients to tailor them to nearly match those of reinforcing fibers.
- o The low elastic modulus of glasses (50-90 GPa) permits high modulus fibers to provide true reinforcement.
- o The ability to control the viscosity of glasses and to flow them easily under pressure permits the physical densification of fiber reinforced composites without mechanical damage to the fibers. It will be shown that relatively high fiber contents can be achieved by several techniques.
- o The composite densification process can be rapid since glass matrix flow is all that is required.

Because of the fact that glass can be treated as a thermoplastic material, many of the processes developed for fiber reinforced glasses can be made to emulate those previously used for polymer matrix systems. Sambell, Phillips and Bowen[1] described in detail the development of a procedure for the fabrication of carbon fiber reinforced glasses using a process closely resembling that for polymer matrix systems. Collimated fibers were wound on mandrels after having been infiltrated with a slurry of glass powder. The resultant tapes could then be cut into plys and densified under pressure and high temperature to achieve nearly full density microstructures. The processes of fabricating glass matrix composites are shown in Figure 2.

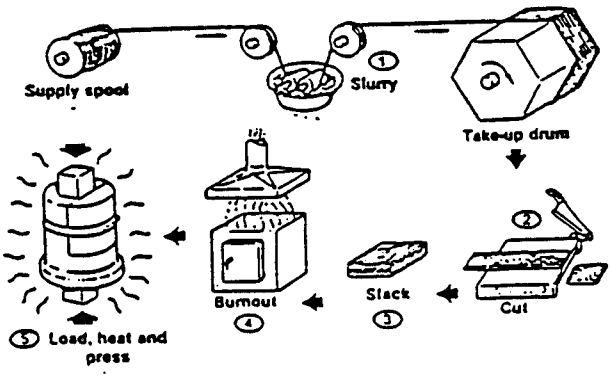

Figure 2 Processing Flow Chart of Glass Matrix Composites Fabrication

Other approaches such as co-winding of fiber and matrix (in a fiber form), the use of a liquid hydrolyzable metalalkoxide to infiltrate precursor fiber tows, and matrix transfer molding have all been successfully demonstrated.

While the above processes were originally demonstrated with glasses, they can also be readily practiced using glass ceramics. The key here is that composite densification takes place while the matrix is in the substantially glassy and viscous form. After full densification the glass can be crystallized under controlled heat treatment conditions to achieve a matrix with superior toughness and high temperature strength.

Composites Properties

Composite properties differ greatly depending on the matrix/fiber combinations. The properties of the following major systems will be described in detail.

Carbon Fiber Reinforced Glass Matrix Composites

Carbon fibers offer the highest structural performance potential of any of the reinforcements. Available in a wide variety of elastic moduli and at relatively low cost, they offer the opportunity to create economically viable systems right now. The ability to fabricate a broad range of carbon fiber reinforced glasses and glass ceramics has been demonstrated by several investigators and resultant composite mechanical properties have been characterized for numerous types of test conditions[2-7]. Through the use of very high elastic modulus pitch based carbon fibers, composites with exceptionally high elastic moduli were obtained[5,7], as shown in Figure 3.

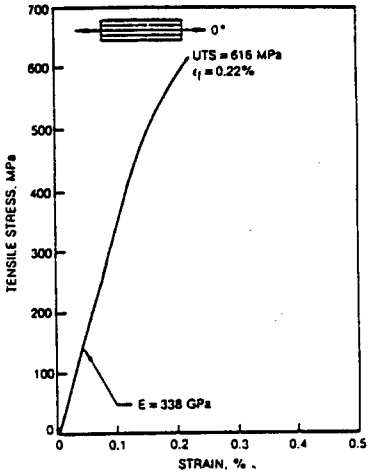

Figure 3 Tensile Stress-Strain Curve for P-100 Carbon reinforced Borosilicate Glass Matrix Composites.

While most of the emphasis over the years has been on the development of carbon reinforced glass for structural applications, it should be noted that the system can also be extremely useful for other reasons. As in the case of carbon reinforced glass, the carbon fibers impart lubricity to the composite surface and the glass matrix can impart higher hardness and wear resistance[8,9]. The combination of glass and carbon fibers also results in a material with exceptional dimensional stability equivalent or superior to even the most dimensionally stable glasses[5,6,6,10,11].

Oxide Fiber Reinforced Composites

Both Al_2O_3 and SiO_2 type fibers have been used to reinforce glasses in the hope of achieving systems with excellent high temperature oxidative stability. Several different types of alumina fibers were used to reinforce high silica glass matrices with the result that modest levels of strength were achieved[12], as shown in Figure 4 and these levels could be maintained up to 1000C. Through qualitative observations of composite fracture surfaces, however, it was found that composites were relatively brittle and this behavior was associated with the formation of a much stronger fiber-matrix bond in these systems.

Fracture surfaces exhibited only very short lengths of fiber pull out and cracks propagate through these composites much more readily. To achieve much higher levels of performance, it was shown that an interfacial region could be artificially created between fiber and matrix[13]. Through the use of an aluminum metal coating on 100μ diameter SiO_2 fibers, it was possible to incorporate them in a low temperature glass matrix and achieve a notch insensitive impact resistant material (Figure 5).

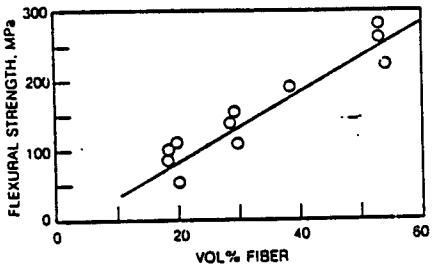

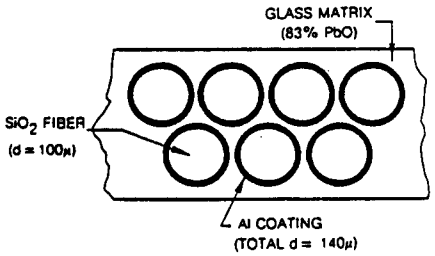

Figure 4 Unidirectional Strength of SiO_2 Matrix Composites vs. Al_2O_3 Content

Figure 5 Metal Coated Fibers Used for Improved Impact Resistance Inorganic Composites

Silicon Carbide and Boron Large Diameter Fiber Reinforced Composites

The availability of high strength fibers of boron and silicon carbide produced by chemical vapor deposition has also been activity pursued as an approach to achieving high performance composites. These filaments have been available for nearly as long as carbon fibers but because of their greater cost and their somewhat less convenient and less flexible composite fabrication possibilities they have not received quite as much attention. Boron fiber reinforced glass was shown to provide composites of exceptionally high strength, stiffness and toughness. Borosilicate glass reinforced with 30% by volume boron fibers exhibited room temperature flexural strengths of 1120 MPa.

Using large diameter SiC fibers that were deposited on a carbon core with a carbon rich surface, borosilicate glass matrix composite were fabricated with high strength and toughness[14].

Silicon Carbide Yarn Reinforced Composites

A major increase of interest in the development of fiber reinforced glass and glass-ceramic can be attributed to the development of a high performance silicon carbide type yarn by Professor Yajima and his co-workers[15]. Available under the name NICALON® with an average tensile strength and elastic modulus of 2060 MPa and 193 GPa, respectively, suited to the development of high strength glass and glass ceramic matrix composites[14,16,17,18]. To achieve the highest levels of strength and temperature capability, the use of lithia aluminosilicate (LAS) matrices proved most advantageous. By densifying the composites while the matrix is in a glassy state and then crystallizing (ceraming) the matrix afterwards it was possible to fabricate easily yet end up with a very refractory composite. The impressive toughness has been related to the presence of a low strength carbon rich fiber-matrix interfacial region created during composite fabrication and attributable to fiber and matrix chemistry[18].

Further testing of these composites in tension has shown that their strength can, in part, be related to the in-situ NICALON® fiber tensile strength, and that, when fiber strength and failure strain are great enough to permit matrix failure to occur without overloading the fibers, a nonlinear tensile stress-strain curve was observed as shown in Figure 6. Also shown in this figure is the tensile stress-strain curve for a NICALON® reinforced epoxy matrix composite which is perfectly linear to failure due to the fact that the epoxy matrix has a higher failure strain than the NICALON® fibers. Repeated mechanical tensile cycling of the LAS matrix composite at increasing values of strain results in the observation that composite elastic modulus decreases markedly with increasing strain (Figure 7). This is attributed to the progressive microcracking of the matrix and accompanying decrease in its contribution to the composite stiffness. Eventually the final composite elastic modulus of 88 MPa can be attributed almost solely to the reinforcing fibers.

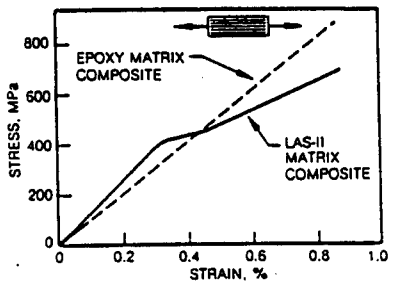

Figure 6 Tensile Stress Strain Curve for Unidirectional SiC Composites.

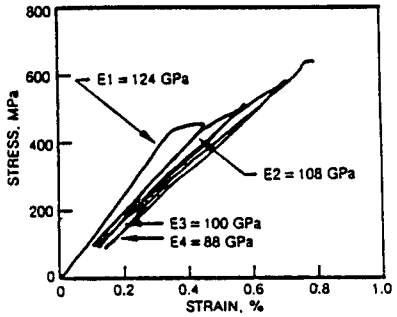

Figure 7 Cycled Tensile Stress-Strain curves for SiC Reinforced LASII Composites.

Fracture Mechanism

A structural glass and glass-ceramic matrix composite can be readily classified as a "toughened" glass. The fibrous addition increases the toughness through crack deflection and fiber bridging behind the crack tip. The blunting of the crack tip and the changing of the crack path can be achieved through the presence of interfaces with the addition of fiber and it is essential to have a low interfacial shear strength. The ability to contain matrix microcracking within the composite without causing immediate failure results in high failure strain composites with highly non-linear stress-strain curves despite the very limited strain capability of both matrix and fiber. A non-linear stress-strain behavior leads to the ability of these materials to redistribute applied loads in a manner similar to metals and hence achieve greater reliability.

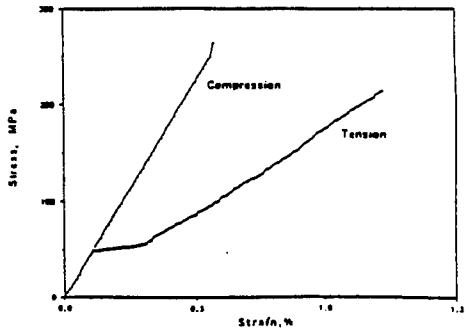

Figure 8 Stress-Strain Curves of Tension and Compression for chopped Graphite Fiber Reinforced Glass Composites

A typical stress-strain curve characteristics of a discontinuous graphite fiber reinforced glass matrix composite under both tension and compression[19] is shown in Figure 8. The initial linear part of the curve for tensile and compression testing is identical. However, the composite exhibited linearity under compressive loading all the way to failure. The tensile curve showed a plateau or a pseudo "yielding" behavior due to matrix cracking, followed by fracture. The fracture of tensile specimens occurred in a non-catastrophic manner with extensive fiber pull-out.

Further understanding of the fracture mechanism can be obtained using the acoustic emission technique to track damage progression in real time[20-22]. The AE results for the above discontinuous fiber reinforced glass matrix composites during loading are shown in Figure 9. The AE data are divided into three regions; (a), (b), and (c). The region (a) corresponds to the initial portion of the stress-strain curve in which the material first behaves elastically and then shows non-linearity induced by matrix microcracking. The region (b) corresponds to the intermediate region in which the stress-strain curve is linear but has a reduced modulus. The region (c) corresponds to the last portion of the stress-strain curve which includes the final failure. In region (a), considerable acoustic emission activity occurs and most of the events have an amplitude ranging between 45 and 60 dB. In region (b), very little acoustic emission activity is noted. This suggests that no further fracture events occur in this region. This fact is supported by the linear stress-strain curve in this region. Considerable activity is again noted in region (c). The amplitude of these AE events ranges between 60 and 70 dB. This suggests that the AE events occurring in this region are different from those occurring in region (a). The AE activity in this region probably corresponds to fiber breakage. These observations indicate that microcraking is confined to region (a), and mostly to the horizontal or plateau portion in the stress-strain curve.

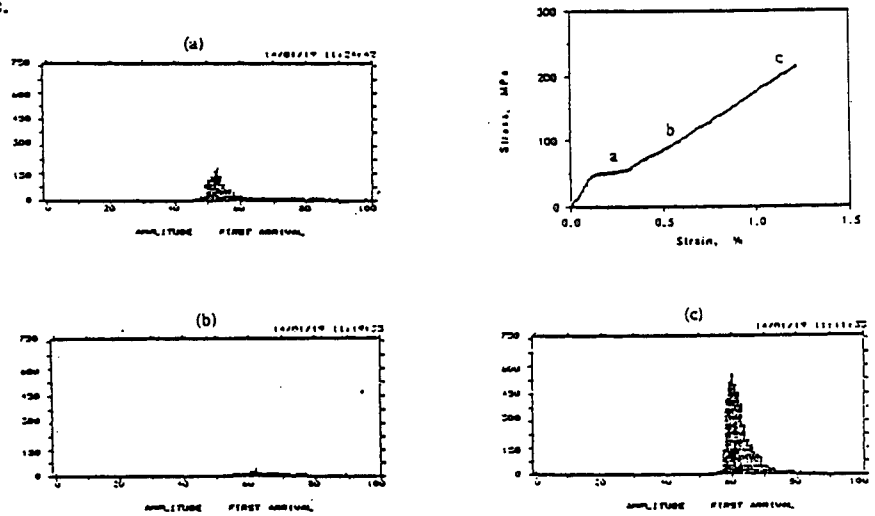

Figure 9. Amplitude Distributions at Various Stages During Tensile Testing

Summary

From the above presented review of glass and glass-ceramic matrix composite development, it can be seen that a broad range of material combinations has already been explored. Numerous suitable reinforcing fibers are available, matrix compositions have been identified, and fabrication processes have been demonstrated. Also, in all cases it has

been found that these composites must be treated as three component systems, i.e. fiber, matrix and fiber-matrix interfacial region. It is this last region of transition which appears to control the fracture process in these composites and hence their relative toughness.

The following points may be concluded as being important for fiber reinforced glass matrix composites.

- o Fiber, matrix and interface must all be tailored to achieve strong, tough composites.
- o Low fiber-matrix interfacial strength also implies low off axis strength.
- o Nonlinear stress-strain curves and an elastic modulus that decreases with increasing strain will have to be accounted for in successful designs if composites are to see use strain levels above ε_m, the matrix failure strain.
- o Environmental stability and composite structural life prediction will be the key issues for successful composite implementation.
- o Non structural composite performance such as tribology and dimensional stability may provide the keys to first composite usage at minimum risk of failure.

It is anticipated that the potential for fiber reinforced glass matrix composites is very significant and that the precise compositions of those materials to be most important are yet to be developed.

References

1. R. A. Sambell, D. C. Phillips, D. H. Bowen, "The Technology of Carbon Fibre Reinforced Glasses and Ceramics", Harwell Report AERE-R-7612, Feb. 1974.
2. S. R. Levitt, "High Strength Graphite Fibre-LAS", J. Mat. Sci, 8, 1973, p.793.
3. K. M. Prewo, J. F. Bacon, "Glass Matrix Composites-1, Graphite Fiber Reinforced Glass", Proc. Second Intl. Conf. on Composites, edited by B. Noton, AIME, 1978.
4. K. M. Prewo and E. R. Thompson, "Graphite Fiber Reinforced Glass", Proceedings of AIME Conf. Advanced Fibers and Composites for Elevated Temperatures, edited by I. Ahmad and B. Noton, 1979.
5. K. M. Prewo, E. R. Thompson, "Research on Graphite Reinforced Glass Matrix Composites", NASA Contract Report 165711, May 1981.
6. K. M. Prewo, J. F. Bacon and D. L. Dicus, "Graphite Fiber Reinforced Glass Matrix Composites", SAMPE Quarterly 10, (4), 42 (1979).
7. K. M. Prewo, E. J. Minford, "Graphite Fiber Reinforced Thermoplastic Matrix Composites for Use at 1000 F", SAMPE Jl. Vol. 21-2, March 1985.
8. V. D. Khanna, et al., "Friction and Wear of Glass Matrix-Graphite Fiber Composites", Proc. Mechanical Behavior of Metal Matrix Composites, edited by J. Hock, AIME, 1983.
9. E. Minford and K. Prewo, "Friction and Wear of Graphite Fiber Reinforced Glass Matrix Composites", to be published in the Journal Wear, 1985.
10. K. M. Prewo, "Development of a New Dimensionally and Thermally Stable Composite", Proceedings of the Special Topics in Advanced Composites Mtg, El. Segundo, Calif. 1979.
11. K. M. Prewo and E. J. Minford, "Thermal Stable Composites- Graphite Reinforced Glass", Proceedings of SPIE- the Intl. Society for Optical Engineers, Vol. 505, Aug. 1984.
12. J. Bacon, K. Prewo, R. Veltri, "Glass Matrix Composites-2-Alumina reinforced Glass", Proc. 1978 Intl. Conf. on Composite Materials, Toronto Canada 1978, Pub. by AIME.

13. A. C. Siefert, Method of Making Impact Resistant Inorganic Composites, U.S. Patent 3,702,240, Nov. 7, 1972 (applied April 1969).
14. K.M. Prewo and J. J. Brennan, "High Strength Silicon Carbide Fibre Reinforced Glass Matrix Composites", Jl. Mat. Sci, 15, 1980, p. 463.
15. S. Yajima, K. Okamura, J. Hayashi and M. Omori, "Synthesis of Continuous SiC Fibers with High Tensile Strength", Jl. Am. Ceramic Soc., Vol. 58, No. 7-8, 1976, p. 324.
16. K.M. Prewo and J. J. Brennan, "Silicon Carbide Fibre Reinforced Glass Matrix Composites", Jl. Mat. Sci, 17, 1982, p. 1201.
17. J. J. Brennan and K. M. Prewo, "Silicon Carbide Fibre Reinforced Glass-Ceramic Matrix Composites Exhibiting High Strength and Toughness", Jl. Mat. Sci, 17, 1982, 2371.
18. J.J. Brennan, "Interfacial Characterization of Glass and Glass-Ceramic Matrix-NICALON® SiC Fiber Composites", Proc. 21st University Conference on Ceramic Science, Penn. State Univ. July 1985.
19. K. M. Prewo,"A Compliant, High Failure Strain, Fibre Reinforced Glass-Matrix composite" J. Mater. Sci. 17(1982) p.3549.
20 O. Chen, N. Takeda, T. Kishi, W. Treadway, K. Prewo, "Fracture Mechanism of A High Compliance, High Failure Strain Glass Matrix Composite", Proc. 5th Japan-US Conference on Composites Materials, to be published.
21 O. Chen, N. Takeda, T. Kishi, W. Treadway, K. Prewo, "Acoustic Emission Characterization of the Fracture Mechanism of a High Compliant, Glass-Matrix Composite", International Conference on Advanced Materials Mechanical Properties, August 6-9, 1990, Utsunomia, Japan.
22 O. Chen, N. Takeda, T. Kishi, "Acoustic Emission Studies on Fracture Mechanisms of Randomly Oriented Carbon Fiber Reinforced Glass Matrix Composite", 10th International Conference on Acoustic Emission, October 22-25, 1990, Sendai, Japan

Organic Polymer-Containing Gels for Fine Patterning on Glass Substrates

Atsunori Matsuda and Yoshihiro Matsuno

Tsukuba Research Laboratory, Nippon Sheet Glass Co., Ltd.
5-4 Tokodai, Tsukuba, Ibaraki 300-26, Japan

ABSTRACT

Glass is one of the most promising substrate materials for optical memory disks in terms of optical properties, stability in an ambient atmosphere and so on.[1] In optical memory disks, fine patterns in the submicron scale, so-called pregrooves, are required for the tracking of a laser beam. Pregrooves are conventionally formed by a laser beam recording or by a contact printing on photoresist coated on a glass substrate, developing of the photoresist and etching of the glass substrate.[2-5] These techniques, however, consist of complicated processes and need expensive equipments. To overcome these difficulties, we have proposed a new technique to form pregrooves on glass substrates, based on the sol-gel coating process.[6,7] The technique consists of the following simple steps: (1) formation of an organic polymer-containing gel film on a glass substrate, (2) patterning on the gel film by pressing a stamper, and (3) heat-treatment to decompose the organic polymer and to convert the gel film into the glass film.

The key point of the fabrication of pregrooves by this technique is the patterning by pressing a stamper against the gel

films, the hardness of which is controlled by incorporation of organic polymers. Among the organic polymers examined polyether glycols such as polyethylene glycol (PEG) have been found to be the most suitable for the patterning. Recently, we have also found that the gel-derived SiO_2-TiO_2 coating films provide soda-lime-silica glass substrates with excellent weathering resistance[8] and their refractive indices can be easily controlled by adjusting the TiO_2 content[9]. It is thus expected that pregrooved glass disks with a good weathering resistance and with a good property are obtainable using the SiO_2-TiO_2 films.[10]

In the present work,[11] the effects of the addition of PEG on viscosity of the sols, hardness of the gel films and formation of the gel-derived glass films in the SiO_2-TiO_2 system have been studied relative to their application to the fine-patterning technique for optical memory disks. Moreover the pregrooves have been formed on soda-lime-silica glass disks of 130 mm in diameter using the PEG-containing SiO_2-TiO_2 gel films, and the qualities of the pregrooved glass disks have been evaluated.

The viscosity of the PEG-containing sols increased almost linearly with increasing PEG content and the addition of PEG to the sols affected very slightly the temperature dependence of the viscosity increase of the sols with the storage time. These findings show that PEG added to the SiO_2-TiO_2 sol has no reaction with the hydrolyzed inorganic species. The viscosity increase of the sols during the storage and the hardness of the resultant PEG-containing gel films greatly decreased with increasing PEG content. The average molecular weight of PEG added also affected

the viscosity increase of the sol and the hardness of the films obtained; PEG of the smaller average molecular weight slowed down more effectively the viscosity increase during the storage and gave harder films than PEG of larger molecular weight. The addition of PEG of the smaller average molecular weight probably produced the stiff and small colloidal particles, and thus produced the densified gel-structure. Incorporated PEG in the SiO_2-TiO_2 gel films decomposed completely at temperatures over 300°C. The decomposition of PEG showed very slight influence on chemical bondings in the resultant films heat-treated over 300°C.

It was found that precise pregrooves were uniformly formed in the SiO_2-TiO_2 films on the glass disks of 130 mm in diameter by the fine-pattening technique. When the weight ratio of PEG with the average molecular weight of 600 to SiO_2-TiO_2 oxides was unity, the pitch of the pregrooves formed was unchanged compared to that of the stamper used after the heat-treatment at 350°C, while the land height and the land width of the pregrooves were respectively reduced to 60% and 85% of those of the stamper after the heat-treatment. The noise level of the glass disks with the pregrooved SiO_2-TiO_2 layer was lower than that of the disks obtained using pure SiO_2 layer in the frequency range from 0.5 to 2.0 MHz at 1800 rpm. The lower noise level of the former can be ascribed to the agreement in the refractive index between the pregrooved layer and the glass disks.

References

1. J. Henning, Proc. Int. Symp. on Optical Memory, Jpn. J. Appl. Phy., **26**, Supplement 26-4, 9-14 (1985).

2. K. Ohta, J. Hirokane, T. Inui, A. Takahashi, T. Deguchi and T. Okamoto, J. Vacuum Soc. of Jpn., **28** [2] 77-81 (1985).

3. M. Miyagi, A. Iwasa and H. Yamasaki, Proc. Int. Symp. on Optical Memory, Jpn. J. Appl. Phy., **26** Supplement 26-4, 83-86 (1987).

4. K. Ohta, Y. Nagahara, J. Hirokane, K. Van and T. Inui, Extended Abstracts (The 35th Spring Meeting); The Japan Society of Applied Physics and Related Societies, No.3, p.869, 29a-ZQ-2, (1988).

5. J. Hirokane, Y. Nagahara, K. Van, A. Takahashi, T. Inui and K. Ohta, Extended Abstracts (The 35th Spring Meeting); The Japan Society of Applied Physics and Related Societies, No.3, p.869, 29a-ZQ-3 (1988).

6. N. Tohge, A. Matsuda, T. Minami, Y. Matsuno, S. Katayama and Y. Ikeda, J. Non-Cryst. Solids, **100** 501-505 (1988).

7. N. Tohge, A. Matsuda, T. Minami, Y. Matsuno, S. Katayama and Y. Ikeda, J. Ceram. Soc. Jpn., **96** [12] 1127-1130 (1988).

8. A. Matsuda, Y. Matsuno, S. Katayama and T. Tsuno, J. Mater. Sci. Lett., **8** 902-904 (1989).

9. Y. Matsuno, A. Matsuda, S. Kataoka, S. Katayama and T. Tsuno, Proc. 1st Jpn Int. SAMPE Symp. Nov.28-Dec.1, 295-300 (1989).

10. A. Matsuda, Y. Matsuno, S. Katayama, T. Tsuno, N. Tohge and T. Minami, J. Am. Ceram. Soc., **73** [8] 2217-2221 (1990).

11. A. Matsuda, Y. Matsuno, S. Kataoka, S. Katayama, T. Tsuno, N. Tohge and T. Minami, Proc. SPIE's 1990 Int. Symp., Sol-Gel Opt. 8-13 Jul., in press.

Table 1. Organic additives examined

Organic additives	Formula	Patterning	Remarks
Polyvinyl alcohol (PVA)	$-\{CH_2CH(OH)\}_n-$	×	Low solubility in alcohol
Cellulose acetate	$-\{C_6H_8O_3(OCOCH_3)_2\}_n-$	×	
Cellulose nitrate	$-\{C_6H_8O_3(NO_3)_2\}_n-$	△	Poor optical property
Hydroxypropyl cellulose (HPC)	$-\{C_6H_7O_5(C_3H_6OH)_3\}_n-$	×	Hard gel film
Polyethylene glycol (PEG)	$HO\{C_2H_4O\}_n H$	○	Good optical property
Polytetramethylene glycol (Terathane®)	$HO\{C_4H_8O\}_n H$	○	
Formamide	$HCONH_2$	×	Hard gel film

×: Failure △: Fair ○: Excellent

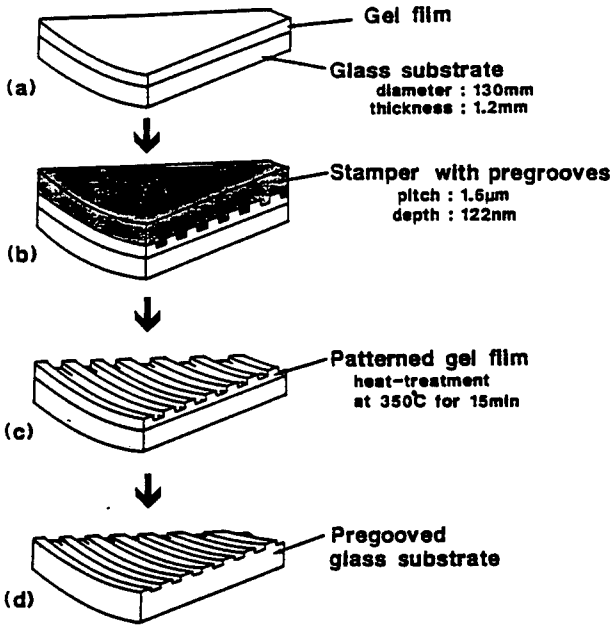

Fig.1. Pregrooving process by the sol-gel method; (a)formation of a gel film on a glass substrate, (b)patterning on the gel film, (c)heat-treatment, and (d)the pregrooved glass substrate.

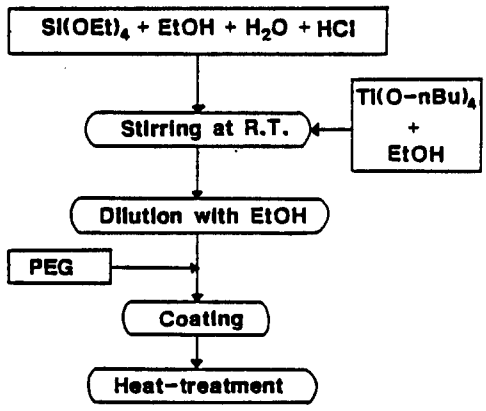

Fig.2. Preparation procedure of polyethylene glycol(PEG)-containing SiO_2-TiO_2 solutions.

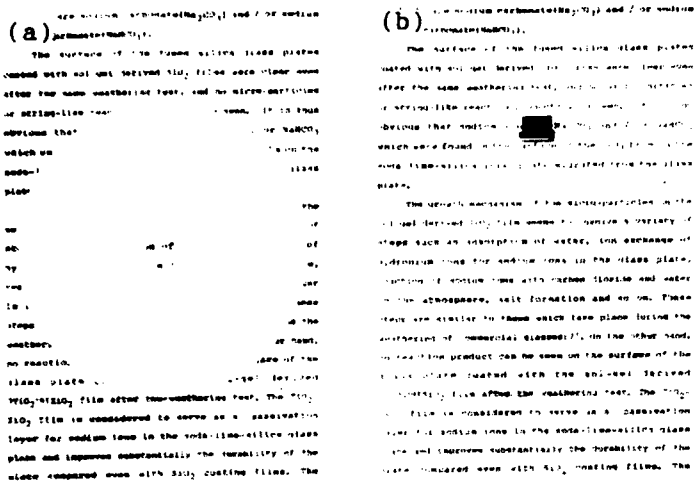

Fig.3. Photographs of the chemically strengthened soda-lime-silica glass disks of 130 mm in diameter and 1.2 mm in thickness after weathering tests. (a) is for the disk without coating and (b) with $83.5SiO_2 \cdot 16.5TiO_2$ coatings. The weathering tests were performed for 50 h at 135 °C and 90% R.H.

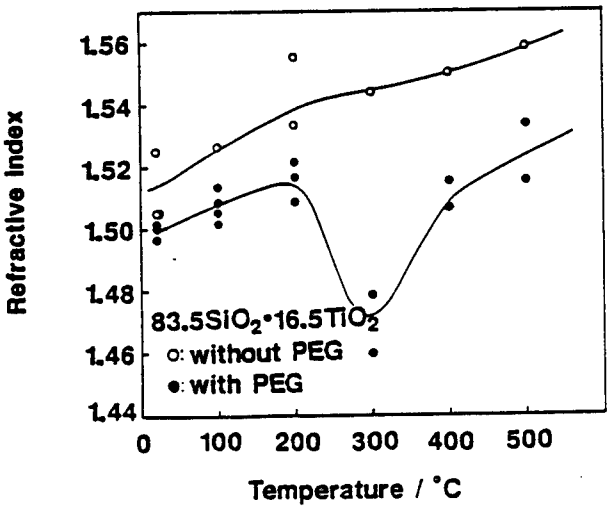

Fig.4. Variations of refractive index of $83.5SiO_2 \cdot 16.5TiO_2$ films with heat-treatment; open and closed circles are respectively for the films obtained without PEG and with the addition of PEG. The weight ratio of PEG600 added to oxides is unity.

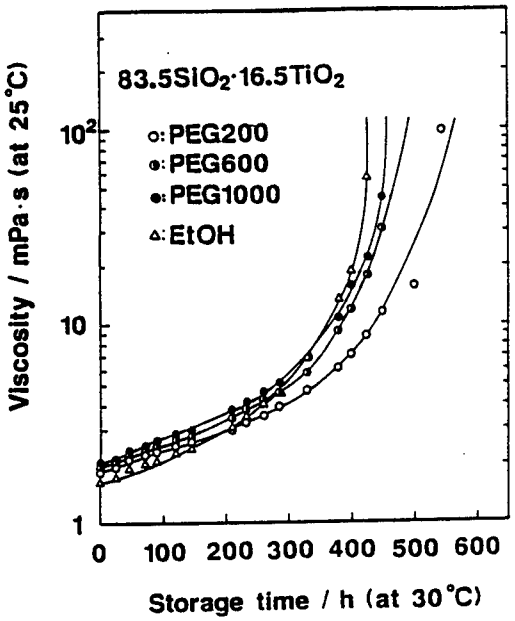

Fig.5. Variations in viscosity of the PEG-containing sols stored at 30°C as a function of storage time. The viscosity of the solutions was measured at 25°C. Open, half-closed and closed circles show PEG of average molecular weight of 200, 600 and 1000, respectively. Triangles show ethanol. For each sols, the additive/oxides weight ratio is unity.

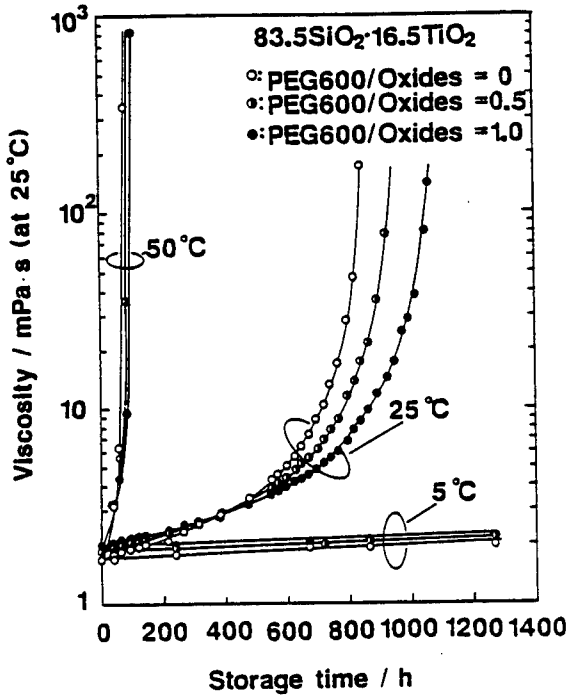

Fig.6. Variations in viscosity of the sols containing different amounts of PEG600 as a function of storage time at temperatures 5, 25 and 50°C. Open, half-closed and closed circles represent PEG600/oxides weight ratio= 0, 0.5 and 1.0, respectively.

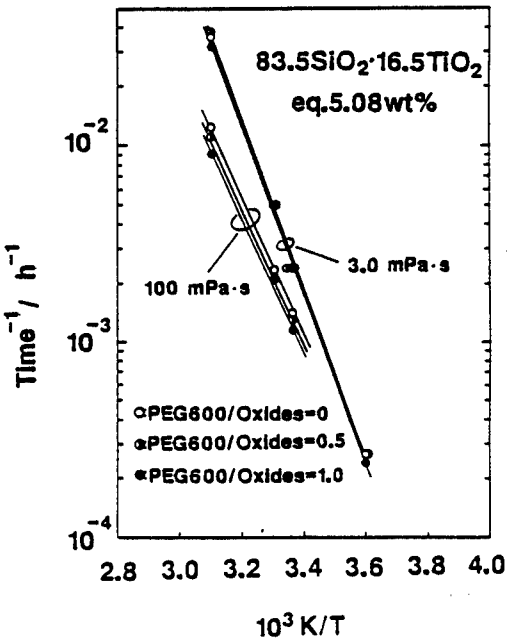

Fig.7. Temperature dependencies of the inverse of the time at which the viscosity of the sols becomes a given value, 3.0 and 100 mPas. Open, half-closed and closed circles have the same meanings as in Fig. 6.

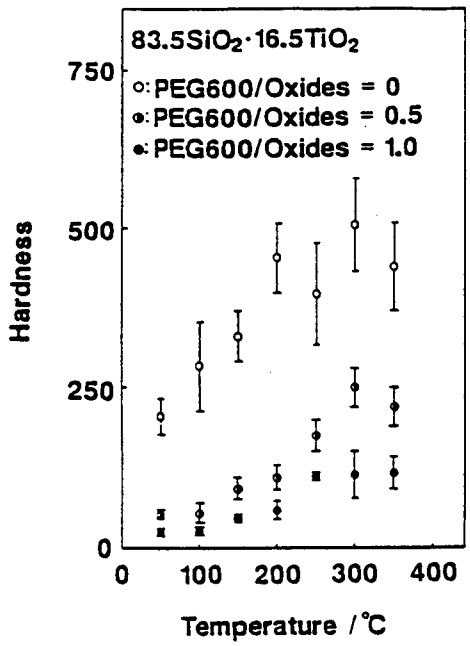

Fig.8. Comparison of hardness of the films containing different amounts of PEG600 as a function of heat-treatment temperature. Open, half-closed and closed circles represent PEG600/oxides weight ratio= 0, 0.5 and 1.0, respectively.

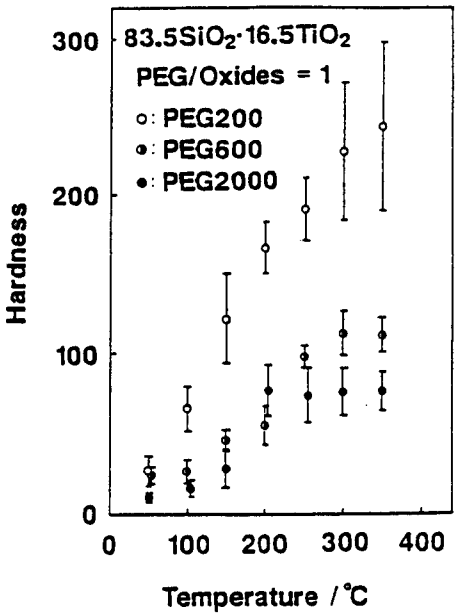

Fig.9. Variations of hardness of the films obtained with the addition of PEG of different molecular weight as a function of heat-treatment temperature. Open, half-closed and closed circles represents the gel films containing PEG200, PEG600 and PEG2000, respectively. For all the films, PEG/oxides weight ratio is unity.

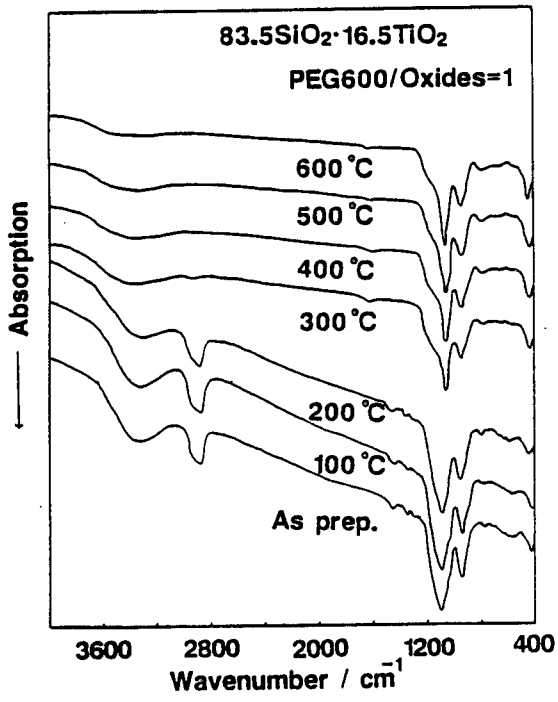

Fig.10. IR absorption spectra of the $83.5SiO_2 \cdot 16.5TiO_2$ films obtained with the addition of PEG600, the weight ratio of PEG to the oxides being unity, as a function of heat-treatment temperature. All the films were heat-treated at each temperature for 15 min.

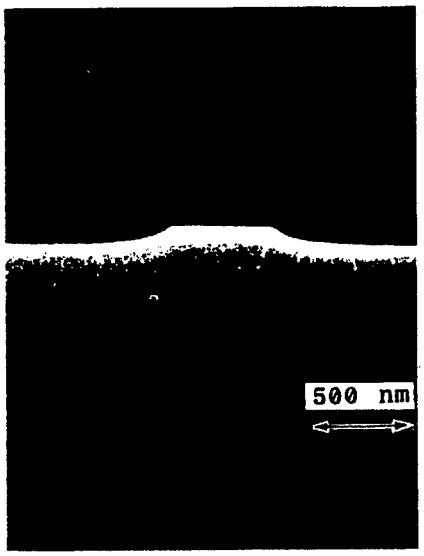

Fig.11. SEM cross-section of TiO_2-SiO_2 pregrooves fabricated on a glass disk of 130 mm in diameter by the present fine patterning technique.

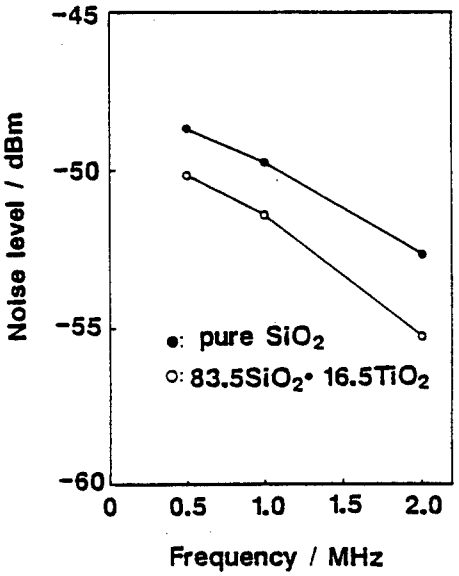

Fig.12. Frequency dependence of noise levels for the fabricated glass disks. Open and closed circles show the disks with pregrooved $83.5SiO_2$• $16.5TiO_2$ layer and with pregrooved pure SiO_2 layer, respectively.

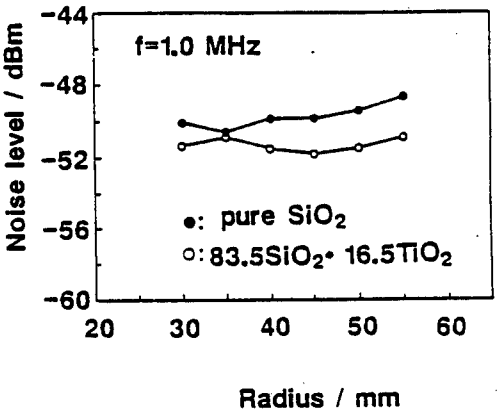

Fig.13. Radial variation of noise levels for the fabricated glass disks at the frequency of 1.0 MHz. Open and closed circles have the same meanings as described in Fig.12.

SESSION III

(2)

DUCTILE REGIME GRINDING AND MACHINING OF BRITTLE MATERIALS

R. O. Scattergood
Precision Engineering Center
North Carolina State University
Raleigh, NC 27695-7918

Recent work being carried out at the Precision Engineering Center will be discussed. Ductile-to-brittle transitions and ductile-regime machining or grinding have been investigated using single-point diamond turning, plunge-grinding and cross-feed grinding for a range of brittle materials. Because of the simpler geometry involved, single-point diamond turning is the most amenable process for fundamental studies. An interrupted cutting test was developed which allows the ductile-to-brittle transition to be directly observed in diamond turning experiments. Fracture mechanics models have been developed based on the concept of a critical cutting depth. Two damage parameters are important in this context - a critical cutting depth d_c and an associated fracture damage depth y_c. The effect of machining geometry and chip profile is a very important aspect of the process. Results from single-point diamond turning experiments will be compared to model predictions. Plunge-grinding experiments (no cross feed) on a laboratory-scale grinding apparatus were made to investigate the material-property dependence of the critical depth parameter d_c in grinding mode conditions. A wide range of brittle materials (single crystal Si and Ge, ceramics and glasses) were used for these studies. In general the results agree well with predictions from fracture mechanics models. Critical depth values are the order of 10 - 100 nm for very brittle materials like glass. Certain ceramics show significant deviation from the predicted correlation, and this has been attribute to microstructure-controlled crack-growth resistance effects (R-curve). A cross-feed grinding system has been implemented in very recent work, along with facilities for interrupted tests. Computer simulation methods have been used to model the grinding chip profile. Initial results will be compared with the predictions. The relevance to commercial grinding technologies will be discussed.

Professor Ronald O. Scattergood

Department of Materials Engineering
North Carolina State University
Raleigh, NC 27695-7907
919-737-7843/3096

Education:

BS	1961	Metallurgical Engineering	Lehigh University
MS	1963	Metallurgy	M. I. T.
ScD	1968	Metallurgy	M. I. T.

Employment Record:

1968 - 1981 Staff Scientist - Basic Research
Argonne National Laboratory
Materials Science Division
Argonne, IL 60439

1973 - 1974 SRC Research Fellow
University of Liverpool
Liverpool, UK

1981 - Professor of Materials Engineering
North Carolina State University
Department of Materials Science & Engineering
Raleigh, NC 27695-7907

Professional Activities:

Member - ASM, AIME, MRS, ASPE, ACS
Associate Director, Precision Engineering Center
Board of Directors, American Society for Precision Engineering

Research Interests:

Mechanics and physics of materials with emphasis on mechanical behavior and fracture mechanics. Current interests include tribology, fracture processes in advanced ceramics, and precision engineering. Approximately 130 publications and technical reports.

The American Society of Mechanical Engineers

Reprinted From
Machining of Advanced Ceramic Materials and Components—1988
Editors: S. Chandrasekar, R. Komanduri, W. Daniels, and W. Rap
(Book No. G00439)

BASIC STUDY ON MACHINABILITY OF ZIRCONIA CERAMICS IN PRECISION DIAMOND CUTTING

T. Moriwaki and K. Iwata
Kobe University
Nada, Kobe, Japan

K. Okuda
Kobe Technical College
Tarumi, Kobe, Japan

ABSTRACT

Experimental investigations on precision machining of zirconia ceramics with diamond tools are carried out employing an ultra-high precision milling machine for fly cutting in order to show feasibility of precision diamond machining of ceramic materials and to identify the problems involved. The three components of the cutting forces and the surface roughness are measured. The finished surface, the wear and damage of cutting tool and the formed chips are also observed employing a differential interference microscope and a scanning electron microscope. The surface roughness less than 0.1 μm in R_{max} was obtained by cutting with a single crystal diamond tool up to a cutting distance of 1000 m when proper cutting conditions were selected. The machinability of zirconia ceramics are discussed in the paper based on the experimental results.

INTRODUCTION

The ceramic materials have been widely adopted as functional materials as well as structural materials in various industrial fields, and their applications to precision parts are also increasing[1]. However, high dimensional accuracy and good surface quality required for the precision parts are not necessarily obtained by conventional forming and sintering process of the ceramic powder. Thus, precision finishing of the ceramics after the forming and sintering is recognized as a key technology to precision ceramic parts.

The quantity of ceramic materials to be removed by finishing process must be very small, so that micro craks will not remain on the finished surface, in order not to deteriorate the performance of the parts. The abrasive processing such as grinding or lapping with diamond abrasives has been generally adopted for precision finishing of ceramics[2,3,4].

It is however, expected that better surface integrity and higher production rate are realized by cutting process, once suitable machines, tools and machining technologies are established. The cutting is also advantageous in making complex shapes in comparison to the other processes. Precision cutting of ceramic materials is a new technology, and there is not much known about machinability of ceramic materials.

In this study, basic experimental investigations on precision diamond cutting of zirconia ceramics are carried out in order to show feasibility of precision diamond cutting of ceramic materials and to identify the problems involved. In the present paper, the machinability of zirconia ceramics is mainly discussed from the viewpoints of the cutting forces, the surface roughnesses, the chip formation and the tool wear.

EXPERIMENTAL EQUIPMENT AND PROCEDURES

An ultra-high precision milling machine for fly cutting is employed for the cutting experiments. Figure 1 shows the overview of the machine and the attached equipment schematically. The cutting machine is required to have high accuracy and high rigidity in order to carry out precision machining of ceramic materials. The main spindle of experimental machine is supported by precision hydrostatic oil bearings and driven by an A.C. motor fixed on an isolated base via a specially ground flat belt. The work table is supported by precision hydrostatic oil ways and is coupled to a drive table driven by a D.C. motor via a pneumatic coupling. The machine base is made of cast iron and is supported by three air

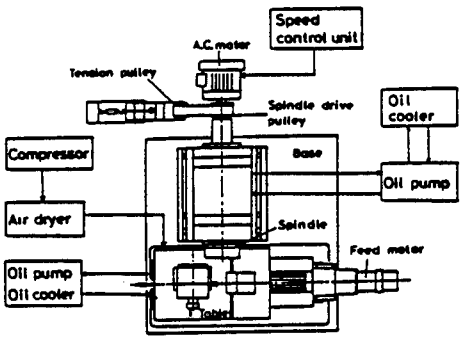

Fig.1 Overview of ultra-high precision milling machine for fly cutting.

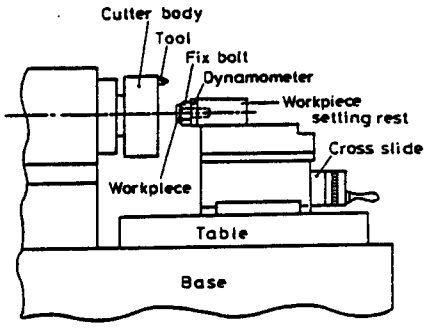

Fig.2 Arrangement for cutting experiment and cutting force measurement.

mounts in order to prevent the external vibrational disturbances.

A special arrangement developed to measure the three components of the cutting forces in fly cutting is shown schematically in Fig.2. A piezo-electric three-component dynamometer is fixed to the workpiece setting rest on the cross slide with a special bolt made of invar. The plate type workpiece is pasted on the top surface of the bolt with instant adhesive agent.

The zirconia ceramics which consists of ZrO_2 and very small amount of metal oxides is employed as the work material, which showed relatively good machinability in the preliminary cutting test. The alumina ceramics were hard to be cut with even diamond tools, and its test results are not included here. The average diameter of zirconia grain is about 0.5 μm. The materials of cutting tool used are both natural single crystal diamond and sintered synthetic diamond.

Table 1 summarizes the materials and the geometries of the cutting tools and the major cutting conditions. The typical cutting conditions are 85 to 255 m/min for the cutting speed, 2 to 50 μm/rev for the feed rate and 0.5 to 2 μm for the depth of cut.

Table 1 Experimental conditions.

Work material	Zirconia ceramic size 20x15x5 mm
Tool materials and tool geometries	Single crystal diamond R: nose radius 1.0, 5.0 mm α: rake angle -3, 0, 3° Sintered diamond R: nose radius 0.2, 1.0 mm α: rake angle -3, 0°
Spindle speed	150, 300, 450 rpm
Cutting speed	85, 170, 255 m/min
Feed rate	2 - 50 μm/rev
Depth of cut	0.5 - 2 μm

EXPERIMENTAL RESULTS AND DISCUSSIONS

Cutting forces

Figure 3 shows examples of the cutting forces measured during one pass of the fly cutting. The figure compares the main cutting force component, the feed force component and the thrust force component for both the single crystal diamond tool and the sintered diamond tool. The magnitude of feed force component is much smaller as compared with the other components. The figure shows that the magnitude of the thrust force component is larger than that of the main cutting force component and that the cutting forces obtained during cutting with the single crystal diamond tool are smaller than those with the sintered diamond tool.

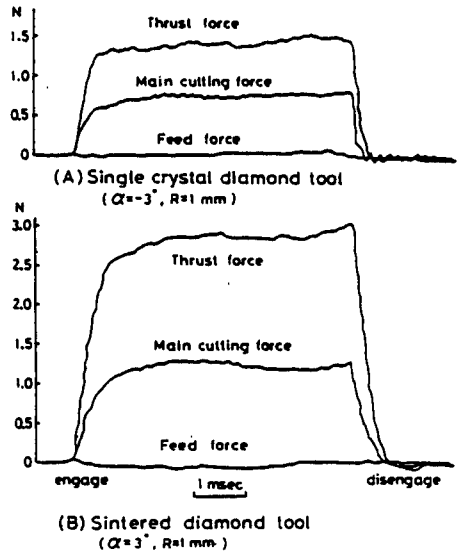

Fig.3 Example of cutting force components measure. (Cutting speed=170 m/min, Feed rate=5 μm/rev, Depth of cut=1 μm)

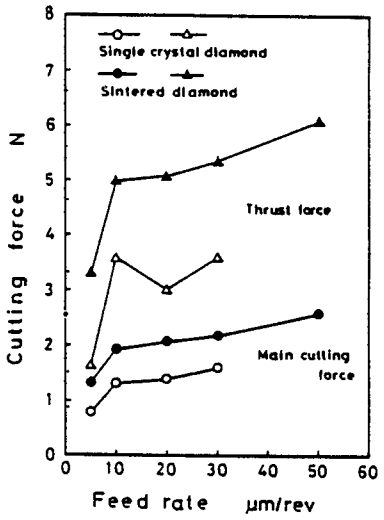

Fig.4 Effect of feed rate on cutting forces. (Tool: Single crystal diamond, α=3°, R=1 mm and Sintered diamond, α=-3°, R=1 mm, Cutting speed=170 m/min, Depth of cut=1 μm)

The effect of the feed rate on the main cutting force and thrust force components is shown in Fig.4. It is understood that the thrust force component is almost twice as large as the main cutting force component in magnitude. It is noteworthy that the thrust force component is the largest among the three components of cutting forces in cutting of zirconia ceramics. The cutting test results of other materials obtained under similar cutting conditions show that the main cutting force component is by far the largest in cutting of copper with diamond tools[5], and that the main cutting force and thrust force components are almost equal in magnitude in cutting of stainless steel with CBN tool[6].

All the three components of the cutting forces in cutting of zirconia ceramics are more than ten times as large as those of copper respectively obtained under the same cutting conditions. The reason for the large thrust force component in cutting of zirconia ceramics is attributable to high hardness of zirconia ceramics.

Each component of the cutting forces shown in the figure is smaller when the zirconia ceramics is cut with the single crystal diamond tool than when cut with the sintered diamond tool. It is understood that the difference in the cutting forces is due to the difference in the sharpness of the cutting edges.

The figure shows that the cutting force components increase with an increase in the feed rate. However, the rate of increase is not proportional to the feed rate. The nominal specific cutting resistance calculated by dividing the measured cutting force by the theoretical cross sectional area of cut becomes extremely large at lower feed rates. The nominal specific cutting resistance of main cutting force component reaches to 100000 MPa, which is greater than the theoretical shear strength of work material. The nominal uncut chip thickness under such small feed rate conditions is far less than the depth of cut, and therefore the roundness of cutting edge plays an important role in determining the cutting forces.

Surface Roughness

Figure 5 shows examples of the surface roughnesses in R_{max} measured when the feed rate was varied from 5 to 50 μm/rev. The cutting tools are the single

crystal and sintered diamond tools. The theoretical surface roughness calculated is also shown in the figure by a dotted curve. The surface roughneses obtained by cutting with the single crystal diamond tool is relatively in good agreement with the theoretical one, while that obtained with the sintered diamond tool is much larger than the theoretical one. The relative discrepancy between the two becomes larger especially at lower feed rates.

According to the previous works of the authors[7], it was found that the surface roughnesses of copper cut with the single crystal diamond tool under the similar cutting conditions were in much better agreement with the theoretical one. This implys that the mechanics of cutting process is different between the metallic material and the ceramics which is a sintered materials. The surface roughness of the zirconia ceramics shown in the figure is much better when it is cut with the single crystal diamond tool than with the sintered one, and it reaches below 0.05 μm at the feed rate of 5 μm/rev.

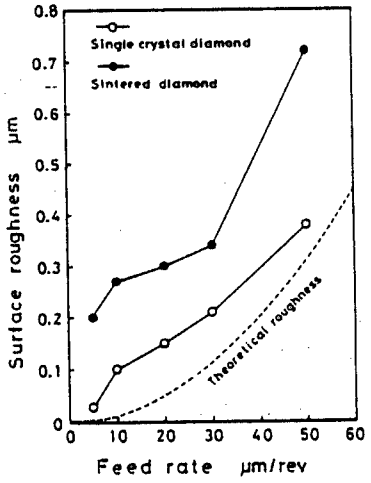

Fig.5 Effect of feed rate on surface roughness. (Tool: Single crystal diamond, α=3°, R=1 mm and Sintered diamond, α=-3°, R=1 mm, Cutting speed=170 m/min, Depth of cut=1 μm)

The photographs of the finished surfaces taken by a differential interference microscope and their surface profiles are shown in Fig. 6, which are obtained at the cutting distance of about 250 m after the start of cutting. The regular and periodical cutter marks with a constant pitch corresponding to the feed are observed on the finished surfaces shown in the figure. The photographs and the profiles of finished surfaces indicate that normal cutting of zirconia

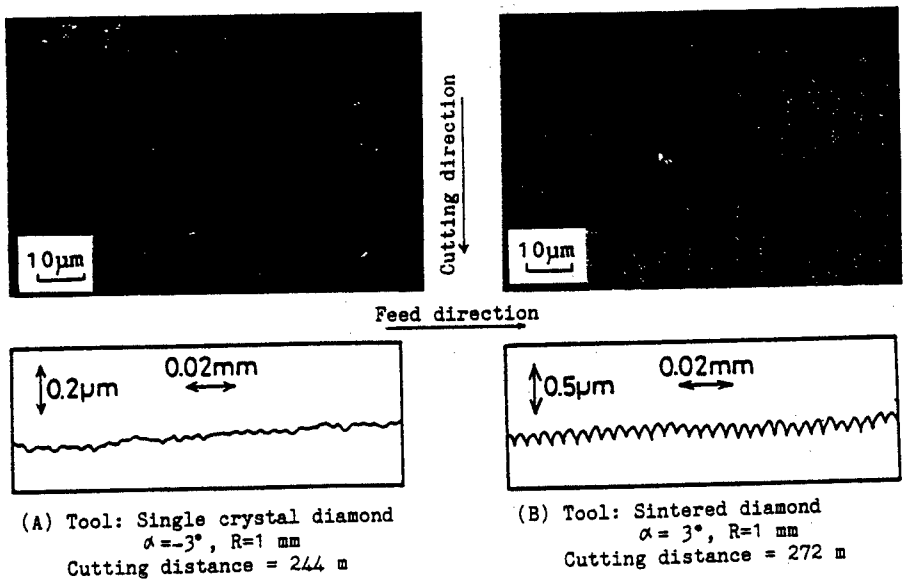

(A) Tool: Single crystal diamond
α=-3°, R=1 mm
Cutting distance = 244 m

(B) Tool: Sintered diamond
α= 3°, R=1 mm
Cutting distance = 272 m

Fig.6 Photographs taken by differential interference microscope and profiles of finished surfaces. (Cutting speed=170 m/min, Feed rate=5 μm/rev, Depth of cut=1 μm)

ceramics is performed, though some vacancies generated by plowing out of the ceramic grains or some defects included in the workpiece are remaining on the finished surface. The distinguished feed mark on the surface finished with the sintered diamond tool is due to the groove-like flank wear of the cutting edges which is discussed later.

It is confirmed through the experiments that the surface roughnesses of less than 0.1 μm in R_{max} can be obtained by machining with the single crystal diamond tool at low feed rates. It is understood that the micro cutting with sharp single crystal diamond tool at small depth of cut and small feed rate is indispensable in order to obtain good surface finish. In the case of sintered diamond tool, the surface roughnesses of less than 0.1 μm were not obtained within the range of cutting conditions in the present experiments.

Figure 7 shows a photograph of finished surface of workpiece. The surface roughness obtained is 0.05 μm in R_{max} excluding the inherent defects of the material. It is seen that a mirror surface of zirconia ceramics is obtained.

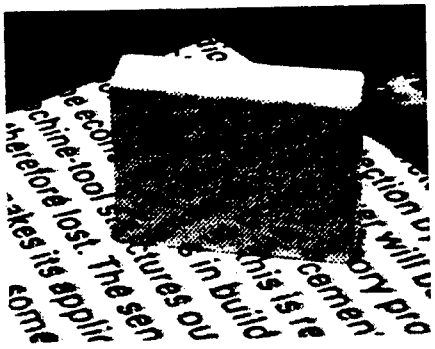

Fig.7 Photograph of finished surface of workpiece. (Tool: Single crystal diamond, α =-3°, R=5 mm, Cutting speed=170 m/min, Feed rate=5 μm/rev, Depth of cut=2 μm)

Cip Formation

SEM photographs of chips formed by cutting with the single crystal and sintered diamond tools are shown in Fig.8. The chips shown in the figure are not of continuous type like those of metals such as copper. However, it is obvious from figure (A) that the chips are formed by normal cutting and the apparent plastic deformation takes place in the chip formation. The discontinuous chips are observed in the case of the sintered diamond tool in figure (B), which are similar to the shear type chips formed typically in cutting of brass.

The chips formed in cutting of alumina ceramics were broken into pieces of alumina grains and the brittle failure of ceramic workpiece by crack propagation predominated in the chip formation. This is due to the fact that the zirconia ceramics has higher toughness than the alumina ceramics.

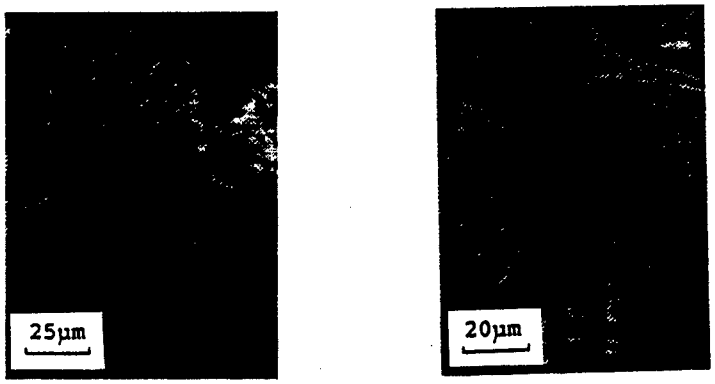

(A) Tool: Single crystal diamond α =-3°, R=1 mm

(B) Tool: Sintered diamond α = 3°, R=1 mm

Fig.8 SEM photographs of chips. (Cutting speed=170 m/min, Feed rate=5 μm/rev, Depth of cut=1 μm)

Wear of Cutting Tool

Typical examples of the photographs of worn flank faces of tool are shown in Fig.9. The pictures are taken with a differential interference microscope. The scratched patterns left on the flank faces indicate that the abrasive wear of flank face by the ceramic grains is predominant. The groove wear due to scratching is clearly observed on the flank face of sintered diamond tool at a regular interval of 5 μm corresponding to the feed. As it was shown in Fig.6, the scratched patterns of flank face are copied on the surface of finished workpiece. The scratches are often generated in the case of low feed rate less than 10 μm/rev. This is expected due to the fact that the binder of sintered diamond tool is selectively abraded, when the feed is close to the grain size of sintered diamond. The mean diameter of grains is about 5 μm.

The flank face of single crystal diamond is scratched at irregular intervals, but the form of cutting edge is kept relatively closer to the initial form as compared with the sintered diamond tool. This is one of the reasons for that the surface roughness obtained by the single crystal diamond tool is better than that obtained by the sintered diamond tool.

In the case of cutting at higher speeds, such as 500 m/min or more, which is realized by employing a precision spindle supported by hydrostatic air bearings, the abrasive wear was scarcely observed, but the brittle failures such as chipping and cracking took place on the rake face. Good surface finish was not obtained due to the rapid progress of the tool failure in this case. The brittle failure of tool was also observed at low cutting speed, typically 85 m/min, when the cutting test was carried out with the spindle supported by the hydrostatic oil bearings. Thus, there exists optimum cutting speed range from the viewpoint of tool life.

Figure 10 shows the effects of cutting distance on the flank wear of single crystal diamond tool and the surface roughnesses in R_{max}. Both the flank wear and the surface roughness increase with an increase in the cutting distance. The flank wear reaches to about 50 μm at the cutting distance of 304 m. The flank wear of 50 μm is quite large in the precision machining and it is expected that the dimensional accuracy is much affected. However, the surface roughness is still kept less than 0.1 μm in R_{max}.

The effect of cutting distance on the flank wear of sintered diamond tool is shown in Fig.11 for three cutting speed. The flank wear increases with an increase in the cutting distance at each cutting speed. The flank wear shows the largest at cutting speed of 85 m/min among the three cutting speeds tested, and the tool failure took place at the cutting distance of about 500 m in this case. The flank wear of sintered diamond tool is relatively small as compared with that of single crystal diamond tool shown in Fig.10.

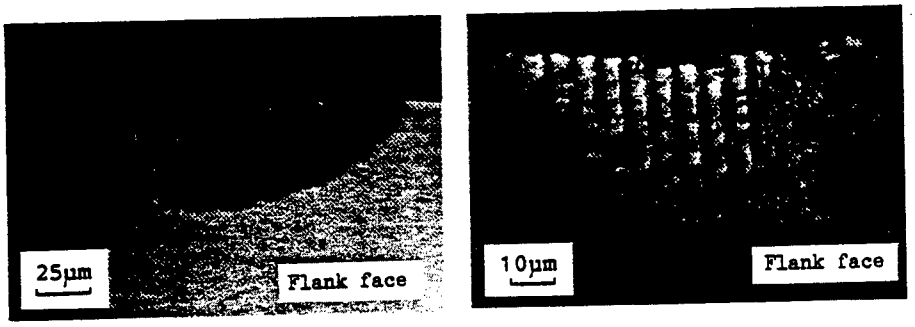

(A) Tool: Single crystal diamond
(α =-3°, R=1 mm,
Cutting distance=304 m)

(B) Tool: Sintered diamond
(α = 0°, R=0.2 mm,
Cutting distance=272 m)

Fig.9 Photographs of worn flank faces of cutting tools.
(Cutting speed=170 m/min, Feed rate=5 μm/rev, Depth of cut=1 μm)

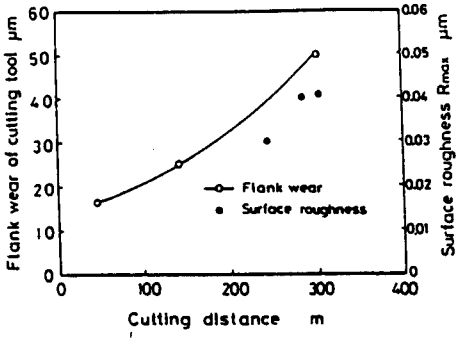

Fig.10 Effects of cutting distance on flank wear of cutting tool and surface roughness. (Tool: Single crystal diamond, α=-3°, R=1 mm, Cutting speed=170 m/min, Feed rate= 5 μm/rev, Depth of cut=1 μm)

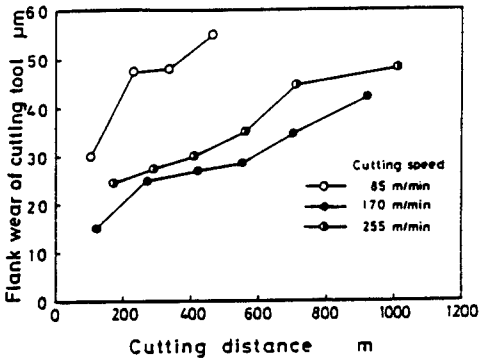

Fig.11 Effect of cutting distance on flank wear of cutting tool. (Tool: Sintered diamond, α= 0°, R=0.2 mm, Feed rate=5 μm/rev, Depth of cut=1 μm)

The cutting tests were continued for the cutting distance up to 1000 m, and it is identified that the surface roughness of 0.1 - 0.2 μm in R_{max} is obtained with the sintered diamond tool and that of less than 0.1 μm, with the single crystal diamond tool.

CONCLUSIONS

The ultra-high precision machining of zirconia ceramics was carried out employing the diamond cutting tools on an ultra-high precision milling machine for fly cutting. The machinability of the zirconia ceramics is discussed from the viewpoints of the cutting forces, the surface roughness, the chip formation and the wear of cutting tool. The following remarks are concluded.

1. The thrust force component is the largest among the three components of the cutting forces measured. The cutting forces increase with an increase in the feed rate, however, the nominal specific cutting resistance becomes extremely large at lower feed rates.
2. The normal chip formation takes place in cutting of zirconia ceramics with diamond tools as in the case of conventional cutting of metals. The chips are formed in association with the plastic deformation of work material.
3. The surface roughness of 0.1 to 0.2 um in R_{max} is obtained steadily by cutting with the sintered diamond tool for the cutting distance up to 1000 m by selecting appropriate cutting conditions. The surface roughness of less than 0.1 μm in R_{max}, except the defects of the material and the vacancies generated by plowing of the ceramic grains, is obtained by cutting with the single crystal diamond tool.
4. There exist optimum cutting conditions, especially cutting speed, for long tool life. The supression of tool wear is key to generate good surface quality steadily.

REFERENCES

1. T.Furukawa, N.Moronuki, K.Kitagawa ; "Development of ultra precision machine tool made of ceramics", Annals of the CIRP, Vol.35, No.1, 1986, p55.
2. R.Murata, K.Okano, C.Tsutumi ; "Grinding of strauctural ceramics (some application of electrolytic in-process dressing to abrasive cut-off operation)", Milton C.Shaw Grinding Synposium, PED-Vol.16, ASME, 1985, p261.

Elastic Emission Machining Technology for Glass material Optics

J.Takashita
CANON Inc.

A. Improvement of Surface Quality

A-1.Introduction

Surface scattering for short wave length optical elements such as excimer and soft X-rays should be reduced as small as possible, and the surface scattering depends upon the surface roughness of the elements. This work determined conditions to reduce the surface roughness for various polishing factors,and removal characteristics against microswell(ripple) by using a polishing device based on the principle of E.E.M(Elastic Emission Machining).

A-2.Behavior Analysis for Polishing Fluid and Particle

Removal efficencies of both the static pressure and dynamic prssures systems were determined by analyzing a flow carrying particles and the behavior of particles using a simple two-dimensional model. In the static pressure system,assuming that the land portion of a cylindrical tool is inclined, feed a fluid under a pressure differential, P_0-P_a.

In the dynamic pressure system, on the other hand, assuming that the tool upstream is larger clearance-shaped than downstream, a flow occurs when the wall surface of tool travels at a constant velocity[1]. On the asumption for these models that a fluid in the boundary adheres to the wall surface, the flow is laminar and has no inertia force, the pressure is constant in the film thickness direction of the fluid, and the polishing fluid is Newtonian fluid, we determined the stream line and locus of particles by setting up the Navier-Stokes equation. As shown in Fig.A1, it is in the dynamic pressure system that the parti-

cles are easy to reach the surface of a work,and a diffrence of two--digit in removal rate was seen in actual polishing.

A-3.Experimental Device and Method

Fig.A2 shows the experimental device for polishing used to apply pressure to the tool, use a parallel hinge leaf spring mechanism with spring constant of 11.2grm/ μ m, and set the applied pressure with a displacement at the movable end. For the work, use synthetic quartz 50mm dia. × 10mm thick. For the tool, finish an urethane resin semi--sphere with a radius of curvature of 25mm within 0.3 μ m in roundness in the direction of rotation for use. For the polishing fluid, dissolve polishing particles into pure water, and add trace quantity of dispersing agent for ultrasonic stirring. Use a sedimentation particle size distribution meter to measure and select particles. For the surface roughness of the polishing quartz material, measure at three points using ZYGO HP5500.

Classify the factors in the surface rougness for machining as shown in Table A1, and take the correlation data with the surface roughness for machining for each to determine the conditions required in order to obtain good surface roughness. The numeral values show the ranges in which the experiments were performed.

In the experiment for removal of ripple we entirely removed ripple with wave length of 0.5 to 4 mm using tool scanning to observe the change in amplitude of the ripple.

A-4.Experimental Results and Considerations

Clear correlation with the surface roughness for maching was observed in the following four factors.

(1)Particle diameter

Surface roughness when the particle diameter distribution for ZrO_2 particles was changed is shown in Fig.A3.

When the average particle diameter is 0.1 μ m or less, the roughness

of rms 0.1nm or less can be obtained, and when the particle diameter exceeds 1 μ m, polishing streaks increase more. SiO_2 particles of average diameter 0.03 μ m are slightly coaser though the particle diameter is small, but flock, which forms another peak in the particle distribution, is considered to be cause of the coase surface.

(2)Concentration of polishing fluid

Correlation of weight concentration of particles in polishing fluid with the surface roughness for machining is shown in Fig.A4. It has a sufficent removal capacity even at a very low concentration of 0.01%, and a good surface roughness was obtained. Degraded surface roughness on high concentration side is considered to be caused by ease of particles to settle and agglomerate or direct contact in tool--particles-work in the minimal clearance.

(3)Tool oscillation

Giving oscillation motion in parallel with the machined surface, we observed the difference between this case and when there is no oscillation. Fig.A5 shows shape of interference fringes after polihed to a width of 4.2mm for removal. While there are fine whiskers-shaped turbulences in the right impression when there is no oscillation, the left impression shows smooth stripes when oscillation stroke$\pm$ 0.5mm was given. The difference between the two was clearly observed using a surface roughness tester.

(4)Surface roughness of spherical tool

As shown in Fig.A6, the smaller the tool surface roughness is, the better the machined surface roughness becomes. Since the tool rotation and oscillation is given, the machined surface roughness is not likely to be transferred to the tool surface roughness. When the tool roughness is small, it is known that the removal rate is low. Accordingly the micro removal effect for every removal is considered.

As regards other factors shown in Table A1, no correlation with the

machined surface roughness was observed.

(5)Removal chracteristics of ripple

Fig.A7 shows interference fringes showing changes in ripple before and after polishing, and a ripple 0.03 to 0.04μ m in amplitude and 1 mm in width has been smoothed to less than 0.01 μ m in amplitude after polishing about 3 μ m depth. Fig.A8 has been obtained by viewing a changeΔ h in amplitude when completely removed by wave length of ripple with a rateα ($\alpha = \Delta h/H$, H:depth of complete removal). This figure shows that the shorter the wave length of the ripple is, the greater the change in amplitude per a fixed removal depth is, and that there is no changes when the wave length of ripple is 4mm, near the minimal unit removal width of tool.

It was confirmed by this characteristic that ripple can be smoothed at least for less than 0.5mm in wave length. It is also presumed that similar smoothing is also possible for ripple of shorter wave length which can be shown by a roughness tester and the surface roughness will be better.

(6)Evaluation of machined surface

The surface roughness of quartz material polishing under the condition obtained in the above experiment is shown in Fig.A9. The surface of the test piece was observed using a Nomrski microscope and FE-SEM, and no abnormalities such as scratches and surface defect were seen.

A-5.Summary

(1)The E.E.M polishing method using dynamic pressure showed that it has a greater removal rate than the static pressure method.

(2)The said method showed that the shorter the wave length of ripple is, the faster it can be removed .

(3)The said method clarified the roughness factors for machining, and provided surface roughness less than rms 0.1nm or Rmax 1nm.

B. Improvement of Removal Form

B-1.Introduction

When a free curved form is finished by the E.E.M.[1] method, the removal form (hereafter referred to as a unit romoval form) will vary depending on the curvature of the machining surface. When the amount of removal is governed by the stay time of tools on the machining surface and an attempt is made to improve the form accuracy, this will cause an inconvenience as the form of removal is required to be uniform. In the present study, the unit removal form is checked from the aspects of its width and depth separately, and the extent of influence of the variable factors were sought on each aspect experimentally. Next, taking advantage of the variation of removal width depending on the polishing load applied, the authors sought the conditions to obtain a uniform unit removal width by one tool regardless of curvature variations on the machining surface.

B-2.Experiment of Variable Factors of Removal Form

First, a study was made of the extent of influence on the depth and width of the removal form by each factor. Conditions of experiments are shown in TableB1. The experiment indicated the following four items as the major factors greatly affecting the removal form:

(1)Surface Roughness of the Tool:

As shown in Fig.B1, when the surface roughness of the tool becomes greater, the removal depth increases. Where the tool roughness is below $1/\mu$ m Rmax, the removal efficiency is lowered, and at the tool roughness of 0.2μ m Rmax, it will drop to almost zero.

(2)Concentration of Polishing Fluid:

As shown in Fig.B2, in the low concentration area[2] of about 0.1 wt.%, where a good surface roughness can be obtained, a sudden variaion in removal depth is observed against fluid concentration.

(3)Polishing Load:

As shown in Fig.B3, the greater the load, the greater will be the removal width. On the other hand, the removal depth gives little variation when it exceeds a certain level of loading.

(4)Tool Roundness:

When the tool is out of roundness, the form is conspicuously degraded such as variations of removal width and swelling of removal forms. When the roundness is below 3-5 μ m, one can obtain a uniform removal form with good reproductivity.

(5)Other factors:

Though the degree of their influence is small, most of other factors relate to the romoval depth. As for the fluid temperature and rotation speed of the tool, the experiment showed that the higher the fluid temperature and greater the rotation speed of the tool, the lower would be the romoval efficiency. Judging from these results, it is understood that the removal depth is closely related to the clearance between the machining surface and the tool, which depends on fluid variations, and the reaching number of polishing particles derived from said clearance.

B-3.Removal Width on a Plane Surface (A comparison with Hertz's Formula)

The spherical tool in work is deformed of its elasticity due to pressures applied. The theoretical contact diameter 2a at the time when both the tool and the work are at stand still, as is well known, can be obtained by the Hertz's formula.[2]

$$2a = k\sqrt{\frac{3}{4}W\left(\frac{1-\nu_1}{E_1}+\frac{1-\nu_2}{E_2}\right)\left(\frac{r_1 r_2}{r_1+r_2}\right)} \qquad (1)$$

k here is the correction factor introduced to obtain the removal width after polishing.

During actual work, there will be added the rotation of the spheri-

cal tool and the scanning motion along the machining surface. Actually, when the unit removal form is measured with an interferometer under the condition where the spherical tool is rotated in a suspension at the rotation speed of 500 rpm, the amount of removal is greater at the input and output sides of the tool rotation and forms and ellipse of 4.5 mm long diameter and 4.2 mm short diameter, as is illustrated in Fig.B4-a. Further, when the tool is made to scan straight or in circle, the section forms a U-shaped groove, as shown in Fig.B4-b.

The removal width at this time is 4.5 mm. When one substitutes the characteristic value E_1 = 60GP$_a$. E_2 =0.005GP$_a$. ν_1 = 0.2, ν_2 =0.45, $\gamma_1 = \infty$, γ_2 = 25 mm, w = 4.39N for this, 2a = 0.291k (= 4.5 mm) is obtained, and thus the coefficient k = 15.46 is determined.

B-4.Experiment to Obtain Uniform Removal Form on a Spheric Surface:

(1)Method of Experiment:

In this experiment, the authors used a polishing machine of the lower-shaft (the work fixing side) tilting and oscillating type. A work previously finished in a spherical surface was linearly scanned along the surface and removal was conducted for 400 seconds to form a straight groove. In order to make the removal width coincide with the value of a plane and uniform, the coefficient obtained in the previous paragraph is applied in seeking the load for each work curvature through Equation (1). The curvature radii of the works in the experiment and the loading values are illustrated in TableB2. The loading value was set by the varied displacement of the leaf spring (spring constant = 11 gf/ μ m) against the work surface. The removal form was measured with a stylus type, form-tracing, measuring machine which obtained the form of the groove section and read the width.

(2)Results of Experiments and Consideration:

Fig.B5 indicates variations of the removal width on a spherical

work when the work load is made uniform. The theoretical value was sought after the magnification correction with the coefficient obtained on a plane work. With the exception of the U-shaped surface with less than 60 mm curvature radius, it shows values almost similar to the experimental values in the entire curvature region of the work, which illustrates appropriateness of corrections by coefficients under Equation (1). The differences from theoretical values, in case of U-shaped surface with less than 60 mm curvature radius, are considered due to the fact that the machining range covers a wide area of the tool.

Fig.B6 illustrates removal forms with different loadings and at different work curvatures, wherein the removal width is uniform at any curvature used in the experiment. The removal form on the surface is asymmetrical, which is considered to owe to the great polishing load that is set, giving an increased pressure acting on the fluid at the revolution output side of the tool in the machining range.

B-5. Summary

The following are concluded from the above experiment results:

(1)There are many factors relating to the depth of removal. Of particularly great influence are the concentration of polishing fluid, which has relationship with the travel of the polishing particles, and the surface roughness of the tool.

(2)Factors relating to the removal width are the tool roundness, which is related to the tool form, and the polishing load.

(3)It is possible to make the removal width uniform on curved surfaces with different curvatures by varying the polishing load in accordance with the Hertz's formula.

This work has been performed under the Research and Development Program on "Advanced Material Processing and Machining System", conducted under a program set by New Energy and Industrial Technology Develop-

ment Organization.

Reference

1) Mori,Ikawa,Okuda,Sugiyama,Yamauchi:JSPE,vol.49,no.11,p.1540

2) JSME Mechanical Engineers' Handbook, B1,p.31

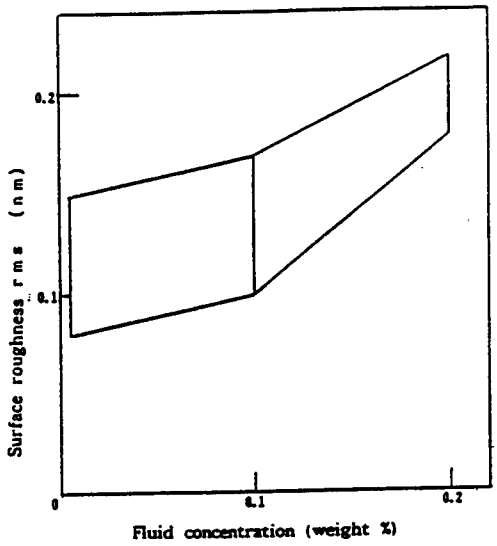

Fig.A4 Correlation with fluid concentration

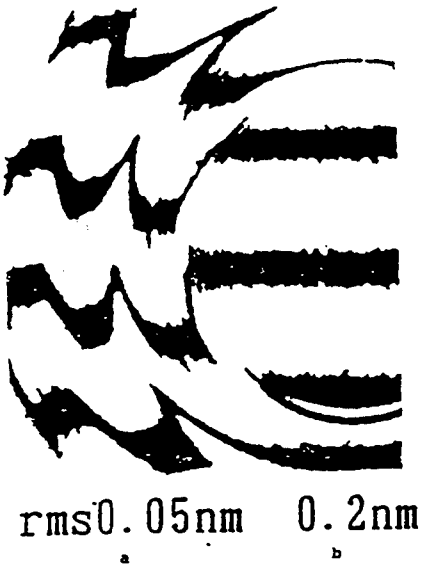

a: with tool oscilation

b: without tool oscilation

Fig.A5 Shape of removal

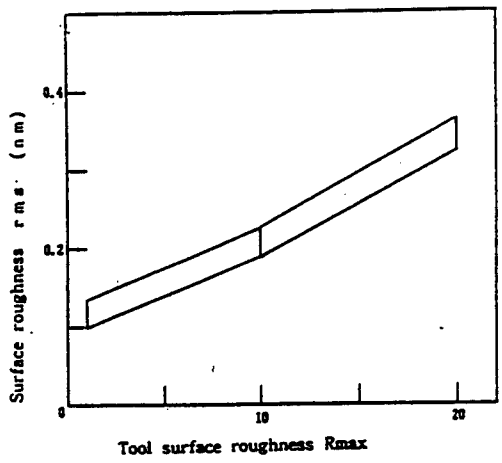

Fig.A6 Correlation with tool surface roughness

Before removal After removal

Fig.A7 Change in swell

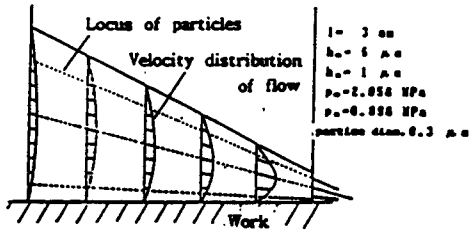

Static pressure system

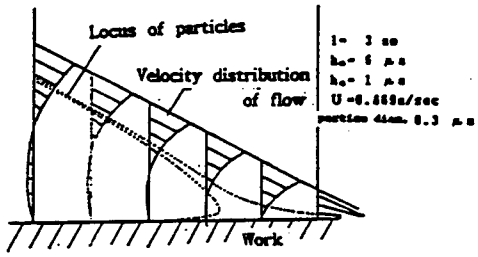

Dynamic pressure system

Fig.A1 Results of Calculation of Comparison Models

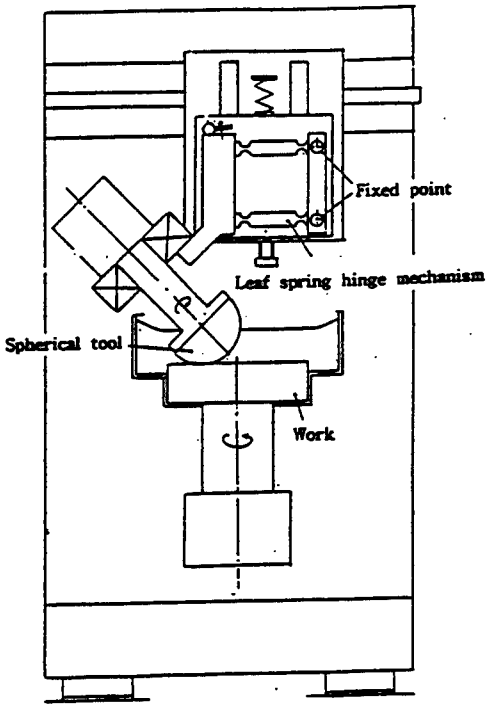

Fig.2 Polishing Device.

TableA1 Objective of Factors of Experiment

Factor		Range
Particle	Average particle diameter	0.03-5μm
	Concentration	0.0005-0.2%
	Type	CeO_2, ZrO_2, SiO_2
Motion	Oscilation velocity	0-2.5mm/sec
	Rotary speed of tool	100-2000rpm
	Load	5.4-21.6N
Tool	Surface roughness	Rmax.1-20 μm
	Type	uretane
	Rubber hardness	60,90,95

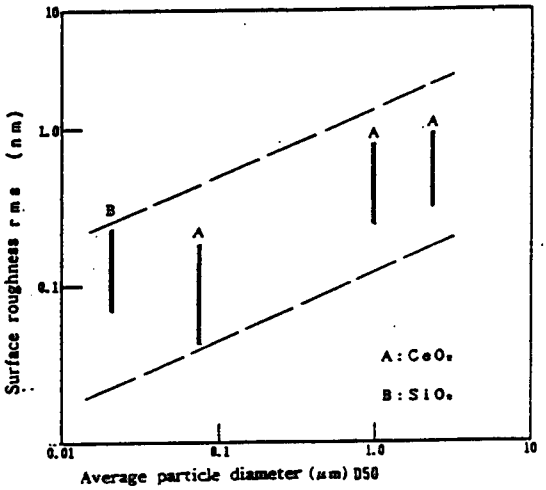

Fig.A3 Correlation with the Particle Diameter

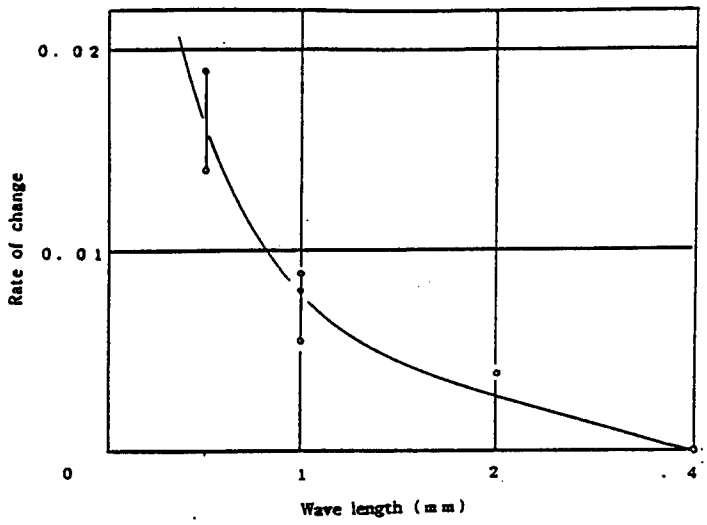

Fig. A8 Change characteristic of swell amplitude by wave length

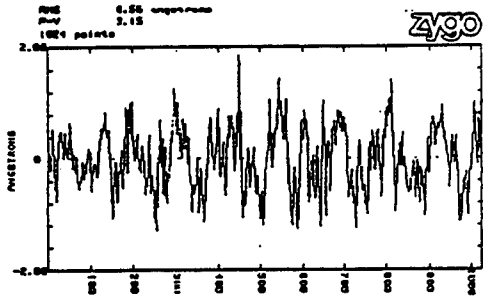

Fig. A9 Polished Surface Roughness Measured by ZYGO HPS500

TableB1 Conditions of Experiment

Tool	Dimension	R25 semisphere
	Material	Hardness 60 Urethane
Speed of Rotation		500 rpm
Polishing Load		550 g
Polishing Particles		ZrO_2 Fine powder
Work		Synthetic quartz ϕ50

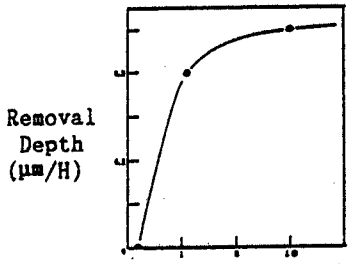

Surface roughness of tool Rmax(μm)

Fig.B1 Influence by Tool Surface

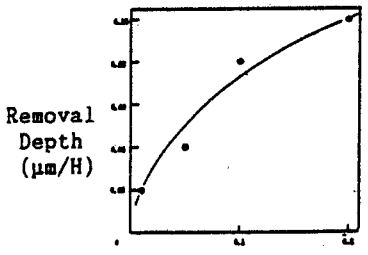

Fluid Concentration (wt.%)

Fig.B2 Influence by Fluid Concentration

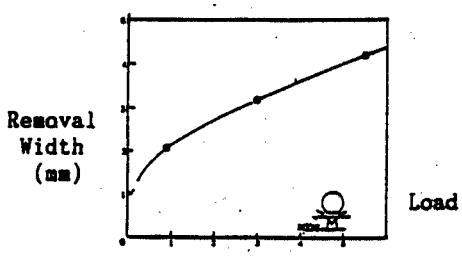

Fig.B3 Influence by Loading

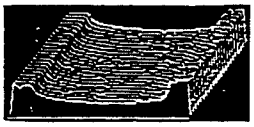

a

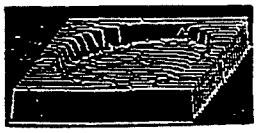

b

Fig.B4 Removal Form

TableB2 Loaded Value

Radius of Curvature mm	Load gm
U 40	206
U 60	320
U 100	412
Plane Surface	550
⊥ 100	688
⊥ 60	778
⊥ 40	894

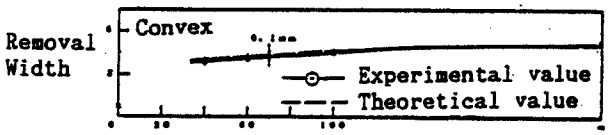

Radius of curvature of the work (⊥ mm)

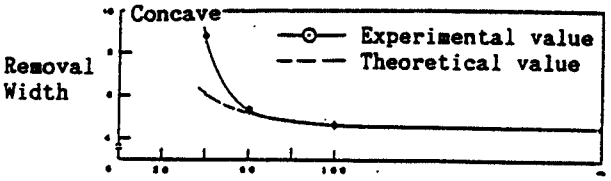

Radius of curvature of the work (U mm)

Fig.B5 Removal Width under Uniform Loading

Output ← Direction of tool rotation

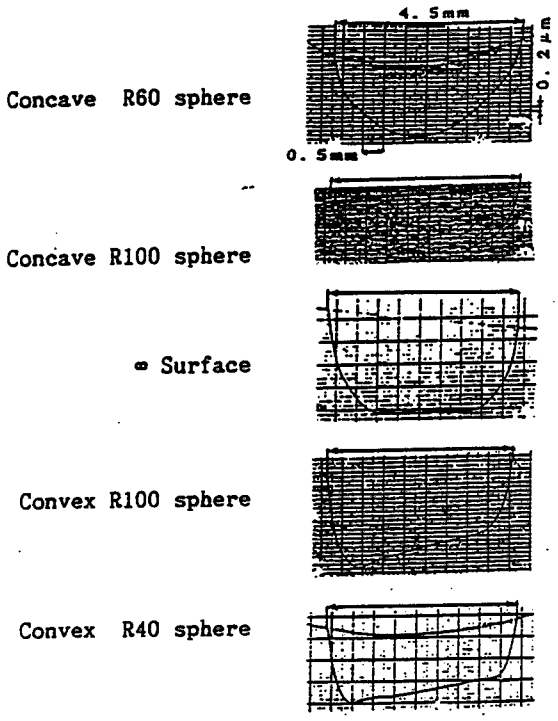

Fig.B6 Removal Form under Varied Loading

The Association of New Glass Industries

Japan Glass Industry Center
3-1-9, Shimbashi Minato-ku, Tokyo
105 JAPAN

社団法人　ニューガラスフォーラム

〒105 東京都港区新橋 3-1-9
日本ガラス工業センタービル

PHONE 03-595-2775　　FACSIMILE 03-595-0255

This symposium is financially supported by Japan Keirin Association.
このシンポジウムは日本自転車振興会からの競輪収益の一部である機械振興資金の補助を受けて実施しました。

- END -

NTIS
ATTN: PROCESS 103
5285 PORT ROYAL RD
SPRINGFIELD, VA 22161

This is a U.S. Government publication. Its contents in no way represent the policies, views, or attitudes of the U.S. Government. Users of this publication may cite FBIS or JPRS provided they do so in a manner clearly identifying them as the secondary source.

Foreign Broadcast Information Service (FBIS) and Joint Publications Research Service (JPRS) publications contain political, military, economic, environmental, and sociological news, commentary, and other information, as well as scientific and technical data and reports. All information has been obtained from foreign radio and television broadcasts, news agency transmissions, newspapers, books, and periodicals. Items generally are processed from the first or best available sources. It should not be inferred that they have been disseminated only in the medium, in the language, or to the area indicated. Items from foreign language sources are translated; those from English-language sources are transcribed. Except for excluding certain diacritics, FBIS renders personal and place-names in accordance with the romanization systems approved for U.S. Government publications by the U.S. Board of Geographic Names.

Headlines, editorial reports, and material enclosed in brackets [ ] are supplied by FBIS/JPRS. Processing indicators such as [Text] or [Excerpts] in the first line of each item indicate how the information was processed from the original. Unfamiliar names rendered phonetically are enclosed in parentheses. Words or names preceded by a question mark and enclosed in parentheses were not clear from the original source but have been supplied as appropriate to the context. Other unattributed parenthetical notes within the body of an item originate with the source. Times within items are as given by the source. Passages in boldface or italics are as published.

SUBSCRIPTION/PROCUREMENT INFORMATION

The FBIS DAILY REPORT contains current news and information and is published Monday through Friday in eight volumes: China, East Europe, Soviet Union, East Asia, Near East & South Asia, Sub-Saharan Africa, Latin America, and West Europe. Supplements to the DAILY REPORTs may also be available periodically and will be distributed to regular DAILY REPORT subscribers. JPRS publications, which include approximately 50 regional, worldwide, and topical reports, generally contain less time-sensitive information and are published periodically.

Current DAILY REPORTs and JPRS publications are listed in *Government Reports Announcements* issued semimonthly by the National Technical Information Service (NTIS), 5285 Port Royal Road, Springfield, Virginia 22161 and the *Monthly Catalog of U.S. Government Publications* issued by the Superintendent of Documents, U.S. Government Printing Office, Washington, D.C. 20402.

The public may subscribe to either hardcover or microfiche versions of the DAILY REPORTs and JPRS publications through NTIS at the above address or by calling (703) 487-4630. Subscription rates will be provided by NTIS upon request. Subscriptions are available outside the United States from NTIS or appointed foreign dealers. New subscribers should expect a 30-day delay in receipt of the first issue.

U.S. Government offices may obtain subscriptions to the DAILY REPORTs or JPRS publications (hardcover or microfiche) at no charge through their sponsoring organizations. For additional information or assistance, call FBIS, (202) 338-6735,or write to P.O. Box 2604, Washington, D.C. 20013. Department of Defense consumers are required to submit requests through appropriate command validation channels to DIA, RTS-2C, Washington, D.C. 20301. (Telephone: (202) 373-3771, Autovon: 243-3771.)

Back issues or single copies of the DAILY REPORTs and JPRS publications are not available. Both the DAILY REPORTs and the JPRS publications are on file for public reference at the Library of Congress and at many Federal Depository Libraries. Reference copies may also be seen at many public and university libraries throughout the United States.